

Modelling antiferromagnetic interfaces with MuMax³

Jonas De Clercq

Promotor:

Prof. Dr. Bartel Van Waeyenberge

Academic year 2016 – 2017

Submitted to the Faculty of Sciences of Ghent University,
in Fulfilment of the Requirements for the Degree of
Doctor of Science: Physics



Modelling antiferromagnetic interfaces with MuMax³

Jonas De Clercq

Public defense: 13th September 2017
DyNaMat, Department of Solid State Sciences

Promotor: Prof. Dr. Bartel Van Waeyenberge

Submitted to the Faculty of Sciences of Ghent University,
in Fulfilment of the Requirements for the Degree of
Doctor of Science: Physics

Ardet ut vivat.



She burns so she may live.

Samenvatting

Computers en *smart devices* in het algemeen zijn niet meer weg te denken in onze huidige samenleving. Technologieën zoals leeskoppen in harde schijven en rotatiesensoren maken vaak gebruik van magnetoresistieve effecten: de weerstand van een sensor hangt af van de relatieve oriëntatie tussen 2 ferromagnetische lagen. Terwijl men de oriëntatie van de ene laag kan regelen door het aanleggen van een extern magnetisch veld, dient de andere laag vastgehouden te worden. Dit gebeurt vaak door deze te koppelen aan een antiferromagneet. De interactie aan de grenslaag tussen een ferromagneet (FM) en een antiferromagneet (AFM) zorgt voor een unidirectionele koppeling in de FM en wordt *exchange bias* genoemd.

Exchange bias treedt op wanneer een FM/AFM dubbellaag gekoeld wordt in een extern veld onder de Néeltemperatuur en leidt tot zowel een verschuiving van de hysteresislus als een verhoogde coërciviteit. Deze effecten worden vaak verklaard door de aanwezigheid van ongecompenseerde AFM spins in de grenslaag. Dit betekent dat slechts 1 subrooster van de AFM koppelt aan de ferromagneet. Naast deze verhoogde coërciviteit en de verschuiving van de hysteresislus, kan men in polykristallijne dubbellaagen ook vaak een training effect waarnemen: de verschuiving en de breedte van de lus nemen af voor een toenemend aantal veldcycli.

Een analyse van de grootte van het exchange bias veld toont aan dat in de meeste systemen slechts een klein deel van de AFM spins vastgevroren zitten in de grenslaag. Wanneer beide subroosters van een antiferromagneet koppelen aan een ferromagneet, dus in het geval van een gecompenseerde AFM grenslaag, zullen beide subroosters de totale energie van het systeem proberen te minimaliseren door hun spins iets af te buigen in de richting van de ferromagneet. Deze tweede orde magnetische interactie, spin flop koppeling genoemd, leidt tot een klein magnetisch moment in de antiferromagneet en tot een verhoogde coërciviteit.

Ondanks dat exchange bias reeds 60 jaar geleden ontdekt is door Meiklejohn en Bean, zijn nog niet alle details volledig begrepen. Eenvoudige modelletjes, die uitgaan van een uniforme magnetisatie in de ferromagneet en de antiferromagneet, zijn immers niet in staat de complexiteit van reële systemen volledig te beschrijven. Om bijvoorbeeld de oorsprong van training effecten in polykristallijne FM/AFM dubbellagen te bestuderen, dient men gebruik te maken van computersimulaties.

In deze thesis onderzoeken we hoe we zowel gecompenseerde als ongecompenseerde antiferromagnetische grenslagen kunnen modelleren in het open source softwareprogramma MuMax³, dat ontwikkeld is binnen onze eigen onderzoeksgroep DyNaMat en voornamelijk gebruikt wordt om statische en dynamische effecten in ferromagneten te bestuderen. Dit laat ons toe een realistische beschrijving te geven van statische effecten die optreden wanneer een ferromagneet gekoppeld wordt aan een antiferromagneet.

In het eerste hoofdstuk van deze thesis geven we een algemene inleiding op de oorsprong van magnetisme en wordt het micromagnetisch framework ingevoerd. Deze theorie middelt kwantummechanische effecten uit over een schaal (orde nanometer) die groot genoeg is om over te gaan van discrete atomaire magnetische momenten naar een continue magnetisatievector. Aan de hand van deze theorie bestudeert men magnetische objecten op een lengteschaal van de orde nanometer tot verschillende micrometer en op een tijdschaal van picosecondes tot honderden nanoseconden. Het slaat dus een brug tussen de atomaire schaal en de macroscopische wereld.

In hoofdstuk 2 bespreken we de ontdekking van exchange bias, de verschillende modellen en enkele technologische toepassingen, bv. de leeskop in een harde schijf of MRAM geheugencellen, waarvan verwacht wordt dat ze binnen enkele jaren een grote impact zullen hebben op data-opslag.

In hoofdstuk 3 leggen we uit hoe we exchange bias, de verhoogde coërciviteit en het athermisch training effect ten gevolge van *ongecompenseerde* AFM spins[1] kunnen modelleren aan de hand van MuMax³. Deze implementatie laat ons toe experimentele data, zoals training in een Co/CoO dubbellaag, te reproduceren.

In hoofdstuk 4 tonen we aan hoe we de spin flop koppeling ten gevolge van *gecompenseerde* antiferromagnetische spins[2] kunnen beschrijven in MuMax³. Ook training effecten in het geval van een gecompenseerde grenslaag met biaxiale anisotropie worden besproken en een fase-diagram opgesteld. Om ons micromagnetisch model te staven aan de fysische realiteit, zullen we ook hier aantonen dat wij experimentele data kunnen reproduceren.

Ten slotte trekken we nog enkele algemene conclusies in hoofdstuk 5 en blikken we vooruit op enkele mogelijke toepassingen van ons micromagnetisch model.

Abstract

*If I have seen further than others,
it is by standing upon the shoulders of giants.*

Isaac Newton

Laptops and smart devices in general have become indispensable in our modern day society. Technologies such as reading heads in hard drives or rotation sensors often make use of magnetoresistive effects: the resistance of a sensor depends on the mutual orientation between 2 ferromagnetic layers. While changing the orientation of one layer by applying an external magnetic field, the other ferromagnetic layer needs to be pinned. This is often done by coupling it to an antiferromagnet. The interface interaction between a ferromagnet (FM) and an antiferromagnet (AFM) gives rise to a unidirectional coupling in the FM layer, which is called *exchange bias*.

Exchange bias occurs when a FM/AFM bilayer is cooled in an external field below the Néel temperature and leads to a shift of the hysteresis loop as well as an enhanced coercivity. These effects are often explained by considering uncompensated AFM spins at the interface. This means only 1 sublattice of the antiferromagnet couples to the FM layer. Besides an increase in coercivity and a shift of the loop, also a training effect in most polycrystalline bilayers is observed, i.e. the bias field and the coercivity decrease for an increasing number of field cycles.

An analysis of the magnitude of the exchange bias field shows that in most systems only a small fraction of the interfacial AFM spins are uncompensated. When both sublattices of an AFM couple to the FM layer, i.e. in case of a compensated AFM interface, the sublattices will try to minimize the total energy of the system by canting towards the ferromagnet. This second order magnetic interaction, called spin flop coupling, produces a small net magnetic moment in the AFM and an increased coercivity.

Although exchange bias was already discovered 60 years ago by Meiklejohn and Bean, not all details are fully understood today. Simple models, which assume that the ferromagnet and the antiferromagnet can be described as uniform layers, are not capable of grasping the complexity of real systems. To study e.g. the origin of training effects in a polycrystalline FM/AFM bilayer, one needs to resort to computer simulations.

In this thesis, we investigate how compensated as well as uncompensated antiferromagnetic interfaces can be modelled in the open source software package MuMax³, which has been developed within our own research group DyNaMat and is predominantly used to study static and dynamic effects in ferromagnets. This implementation allows us to give a realistic description of static effects in ferromagnets due to the presence of an antiferromagnetic interface.

In the first chapter of this thesis, we give a general introduction on the origin of magnetism and the micromagnetic framework is discussed. This theory averages out quantum mechanical effects on a length scale (order nanometer) large enough to replace the discrete atomic moments by a continuous magnetisation vector. One typically investigates magnetic objects on the nanometer to micrometer scale and on a time scale of the order picoseconds to several hundreds of nanoseconds. This bridges the gap between the atomic scale and the macroscopic world.

In chapter 2 we discuss the discovery of exchange bias, the different models and some technological applications, e.g. reading heads in hard drives and MRAM memory cells which will have an important impact on data storage within the next few years.

In chapter 3 we demonstrate how we can model exchange bias, the enhanced coercivity and athermal training effects due to *uncompensated* AFM spins[1] in MuMax³. This implementation allows us to reproduce experimental data, e.g. training in a Co/CoO bilayer.

In chapter 4 we describe how spin flop coupling due to *compensated* anti-ferromagnetic spins[2] can be implemented in MuMax³. Also training in a compensated AFM interface with biaxial anisotropy is discussed and a phase diagram is composed. To demonstrate that our micromagnetic model gives a good approximation of the physical reality, we will also show in this case that we can reproduce experimental data.

Finally, we will draw some general conclusions in chapter 5 and provide an outlook on future applications of our micromagnetic model.

Reflections and Acknowledgments

In the Garden of Paradise, beneath the Tree of Knowledge, bloomed a rose bush. Here, in the first rose, a bird was born. His flight was like the flashing of light, his plumage was beautiful, and his song ravishing. [...] The fable tells that he dwells in Arabia, and that every hundred years, he burns himself to death in his nest; but each time a new Phoenix, the only one in the world, rises up from the red egg.

Hans Christian Andersen, *The Phoenix Bird*

First of all, I would like to thank my parents for giving me this opportunity and my brother for his support. A special thanks to my grandmother who taught me how to make cake and bake chocolate croissants. An important lesson in life and a useful skill!

Secondly, I would like to thank my promotor, Prof. Dr. Bartel Van Waeyenberge, for guiding me through this PhD. Even though (alas) the BEEM experiments never came, exchange bias is (almost) an as interesting topic. Thank you for the pleasant cooperation.

The previous 6 years were rather good, considering the many ups and downs, sometimes floating between hope and despair. It would be wrong and dishonest to claim otherwise. But, after the first paper was finally submitted, there was some faint gloomy light at the end of the tunnel. The fenix always rises again, *n'est-ce pas?* Another sparkle of hope suddenly appeared, just out of the blue, when the article *Modelling exchange bias with MuMax³*[1] was chosen by the Editorial Board of *Journal of Physics D: Applied Physics* as one of the highlights of 2016, officially on the basis of novelty, scientific impact and broadness of appeal. A second paper[2] followed very shortly.

In the end, a nice (at least according to me, let the reader decide for himself) thesis was produced, discussing phenomena which we use every day in our laptop, but are still not fully understood. Probably, due to the many facets, disorder and effects present in the interfacial coupling between a ferromagnet and an antiferromagnet, we will never be able to exactly predict any quantitative results, except in trivial cases. My thesis combines some small pieces of this complex puzzle however, in order to better understand what is going on in exchange biased systems and it offers a tool to other scientists to investigate these phenomena.

Et voilà, behold, my first contributions to the scientific community were made. Maybe not the groundbreaking discoveries as one sometimes would like to see, but nevertheless I am proud of my work. Science often proceeds in small steps. Even 50 years after the discovery of exchange bias and hundreds, thousands of scientific papers later, we are still learning something new about this interface interaction every day. Progress is made... in small... but *not unsignifying* steps.

Furthermore, I would like to thank my dear DyNaMat colleagues: Pieter, Jeroen, Jasper and Jonathan. Some more than others, nonetheless everyone has contributed something substantial in his own way. Mostly, by just hanging around in the neighbourhood of my office and taking time for a (small) talk. It's sad to say goodbye to some...

Finally, I would also like to thank some Lumilab members for their pleasant company during lunch time, which I considered as an oasis of *trouble free me time*. The importance of this small hour is probably underestimated.

Thanks to all those who have made this thesis possible and put their trust in me. Think, act, reflect... and in the end: proceed and try not to look back.

*Believe in what you feel inside,
and give your dreams the wings to fly.*

Josh Groban, *Believe*

Jonas De Clercq
4th of September 2017
my DyNaMat office

Contents

Samenvatting	V
Abstract	IX
Reflections and Acknowledgments	XIII
Contents	XV
1 From Magnetism to Micromagnetism	1
1.1 Introduction	1
1.2 The origin of magnetism	4
1.3 Different forms of magnetism	6
1.4 Micromagnetic approach	14
1.5 Magnetic domains and hysteresis	23
1.6 Stoner Wohlfarth model	26
1.7 Micromagnetic modelling using MuMax ³	30
2 Antiferromagnets and exchange bias	31
2.1 Antiferromagnets	31
2.2 Discovery of exchange bias	33
2.3 Alternative models for exchange bias	37
2.4 Technological applications	43
2.5 Modelling of antiferromagnets	53
3 Modelling uncompensated AFM interfaces in MuMax³	57
3.1 Introduction	57
3.2 Exact solution for uncompensated AFM spins	60
3.3 Approximated solution for uncompensated AFM spins	64
3.4 Implementation of uncompensated AFM interfaces	66
3.5 Testing the micromagnetic model	69
3.6 Example: Training effects in a Co/CoO bilayer	73

3.7	Example: Positive exchange bias fields	84
3.8	Conclusions	91
4	Modelling compensated AFM interfaces in MuMax³	93
4.1	Introduction	93
4.2	Approximated solution for compensated AFM spins	95
4.3	Implementation of compensated AFM interfaces	98
4.4	Testing the micromagnetic model	102
4.5	Example: Spin flop coupling in LSMO/LFO nanosquares	105
4.6	Example: Hoffmann training in a biaxial AFM	111
4.7	Example: Training in an IrMn/CoFe bilayer	121
4.8	Conclusions	126
5	Conclusions and outlook	127
5.1	Conclusions	127
5.2	Future outlook	128
6	Publications	133
	Appendices	137
A	Stoner Wohlfarth for general angles γ	138
B	Exchange bias for an uncompensated AFM	139
C	Implementation of a compensated AFM interface	142
D	Implementation of biaxial anisotropy	152
E	Spin flop coupling for a biaxial AFM	153
F	Exchange bias for a biaxial compensated AFM	155
G	Spin flip in a uniaxial compensated AFM	160
H	Exchange bias induced by unequal coupling strengths in a compensated AFM	162
	Bibliography	165

FROM MAGNETISM TO MICROMAGNETISM

*And Thales, according to what is related of him,
seems to have regarded the soul as something endowed
with the power of motion, if indeed he said
that the loadstone has a soul because it moves iron.*

Aristotle, *De Anima I.2, 405a19*

1.1 Introduction

'Truly remarkable', Thales of Miletus (624 – 546 BC) must have thought when rubbing a piece of amber with animal fur or observing the strange interaction between loadstone and iron. This ancient Greek philosopher who fell into a well while pondering on the nature of the stars¹, is often regarded as the first Western scientist who systematically tried to explain strange effects by considering natural causes rather than seeking refuge in mythology. In a time when most philosophers attributed earthquakes to the rage of Poseidon, he postulated that they were produced by waves in a big ocean upon which the earth was floating. It is not without reason that Bertrand Russell stated in his book *The History of Western Philosophy* that Western philosophy (and by extension also physics) began with Thales.

Since ancient times, humans have always shown a special interest in science and philosophy, whether it is the study of the heavenly bodies, alchemy or the essence of objects themselves. It was only at the end of the 16th century however that a real systematic study of electric and magnetic effects was done. William Gilbert, who was the first one to use the term *electricus*² to

¹At least according to Plato's *Theaetetus*.

²Named after the Greek word for amber.

describe the electric force, published his opus magnum *De Magnete* in 1600 AC. This book was considered as the standard reference work about magnetism for almost 200 years. Gilbert used small magnetic spheres (*terrella*), representing the earth, to study the deflection of a compass in a magnetic field and concluded that the earth behaves as a giant magnet. He also introduced the concepts of magnetic poles and proved that magnets can exert forces on each other, when separated by a distance. In chapter 3 of his book *De Magnete*, he writes: '*Thus do we find two natural poles of excelling importance even in our terrestrial globe [...] In like manner, the loadstone has from nature its two poles, a northern and a southern.*' and in chapter 4, we find: '*For opposite poles attract opposite poles. But, now, if in the same way you present north to north or south to south, one stone repels the other.*' He also remarks that, when breaking a magnet in two pieces, each piece still contains a north and a south pole. Concepts that are still used today.

It took until the beginning of the 19th century however until a fundamental link between electricity and magnetism was established. Ørsted observed that a compass needle was deflected when brought in the neighbourhood of an electric current. In 1865, a groundbreaking paper *General Equations of the Electromagnetic Field* was published by James Clerk Maxwell which, together with the Lorentz force³, provides a complete mathematical description of the theory of electromagnetism. In modern day notation, the microscopic Maxwell equations (representing 8 scalar partial differential equations) are given by

$$\begin{aligned}\nabla \cdot \mathbf{E} &= \frac{\rho}{\epsilon_0} \\ \nabla \cdot \mathbf{B} &= 0 \\ \nabla \times \mathbf{E} &= -\frac{\partial \mathbf{B}}{\partial t} \\ \nabla \times \mathbf{B} &= \mu_0 \mathbf{J} + \mu_0 \epsilon_0 \frac{\partial \mathbf{E}}{\partial t}\end{aligned}$$

These equations show that the total electric charge density ρ and microscopic current density \mathbf{J} are the sources of the electric and magnetic fields, labeled by \mathbf{E} and \mathbf{B} respectively. The constants ϵ_0 and μ_0 represent the

³The Lorentz force $\mathbf{F} = q\mathbf{E} + q\mathbf{v} \times \mathbf{B}$ describes the equations of motion of a charged particle in a magnetic and electric field.

electric permittivity and magnetic permeability in vacuum. These equations also indicate that time varying electromagnetic fields can produce non local fields, even in vacuum and that magnetic monopoles do not exist, or at least not in standard electromagnetic theories. From the source free Maxwell equations, one can easily proof that \mathbf{E} and \mathbf{B} satisfy the standard wave equation, e.g.

$$\epsilon_0\mu_0 \frac{\partial^2 \mathbf{E}}{\partial t^2} - \nabla^2 \mathbf{E} = \mathbf{0} \quad (1.1)$$

as was confirmed by the experiments of Heinrich Hertz in 1887. This explicitly shows that electromagnetic waves travel at the speed of light, i.e. $c = \frac{1}{\sqrt{\epsilon_0\mu_0}} \approx 3 \times 10^8$ m/s.

Using the auxiliary fields $\mathbf{D} = \epsilon_0\mathbf{E} + \mathbf{P}$ and $\mathbf{H} = \frac{1}{\mu_0}\mathbf{B} - \mathbf{M}$, which are called the displacement vector and magnetising field respectively, one can redefine the Maxwell equations in terms of free currents \mathbf{J}_f and free charge densities ρ_f . One can write that

$$\rho = \rho_f - \nabla \cdot \mathbf{P} \quad (1.2)$$

$$\mathbf{J} = \mathbf{J}_f + \nabla \times \mathbf{M} + \frac{\partial \mathbf{P}}{\partial t} \quad (1.3)$$

where \mathbf{P} is the electric polarisation and \mathbf{M} the magnetisation. In linear isotropic dielectric media, experiments have shown that the polarisation is proportional to the electric field and thus

$$\mathbf{D} = \epsilon_0 (1 + \chi_e) \mathbf{E} := \epsilon \mathbf{E} \quad (1.4)$$

The constant χ_e is called the electric susceptibility and is a dimensionless quantity. Analogous for the magnetisation, one can write for homogeneous and isotropic magnetic materials in a weak external magnetic field that

$$\mathbf{B} = \mu_0 (1 + \chi_m) \mathbf{H} := \mu \mathbf{H} \quad (1.5)$$

where χ_m represents the magnetic susceptibility. In case the magnetisation does not respond linearly with the applied field (e.g. in ferromagnets), one defines the magnetic susceptibility as

$$\chi_m = \frac{\partial M}{\partial H} \quad (1.6)$$

It is important to note that χ_e and χ_m are in general tensors and temperature dependent quantities.

1.2 The origin of magnetism

Although the magnetisation vector $\mathbf{M}(\mathbf{r}, t)$ represents a continuous vector field in the Maxwell equations, its origin lies in a quantum mechanical description of discrete magnetic moments $\boldsymbol{\mu}_i$ that can be associated with the intrinsic moment of the nucleus, the intrinsic moment of an electron due to its spin and the magnetic moment associated with the orbital movement of an electron around its nucleus.

1.2.1 Orbital magnetic moment

The orbital magnetic moment of an electron around a fixed nucleus can be understood in a semi-classical description, as is shown in figure 1.1. An electron orbiting a nucleus with an angular velocity $\boldsymbol{\omega}$ at a radius r from the center, induces a current loop⁴ with magnitude $|I| = \frac{e\boldsymbol{\omega}}{2\pi}$. In electromagnetism, the magnetic moment $\boldsymbol{\mu}_l$ of a current loop is given by $\boldsymbol{\mu}_l = I\mathbf{A}$ with $\mathbf{A} = A\mathbf{e}_n$ the surface that is bound by the current loop and \mathbf{e}_n the unit vector perpendicular to the surface, determined by the direction of the current I . For an electron, we find that $\boldsymbol{\mu}_l = \frac{er^2\boldsymbol{\omega}}{2}\mathbf{e}_n = -\frac{e}{2m_e}\mathbf{L}$ with $\mathbf{L} = \mathbf{r} \times \mathbf{p}$ the angular momentum. In quantum mechanics however, the angular momentum vector \mathbf{L} is replaced by an operator whose expectation values are quantised and determined by $L^2|\psi\rangle = l(l+1)\hbar^2|\psi\rangle$ for l ranging from $l = 0$ to $l = n - 1$ with n the principal quantum number. The orbital $l = 0$, $l = 1$ and $l = 2$ are often called the s, p and d orbitals respectively. For the component of the orbital angular momentum along the quantisation axis, we find $L_z|\psi\rangle = m_l\hbar|\psi\rangle$ with m_l ranging from $-l$ to l . This means that the norm of the vector $L = \hbar\sqrt{l(l+1)}$ as well as its projection L_z are quantised. As a consequence, the orbital magnetic moment can be written as $\boldsymbol{\mu}_l = -\frac{\mu_B}{\hbar}\mathbf{L}$ with $\hbar = 1.054 \times 10^{-34}$ J.s the reduced Planck constant and $\mu_B = \frac{e\hbar}{2m_e} = 9.27 \times 10^{-24}$ J/T the Bohr magneton.

1.2.2 Spin magnetic moment

The magnetic moment associated with the spin \mathbf{S} of an electron has no real classical equivalent as it is an intrinsic quantum mechanical property of elementary particles. Similar to the orbital angular momentum, also the spin is quantised with eigenvalues determined by $S^2|\psi\rangle = s(s+1)\hbar^2|\psi\rangle$ and for the component along the quantisation axis we find $S_z|\psi\rangle = m_s\hbar|\psi\rangle$

⁴The conventional current I is opposite to the orbital movement of the electron.

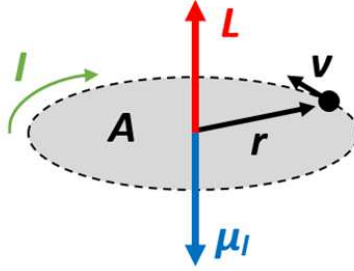


Figure 1.1: Classical concept of the orbital magnetic moment μ_l of an electron, orbiting a nucleus with velocity v .

with $s = \frac{1}{2}$ for an electron and thus $m_s = \pm \frac{1}{2}$. Using the Dirac equation, one can show that the intrinsic spin magnetic moment of an electron is given by $\mu_s = -g_e \frac{\mu_B}{\hbar} \mathbf{S}$ where $g_e = 2$ is called the g-factor. For an electron with angular momentum \mathbf{L} and spin \mathbf{S} , the total magnetic moment is thus given by

$$\boldsymbol{\mu} = -\frac{\mu_B}{\hbar} (\mathbf{L} + 2\mathbf{S}) \quad (1.7)$$

1.2.3 Total magnetic moment of an atom

Until now, the magnetic moment of only 1 electron was discussed. In an atom however, many electrons are present and thus one needs to put together all those orbital and spin angular momenta to determine the total magnetic moment of an atom⁵. In case the electrons are strongly bound (localised) to the nucleus, this can be done by using the Russell Saunders $\mathbf{L} - \mathbf{S}$ coupling or the $\mathbf{J} - \mathbf{J}$ coupling scheme, depending on the size of the spin orbit coupling⁶. For lighter atoms (typically $Z < 40$), the spin orbit

⁵The nuclear magnetic moment can often be neglected due to the heavy masses of protons and neutrons compared to that of electrons as $|\mu_i| \propto \frac{1}{m_i}$ and $\frac{m_p}{m_e} \approx 1800$. Taking into account the nuclear magnetic moment leads to the hyperfine interaction.

⁶In a classical treatment, one can say that from the reference system of the electron (neglecting that this is not an inertial system), the nucleus with a charge Ze orbits around the electron and thus produces a magnetic field which is proportional to the orbital angular momentum \mathbf{L} of the electron. This magnetic field interacts with the spin magnetic moment and thus couples the angular momentum to the intrinsic spin \mathbf{S} of the electron. In the case of only 1 electron, the spin orbit Hamiltonian as found from a full quantum mechanical treatment is given by $\mathcal{H}_{so} = \frac{1}{2m_e^2 c^2} \left(\frac{1}{r} \frac{\partial V}{\partial r} \right) \mathbf{L} \cdot \mathbf{S}$ with V the Coulomb potential induced by the nucleus on the place of the electron and thus proportional to the total charge Ze of the nucleus.

interaction is small and thus one can use the Russell Saunders coupling. In this scheme, one first couples all individual orbital angular momenta \mathbf{L}_i together into a total $\mathbf{L} = \sum_i \mathbf{L}_i$ and afterwards one separately couples all individual spin angular momenta \mathbf{S}_i together into a total momentum $\mathbf{S} = \sum_i \mathbf{S}_i$. The total angular momentum \mathbf{J} of an atom can in this case be written as $\mathbf{J} = \mathbf{L} + \mathbf{S}$. The allowed values for J are given by $J = |L - S|$ to $J = L + S$ as the composition of the vectors \mathbf{L} and \mathbf{S} have to satisfy the triangle inequality. The total magnetic moment of an atom with a certain angular momentum \mathbf{J} , is determined by $\boldsymbol{\mu}_J = -\frac{\mu_B}{\hbar} g_J \mathbf{J}$ with $g_J = \frac{3}{2} + \frac{S(S+1) - L(L+1)}{2J(J+1)}$ the Landé splitting factor and so the magnitude of the magnetic moment is given by

$$|\mu_J| = \mu_B g_J \sqrt{J(J+1)} \quad (1.8)$$

As for closed shells $J = 0$, only the electrons in the outermost non filled shell contribute to the total magnetic moment of an atom.

1.3 Different forms of magnetism

To study the different types of magnetic effects, it is necessary to take a look at the response of an electron in a magnetic field. A quantum mechanical treatment⁷ of this problem shows that to determine the kinetic energy of an electron, the momentum \mathbf{p} has to be replaced by $\mathbf{p} \rightarrow \mathbf{p} + e\mathbf{A}$. The vector field \mathbf{A} is called the magnetic vector potential and is defined by the relation $\mathbf{B} = \nabla \times \mathbf{A}$, which satisfies the Maxwell equation $\nabla \cdot \mathbf{B} = 0$. The kinetic part of the Hamiltonian of an electron is then given by

$$\mathcal{H} = \frac{(\mathbf{p} + e\mathbf{A})^2}{2m_e} \quad (1.9)$$

For an uniform external field \mathbf{B} , we can write⁸ that $\mathbf{A} = -\frac{1}{2}\mathbf{r} \times \mathbf{B}$ using the gauge condition $\nabla \cdot \mathbf{A} = 0$. Expanding the Hamiltonian, we find

$$\mathcal{H} = \frac{(\mathbf{p} - \frac{e}{2}\mathbf{r} \times \mathbf{B})^2}{2m_e} = \frac{\mathbf{p}^2}{2m_e} - \frac{e\mathbf{p} \cdot (\mathbf{r} \times \mathbf{B})}{2m_e} + \frac{e^2}{8m_e} (\mathbf{r} \times \mathbf{B})^2 \quad (1.10)$$

⁷It appears that for a charged particle q in an electromagnetic field, the canonical conjugate of the position is not the linear momentum \mathbf{p} anymore, but given by $\mathbf{p} - q\mathbf{A}$.

⁸Using vector calculus, one can check for this expression that $\nabla \times \mathbf{A} = \mathbf{B}$ and also $\nabla \cdot \mathbf{A} = 0$. This definition thus satisfies the requirements.

where we have used that \mathbf{p} commutes with \mathbf{A} for a homogeneous field \mathbf{B} , as $[p_i, r_j] = 0$ for $i \neq j$. Assuming $\mathbf{B} = B\mathbf{e}_z$ and rewriting the term $\mathbf{p} \cdot (\mathbf{r} \times \mathbf{B}) = -\mathbf{B} \cdot (\mathbf{r} \times \mathbf{p}) := -\mathbf{B} \cdot \mathbf{L}$, we obtain

$$\begin{aligned} \mathcal{H} &= \frac{\mathbf{p}^2}{2m_e} + \frac{\mu_B}{\hbar} \mathbf{B} \cdot (\mathbf{L} + 2\mathbf{S}) + \frac{e^2 B^2}{8m_e} (x^2 + y^2) \\ &= \mathcal{H}_0 + \mathcal{H}_{\text{para}} + \mathcal{H}_{\text{dia}} \end{aligned} \quad (1.11)$$

where we have added the interaction of a spin \mathbf{S} with the magnetic field \mathbf{B} . The first term is the normal kinetic energy of the electron, the second term is the paramagnetic contribution and the last term leads to a diamagnetic effect.

1.3.1 Diamagnetism

Diamagnetism is a form of magnetism that is present in all materials, even in atoms with filled shells ($J = 0$), as can be seen from equation 1.11. Considering such an atom⁹ for simplicity, the Hamiltonian corresponding to the diamagnetic contribution for N_e localised electrons, can be seen as a small perturbation. Defining $|\Psi_0\rangle$ as the ground state of the unperturbed Hamiltonian and retaining only the first order term, we find as energy correction

$$\begin{aligned} E_{\text{dia}} &= \langle \Psi_0 | \sum_i \mathcal{H}_{\text{dia},i} | \Psi_0 \rangle = \frac{e^2 B^2}{8m_e} \sum_i \langle \Psi_0 | x_i^2 + y_i^2 | \Psi_0 \rangle \\ &= \frac{e^2 B^2 N_e}{12m_e} \langle r^2 \rangle \end{aligned} \quad (1.12)$$

assuming spherical symmetry and defining the average quadratic radius as $\langle r^2 \rangle = \frac{1}{N_e} \sum_i \langle \Psi_0 | r_i^2 | \Psi_0 \rangle$.

Labeling N as the number of atoms are present in the solid, we can calculate the magnetisation M by using that $M = -\frac{1}{\mu_0 V} \left(\frac{\partial E}{\partial H} \right)$ and for the magnetic susceptibility that $\chi_m = \frac{\partial M}{\partial H}$. So we find

$$M = -\frac{e^2 B N_e n}{6m_e} \langle r^2 \rangle \quad (1.13)$$

$$\chi_m = -\frac{\mu_0 e^2 N_e n}{6m_e} \langle r^2 \rangle \quad (1.14)$$

⁹So we don't have to take into account the paramagnetic contribution to the Hamiltonian.

with $n = \frac{N}{V}$ the number of atoms per unit volume. This shows that the diamagnetic effect leads to a negative susceptibility and thus the atoms are being repelled by an external magnetic field. For water, one finds that $\chi_m \approx -9 \times 10^{-6}$ at a temperature of 20 °C. As diamagnetism is a very weak effect in atoms, it is often overcome by the paramagnetic contribution.

1.3.2 Paramagnetism

Paramagnetism occurs in atoms which have a net magnetic moment μ_J . When an external field is applied, the magnetic moments will try to align themselves parallel to the magnetic field and produce a macroscopic magnetisation. When no field is present however, thermal fluctuations randomize their moments and so no spontaneous magnetisation is present. In the case of a free atom with localised electrons, the energy of a magnetic moment μ_J in an external field $\mathbf{B} = B\mathbf{e}_z$ is given by $E = \frac{\mu_B}{\hbar} g_J \mathbf{J} \cdot \mathbf{B}$. Using $M = -\frac{1}{\mu_0 V} \left(\frac{\partial E}{\partial H} \right)$, one can show[3] that the magnetisation is given by

$$M(x) = ng_J\mu_B JB_J(x) \quad (1.15)$$

with $n = \frac{N}{V}$ the number of atoms per unit volume and where $B_J(x)$ is called the Brillouin function

$$B_J(x) = \left(1 + \frac{1}{2J}\right) \coth \left[x \left(1 + \frac{1}{2J}\right) \right] - \frac{1}{2J} \coth \left[\frac{x}{2J} \right] \quad (1.16)$$

with $x = \frac{g_J\mu_B JB}{k_B T}$. This shows that in the absence of an external magnetic field, the magnetisation M for paramagnetic atoms vanishes as $B_J(0) = 0$.

In case $x \ll 1$, one can expand the Brillouin function and so we find that

$$M = \frac{ng_J^2 J(J+1)\mu_B^2 B}{3k_B T} \quad (1.17)$$

using that $\coth(y) \approx \frac{1}{y} + \frac{y}{3}$. For the susceptibility χ_m , we obtain

$$\chi_m = \frac{n\mu_0 g_J^2 J(J+1)\mu_B^2}{3k_B T} := \frac{C_P}{T} \quad (1.18)$$

which amounts to the famous Curie law for paramagnets and where C_P is called the Curie constant. The magnetic susceptibility is positive, in contrast to the diamagnetic effect.

In the case of low temperatures and high magnetic fields ($x \rightarrow \infty$), the Brillouin function approaches 1 and so we find for the magnetisation

$$M = ng_J\mu_B J \quad (1.19)$$

which corresponds to the maximal attainable magnetisation.

Keeping the temperature constant, one can conclude that for low magnetic fields the magnetisation of paramagnets varies linearly with B and saturates in high magnetic fields, i.e. when all magnetic moments are aligned. This behaviour can be seen in figure 1.2.

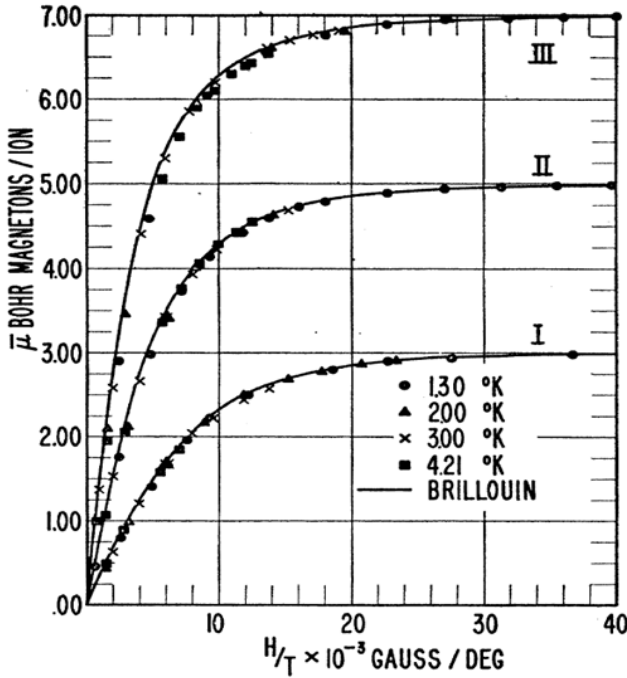


Figure 1.2: Average magnetic moment per Cr^{3+} , Fe^{3+} and Gd^{3+} ion in the salts CrKO_8S_2 (I, $S = 3/2$), $\text{NH}_4\text{Fe}(\text{SO}_4)_2 \cdot 12\text{H}_2\text{O}$ (II, $S = 5/2$), and $\text{Gd}_2(\text{SO}_4)_3 \cdot 8\text{H}_2\text{O}$ (III, $S = 7/2$) respectively as a function of the parameter $\frac{H}{T}$ which is proportional to x . For each of these materials, the orbital magnetic moment is quenched, i.e. $\langle L \rangle = 0$, which leads to $J = S$. Reproduced from [4].

1.3.3 Ferromagnetism

We have discussed that magnetism arises due to the presence of magnetic moments which can be associated with the intrinsic spin and orbital angular momenta of electrons in an atom. In the previous section, we have seen that paramagnetic atoms can only have a macroscopic magnetisation when an external field is applied.

Experiments have shown however that some materials, called ferromagnets, can have a spontaneous magnetisation in the absence of an external field and that their magnetisation vanishes above a critical temperature, called the Curie temperature T_C which is specific for each material. Above T_C these materials behave as paramagnets. To account for these effects, Pierre Weiss¹⁰ assumed that in ferromagnets an internal field is present, which is proportional to its own magnetisation. This *molecular field*, as Weiss called it, originates from the quantum mechanical nature¹¹ of the Coulomb interaction and tries to align the magnetic moments in absence of an external field. We can thus write for the total field that $H \rightarrow H_t = H + \lambda M$. Using for paramagnets that $M = \left(\frac{C_P}{T}\right)H$ as given in equation 1.17, we find for ferromagnets above the Curie temperature that

$$M = \frac{C_P(H + \lambda M)}{T} \quad (1.20)$$

Rearranging terms, we obtain $M = \left(\frac{C_P}{T - T_C}\right)H$ with $T_C = \lambda C_P$. The magnetic susceptibility is then given by

$$\chi_m = \frac{C_P}{T - T_C} \quad (1.21)$$

¹⁰J. Phys Radium 4,661 (1907)

¹¹ The total wave function of a two electron system (helium atom), orbiting a nucleus, can be described as the product of a spatial wave function and a wave function, associated with the spins of the 2 electrons. As the total wave function has to be antisymmetric while exchanging the 2 electrons due to the Pauli exclusion principle, the spatial part has to be antisymmetric and the spin part symmetric or vice versa. The energy, related to the Coulomb repulsion between the 2 electrons, is lower when the spatial wave function is antisymmetric, as then the overlap between the 2 spatial wave functions is minimal. With an antisymmetric spatial wave function, one has to associate a symmetric spin wave function which induces a parallel spin orientation of the two electrons. The energy difference between the triplet states ($S = 1$) and singlet state ($S = 0$) is called the exchange energy and leads to the Heisenberg Hamiltonian, as given in equation 1.29.

as can be seen in figure 1.3. This law gives a good description above the Curie temperature and is called the Curie - Weiss law. The divergence of the susceptibility at $T = T_C$ is a signature of a phase transition, i.e. the paramagnet becomes ferromagnetic under the transition temperature. Using the definition of the Curie constant C_P as given in equation 1.18, we can write the constant λ as a function of T_C

$$\lambda = \frac{T_C}{C_P} = \frac{3k_B T_C}{\mu_0 n g_J^2 J(J+1) \mu_B^2} \quad (1.22)$$

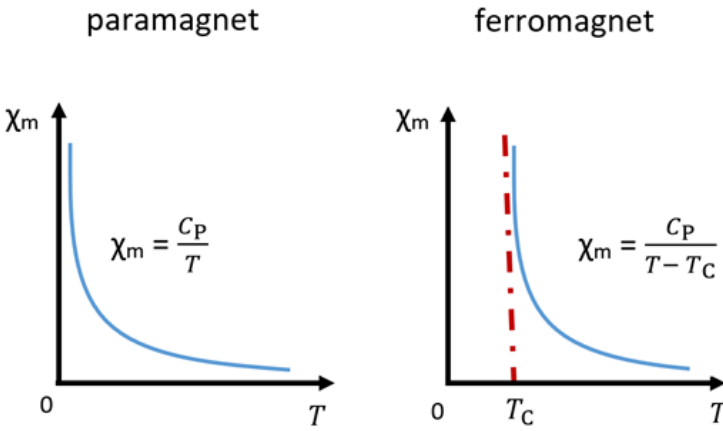


Figure 1.3: The susceptibility of ferromagnets above the Curie temperature T_C is very similar to that of paramagnets, but is shifted. The divergence at $T = T_C$ signals a phase transition from a disordered to an ordered ferromagnetic state. For a ferromagnet, the behaviour of the susceptibility for $T < T_C$ is material dependent and thus not shown.

To determine the magnetisation of a ferromagnet as a function of temperature, one can make following substitution in the argument of the Brillouin function

$$x \rightarrow \frac{\mu_0 g_J \mu_B J (H + \lambda M)}{k_B T} \quad (1.23)$$

The spontaneous magnetisation, i.e. at a vanishing external field, can be found by setting $H = 0$ and thus solving

$$M = n g_J \mu_B J B_J(x_0) \quad (1.24)$$

with

$$x_0 = \frac{3M}{ng_J(J+1)\mu_B} \left(\frac{T_C}{T} \right) \quad (1.25)$$

which is an implicit equation and can only be solved numerically.

For ferromagnets, a parallel orientation between the spins is preferred as the Weiss constant λ was assumed to be positive. In some materials however, an antiparallel orientation between 2 neighbouring spins is energetically more favourable, leading to ferri - or antiferromagnetic behaviour.

1.3.4 Metallic paramagnets and ferromagnets

Until now we have always assumed that the electrons were strongly bound and thus localised to their nucleus. Experiments have shown however that the susceptibility attributed to conduction electrons is very small and nearly independent of temperature. For metals, the model of a free electron gas is more appropriate. When such a metal, with as many spin up as spin down electrons (see figure 1.4), is brought inside a magnetic field, the original symmetric band structure will split into 2 parts. The band of electrons with a magnetic moment antiparallel to the field will be shifted upwards with an energy $\mu_B B$, whereas the band of electrons with a magnetic moment parallel to the field, will be shifted downwards with an energy $-\mu_B B$. As the 2 spin split energy bands are still filled up to the Fermi level, this shifting leads to a net transfer of electrons with an antiparallel moment to electrons in the lowest energy band, i.e. with a magnetic moment parallel to the field. One can show[5] that the paramagnetic susceptibility χ_P , called the Pauli susceptibility, associated with this behaviour is given by

$$\chi_P = \mu_0 \mu_B^2 D(E_F) \quad (1.26)$$

where $D(E_F)$ corresponds to the density of states at the Fermi level. This is typically a small effect and arises only in the presence of an external magnetic field.

In the case of metallic ferromagnets, an internal magnetic field is present due to the exchange interaction, analogous to what was discussed in the Weiss theory. This leads to a *spontaneous* splitting of the energy bands as can be seen in figure 1.5 for hcp cobalt and gives rise to a measurable net magnetic moment, even in the absence of an external field.

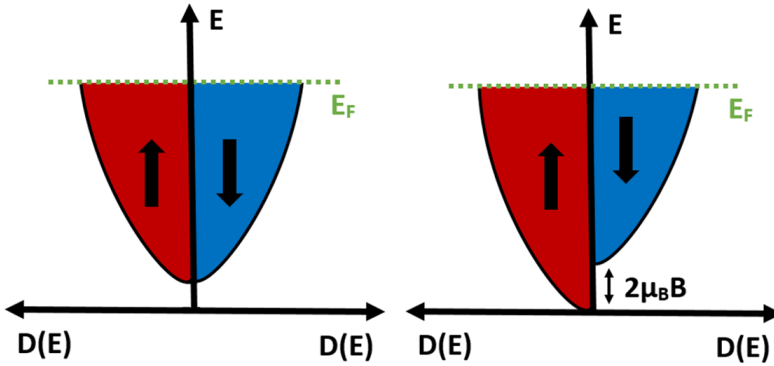


Figure 1.4: Pauli paramagnetism in a free electron gas. Left: when no magnetic field is applied, there are as many spin up as spin down electrons. Right: due to the splitting of the energy bands in a magnetic field, a net magnetic moment is produced. In a ferromagnet, this splitting happens spontaneously due to the exchange interaction.

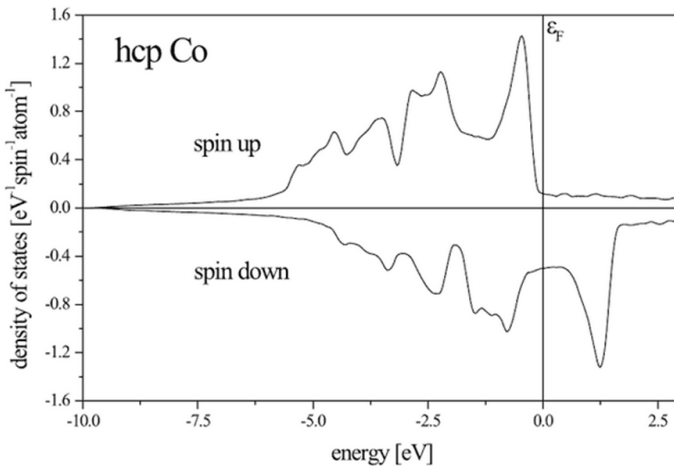


Figure 1.5: Total density of states in hcp cobalt. The exchange split polarised 3d energy bands lead to a net magnetic moment. For non magnetic metals, the 2 energy bands are symmetric with respect to the Fermi level. Reproduced from [5].

The condition for the spontaneous splitting of the energy bands, is given by the Stoner criterion which demands that $I_S D(E_F) > 1$ where I_S is called the Stoner parameter, which is related to the Weiss constant λ and thus the strength of the exchange interaction. Typically, 3d ferromagnets have a peak in their density of states near the Fermi level and the constant I_S is on the order of 1 eV. The Stoner criterion is satisfied for Fe, Co (although barely) and Ni, which should not come as a surprise.

1.4 Micromagnetic approach

When studying magnetic objects on the micrometer scale, it is often not desirable to take into account the full quantum mechanical description which is very complicated and requires a lot of computing time. For this reason an effective theory, called micromagnetism, was developed by Landau and Lifshitz[6] in the early part of the 20th century while studying a domain wall between 2 antiparallel magnetic domains. In micromagnetism, one averages out quantum mechanical effects and discrete magnetic moments over a length scale larger than the atomic scale, but small enough to resolve magnetic structures such as domain walls or vortex cores. Using this theory, one typically studies ferromagnets on the scale of a few nanometers up to the order of several micrometers and on a time scale of the order picoseconds to several hundreds of nanoseconds. Thus, bridging the gap between atoms and fridge magnets.

In the micromagnetic framework, the discrete atomic magnetic moments in a ferromagnet are replaced by a continuous vector field $\mathbf{M}(\mathbf{r}, t)$ as one assumes strong coupling between the moments, i.e. the angles between the magnetic moments are small. The magnetisation $\mathbf{M}(\mathbf{r}, t)$ can be written as $\mathbf{M}(\mathbf{r}, t) = M_s \mathbf{m}(\mathbf{r}, t)$ where M_s is called the saturation magnetisation, defined as the average magnetic moment per unit volume, i.e. $M_s = \frac{\sum_i \mu_i}{\Delta V}$ with the averaging volume ΔV larger than the atomic scale. The vector $\mathbf{m}(\mathbf{r}, t)$ is a dimensionless unit vector, pointing in the direction of the magnetisation. For cobalt, one finds that $M_s \approx 1400$ kA/m.

As energy minimalisation is the driving force in nature, the evolution and magnetic configuration of a system will be determined by the different energy contributions, amounting into a total free energy functional E given by

$$E[\mathbf{m}] = \int_V \varepsilon[\mathbf{m}] d^3 \mathbf{r} \quad (1.27)$$

Using this, one can define a quantity \mathbf{H}_{eff} , called the effective field¹², determined by the functional derivative of the energy density ε

$$\mathbf{H}_{\text{eff}}(\mathbf{r}, t) = -\frac{1}{\mu_0 M_s} \frac{\delta \varepsilon}{\delta \mathbf{m}} \quad (1.28)$$

We will now briefly discuss the most important energy terms.

1.4.1 Exchange energy

Direct exchange coupling is a short ranged force (order nanometers) and finds its origin in the electrostatic Coulomb repulsion, overlap of the wave functions and the Pauli exclusion principle. The exchange energy between 2 normalised spins \mathbf{S}_i and \mathbf{S}_j is given by the Heisenberg Hamiltonian¹³

$$E_{ij} = -2J_{ij} \mathbf{S}_i \cdot \mathbf{S}_j \quad (1.29)$$

where J_{ij} is called the exchange integral. A positive exchange integral leads to ferromagnetism and $J_{ij} < 0$ produces an antiferromagnetic interaction as then an antiparallel spin orientation is preferred. If for each pair $J_{ij} = J$ and $|\mathbf{S}_i| = |\mathbf{S}_j| = S$, we can write

$$E_{ij} = -2JS^2 \cos \phi_{ij} \approx JS^2 \phi_{ij}^2 \quad (1.30)$$

assuming strong coupling between 2 neighbouring spins and neglecting the constant energy term. Writing the angle ϕ_{ij} in terms of the normalised magnetisation vectors \mathbf{m}_i and \mathbf{m}_j , summing over nearest neighbours and taking the continuum limit, one can show[7] that the exchange energy can be written as

$$E_{\text{ex}} = \int_V A_{\text{ex}} \left[(\nabla m_x)^2 + (\nabla m_y)^2 + (\nabla m_z)^2 \right] d^3 \mathbf{r} \quad (1.31)$$

$$= \int_V A_{\text{ex}} (\nabla \mathbf{m})^2 d^3 \mathbf{r} \quad (1.32)$$

¹²The importance of the effective field will be discussed in section 1.4.5.

¹³The factor 2 follows from the energy difference between a triplet and singlet state. A quantum mechanical analysis of the two electron system shows that $E_{\text{trip}} - E_{\text{sing}} = -2J$ with J the exchange integral.

The micromagnetic parameter A_{ex} is called the exchange stiffness and is given by $A_{\text{ex}} = \frac{nJS^2}{a}$. In cubic lattices, n is the number of atoms per unit cell and a the lattice constant. For a bcc lattice, one has for example that $n = 8 \times \frac{1}{8} + 1 = 2$. For cobalt, one typically finds from experiments that $A_{\text{ex}} \approx 3 \times 10^{-11}$ J/m. Calculating the functional derivative of the exchange energy, we can associate an effective field \mathbf{H}_{ex} with it, given by

$$\mathbf{H}_{\text{ex}} = 2 \frac{A_{\text{ex}}}{\mu_0 M_s} \nabla^2 \mathbf{m} \quad (1.33)$$

It is important to note that in the case of an antiferromagnet, this micromagnetic approximation is not valid anymore as the angle between 2 neighbouring spins approaches 180° . The implications of this antiparallel ordering in our micromagnetic model will be discussed in section 3.4.

1.4.2 Magnetocrystalline energy

The magnetocrystalline energy originates from the spin orbit coupling and the crystal field interaction, which is related to the symmetry of the crystal. In this case, the energy of the system depends on the orientation of the magnetisation vector with respect to certain crystallographic axes, which breaks the rotational symmetry in the system. Axes of high energy are called hard axes as it takes a large magnetic field to align the magnetisation vector along that direction. It is important to note that these axes are not unidirectional, i.e. 2 magnetic states 180° apart have the same energy. Depending on the symmetry of the crystal, one can expand the energy as a series of direction cosines.

In case of a uniaxial magnetocrystalline anisotropy, the energy is given by

$$E_{\text{uni}} = - \int_V [K_1(\mathbf{u} \cdot \mathbf{m})^2 + K_2(\mathbf{u} \cdot \mathbf{m})^4 + \dots] d^3 \mathbf{r} \quad (1.34)$$

dropping higher order terms. The unit vector \mathbf{u} is called the anisotropy axis and K_1 and K_2 the first and second order anisotropy constants, respectively. The corresponding effective field is given by

$$\mathbf{H}_{\text{anis}} = \frac{2K_1}{\mu_0 M_s} (\mathbf{u} \cdot \mathbf{m}) \mathbf{u} + \frac{4K_2}{\mu_0 M_s} (\mathbf{u} \cdot \mathbf{m})^3 \mathbf{u} \quad (1.35)$$

Bulk hcp cobalt typically has a uniaxial anisotropy along its c-axis with $K_1 = 0.45$ MJ/m³ and $K_2 = 0.15$ MJ/m³.

Considering only the first order uniaxial anisotropy and exchange energy, one can define a typical length scale, called the exchange length $l_{\text{ex}} = \sqrt{\frac{A_{\text{ex}}}{K_1}}$, on which the magnetisation needs to rotate between 2 antiparallel magnetic domains. For cobalt, we find that $l_{\text{ex}} \approx 8$ nm. In micromagnetic simulations, one typically chooses the cell size smaller than the exchange length.

In case of a biaxial anisotropy, we can define the magnetocrystalline energy as

$$E_{\text{biax}} = \int_V K_c (\mathbf{u}_1 \cdot \mathbf{m})^2 (\mathbf{u}_2 \cdot \mathbf{m})^2 d^3 \mathbf{r} \quad (1.36)$$

where \mathbf{u}_1 and \mathbf{u}_2 represent the 2 normalised anisotropy axes, perpendicular to each other. The energy density ϵ_{biax} as a function of the angle that the magnetisation makes with respect to the easy axes, is shown in figure 1.6. It is clear that biaxial anisotropy is not the same as a combination of 2 perpendicular uniaxial anisotropy axes, as the latter only gives rise to a constant energy shift.

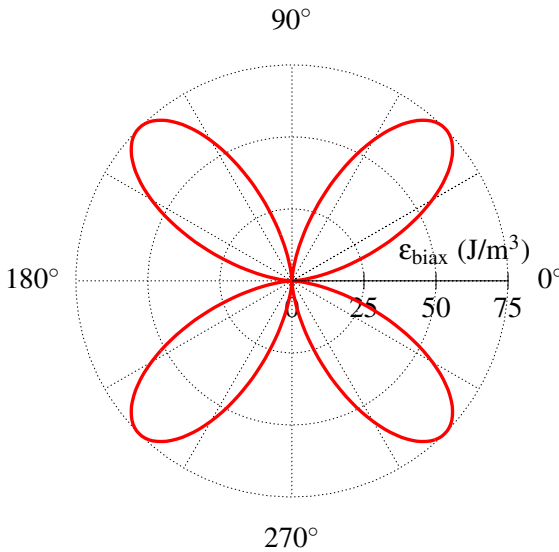


Figure 1.6: Polar plot of the energy density ϵ_{biax} in the case of biaxial anisotropy with $K_c = 3 \times 10^2 \text{ J/m}^3$ and easy axes along 0° and 90° . Remark that at 45° the maximal energy density $\epsilon_{\text{biax}} = \frac{K_c}{4} = 75 \text{ J/m}^3$ is reached.

1.4.3 Magnetostatic energy

This energy contribution is related to the interaction of the magnetisation \mathbf{M} with its own induced magnetic field \mathbf{H}_d and can be viewed as a self energy. It arises from the fact that every magnetic moment acts as a tiny dipole. The sum of all these dipole fields creates a macroscopic field \mathbf{H}_d that opposes the magnetisation inside the magnet. As the Maxwell equations demand that $\nabla \cdot \mathbf{B} = 0$, we can write that

$$\nabla \cdot \mathbf{H}_d = -\nabla \cdot \mathbf{M} \quad (1.37)$$

$$\nabla \times \mathbf{H}_d = \mathbf{0} \quad (1.38)$$

discarding any free currents, polarisation or electric fields. The last equation implies that \mathbf{H}_d can be derived from a scalar magnetic potential Φ according to $\mathbf{H}_d = -\nabla\Phi$. Using the first equation, we can see that the solution is given by the Poisson equation $\nabla^2\Phi = \nabla \cdot \mathbf{M} := -\rho_m$ inside the magnet and $\nabla^2\Phi = 0$ outside the magnet. Using the boundary condition that the potential has to vanish at infinity to obtain a finite energy, one can calculate[8] that the solution to this problem is given by

$$\Phi(\mathbf{r}, t) = \frac{1}{4\pi} \left[\int_V \frac{\rho_m(\mathbf{r}', t)}{|\mathbf{r} - \mathbf{r}'|} d^3\mathbf{r}' + \oint_S \frac{\sigma_m(\mathbf{r}', t)}{|\mathbf{r} - \mathbf{r}'|} dS' \right] \quad (1.39)$$

where $\rho_m(\mathbf{r}', t) = -\nabla_{\mathbf{r}'} \cdot \mathbf{M}(\mathbf{r}', t)$ and $\sigma_m = \mathbf{M} \cdot \mathbf{n}$ are called the magnetic volume and surface charges respectively. V represents the volume of the magnet and S the surface that bounds the volume of the ferromagnet. Using Gauss's theorem¹⁴, we can rewrite equation 1.39 as

$$\Phi(\mathbf{r}, t) = \frac{1}{4\pi} \int_V \mathbf{M}(\mathbf{r}', t) \cdot \nabla_{\mathbf{r}'} \left(\frac{1}{|\mathbf{r} - \mathbf{r}'|} \right) d^3\mathbf{r}' \quad (1.40)$$

and thus the demagnetising field $\mathbf{H}_d(\mathbf{r}, t) = -\nabla_{\mathbf{r}}\Phi(\mathbf{r}, t)$ can be written as

$$\mathbf{H}_d(\mathbf{r}, t) = - \int_V \mathcal{N}(|\mathbf{r} - \mathbf{r}'|) \mathbf{M}(\mathbf{r}', t) d^3\mathbf{r}' \quad (1.41)$$

where the function $\mathcal{N}(|\mathbf{r} - \mathbf{r}'|) = \frac{1}{4\pi} \nabla_{\mathbf{r}} \nabla_{\mathbf{r}'} \frac{1}{|\mathbf{r} - \mathbf{r}'|}$ is called the demagnetisation tensor, written in its most general form. It is clear that \mathbf{H}_d is in fact given by a convolution of the demagnetisation tensor \mathcal{N} and the magnetisation \mathbf{M} . When the magnetisation inside a ferromagnet is in an uniform

¹⁴For a continuous vector field \mathbf{F} , we can write that $\int_V \nabla \cdot \mathbf{F} d^3\mathbf{r} = \oint_S \mathbf{F} \cdot \mathbf{n} dS$ with \mathbf{n} the normal on the surface S , bounding the volume V .

state, \mathbf{H}_d can be defined in terms of the magnetisation and a geometrical *dimensionless* tensor N (also called the demagnetisation tensor), resulting in an alternative definition of the magnetostatic field, whose components are then simply given by

$$H_{d,i} = -\sum_j N_{ij}M_j \quad (1.42)$$

The trace of the demagnetisation tensor N is given by $N_{xx} + N_{yy} + N_{zz} = 1$.

The energy related to the magnetostatic field \mathbf{H}_d can be written as

$$E_d = -\frac{1}{2} \int_V \mu_0 \mathbf{M}_s \cdot \mathbf{H}_d d^3\mathbf{r} \quad (1.43)$$

The factor $\frac{1}{2}$ is introduced to avoid double counting as in the energy the integral is performed over \mathbf{r} as well as \mathbf{r}' . Taking the functional derivative, we find that $\mathbf{H}_{\text{eff}} = \mathbf{H}_d$. Knowing that Φ and \mathbf{B} vanish at infinity, one can rewrite[3] this expression as an integral over whole space

$$E_d = \frac{1}{2} \int_{\text{space}} \mu_0 \mathbf{H}_d^2 d^3\mathbf{r} \geq 0 \quad (1.44)$$

which shows that this energy is always positive and can only be minimized by minimizing the whole demagnetising field, inside as well as outside¹⁵ the ferromagnet, as is shown in figure 1.7. As opposed to the exchange energy, this is a long ranged force as it couples every magnetic moment to another and is in general the energy term that requires the most computing time. In micromagnetic simulations, one can exploit the fact that the magnetostatic field is given by a convolution of the magnetisation with the demagnetisation tensor, as can be seen in equation 1.41. Also here a characteristic length scale (also called the exchange length) can be defined, given by $l_{\text{ex}} = \sqrt{\frac{2A_{\text{ex}}}{\mu_0 M_s^2}}$ which is approximately 5 nm for cobalt.

The demagnetisation tensor N is determined by the geometry of the magnet and can only be exactly calculated in some specific cases. For a thin infinite film with normal parallel to the z -axis, the only non vanishing component of N is given by $N_{zz} = 1$. Defining the magnetisation in spherical coordinates

¹⁵This is often called the stray field and is used in imaging magnetic domains, using magnetic force microscopy (MFM).

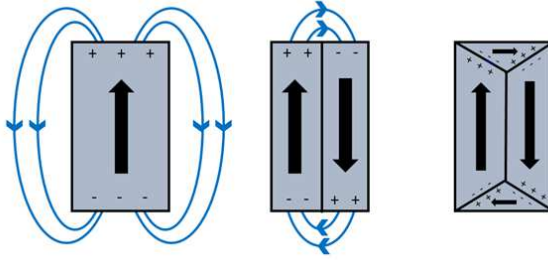


Figure 1.7: Stray field of a rectangular shaped ferromagnet. The demagnetisation energy is minimized by minimizing the magnetic surface charges. Left: highest magnetostatic energy. Right: flux closure state, lowest demagnetisation energy.

as $\mathbf{M} = M_s \sin(\theta) \cos(\phi) \mathbf{e}_x + M_s \sin(\theta) \sin(\phi) \mathbf{e}_y + M_s \cos(\theta) \mathbf{e}_z$, we can find that the magnetostatic energy in this case is given by

$$E_d = \frac{1}{2} \mu_0 V (N_{xx} M_x^2 + N_{yy} M_y^2 + N_{zz} M_z^2) \quad (1.45)$$

$$= \frac{1}{2} \mu_0 M_s^2 V \cos^2(\theta) \quad (1.46)$$

As this expression is equivalent to a first order uniaxial anisotropy (see equation 1.34) with $K_1 = -\frac{1}{2} \mu_0 M_s^2$, this is called shape anisotropy¹⁶ and pushes the magnetisation vector in the plane of the magnetic film. For a cobalt thin film, we find e.g. that $K_1 \approx -1.2 \times 10^6 \text{ J/m}^3$.

In the case of a uniform magnetised ellipsoid of revolution with long axis along the z -axis, we find that

$$E_d = \frac{1}{2} \mu_0 M_s^2 V (N_{zz} \cos^2(\theta) + N_{xx} \sin^2(\theta)) \quad (1.47)$$

as $N_{xx} = N_{yy}$ due to rotational symmetry or equivalently¹⁷

$$E_d = -\frac{1}{2} \mu_0 M_s^2 V (N_{xx} - N_{zz}) \cos^2(\theta) \quad (1.48)$$

dropping constant terms. For a sphere, we find $E_d = 0$ as $N_{xx} = N_{zz} = \frac{1}{3}$.

¹⁶A negative anisotropy constant leads to an easy plane (in this case the xy -plane) perpendicular to the uniaxial axis, i.e. the z -axis.

¹⁷Another form is $E_d = \frac{1}{2} \mu_0 M_s^2 V (1 - 3N_{xx}) \cos^2(\theta)$ as the trace of the demagnetisation tensor equals 1.

1.4.4 Zeeman energy

A ferromagnet will try to minimize its energy by aligning to an external field \mathbf{H}_{ext} . The Zeeman energy is given by

$$E_z = -\mu_0 \int_V \mathbf{M}_s \cdot \mathbf{H}_{\text{ext}} d^3 \mathbf{r} \quad (1.49)$$

which is the micromagnetic form of the atomistic Zeeman energy. The effective field, corresponding to this energy, is given by $\mathbf{H}_{\text{eff}} = \mathbf{H}_{\text{ext}}$.

1.4.5 Brown equations and Landau Lifshitz equation

Having discussed the most important energy terms, we can write the total energy functional $E[\mathbf{m}]$ as

$$E = - \int_V \mu_0 \mathbf{M}_s \cdot \left[\frac{A_{\text{ex}}}{\mu_0 M_s} \nabla^2 \mathbf{m} + \frac{K_1}{\mu_0 M_s} (\mathbf{u} \cdot \mathbf{m}) \mathbf{u} + \frac{\mathbf{H}_d[\mathbf{m}]}{2} + \mathbf{H}_{\text{ext}} \right] d^3 \mathbf{r}$$

and total effective field \mathbf{H}_{eff} as

$$\mathbf{H}_{\text{eff}} = - \frac{1}{\mu_0 M_s} \frac{\delta \epsilon}{\delta \mathbf{m}} = \frac{2A_{\text{ex}}}{\mu_0 M_s} \nabla^2 \mathbf{m} + \frac{2K_1}{\mu_0 M_s} (\mathbf{u} \cdot \mathbf{m}) \mathbf{u} + \mathbf{H}_d + \mathbf{H}_{\text{ext}}$$

considering only the first order uniaxial magnetocrystalline energy. Following Brown[9], the energy minimalisation of a magnetic system can be done by varying a magnetic configuration \mathbf{m} by a small amount $\delta \mathbf{m}$ and so $\mathbf{m} \rightarrow \mathbf{m} + \delta \mathbf{m}$. Using the variational principle that

$$\delta E = E[\mathbf{m} + \delta \mathbf{m}] - E[\mathbf{m}] = 0 \quad (1.50)$$

for linear terms in $\delta \mathbf{m}$, one can show that that the energy functional is extremal when following conditions¹⁸ are satisfied

$$\mathbf{m} \times \mathbf{H}_{\text{eff}} = \mathbf{0} \quad (1.51)$$

$$\frac{\partial \mathbf{m}}{\partial \mathbf{n}} = \mathbf{0} \quad (1.52)$$

using the constraint that $|\mathbf{m}| = 1$ and where \mathbf{n} represents the unit vector perpendicular to the surface S that is bounding the volume V . These equations are called the Brown equations[9] and were first derived in 1940.

¹⁸ $\frac{\partial \mathbf{m}}{\partial \mathbf{n}}$ is a rather formal notation and represents the derivative along the normal on the surface bounding the ferromagnet, i.e. $\frac{\partial \mathbf{m}}{\partial \mathbf{n}} = (\mathbf{n} \cdot \nabla) \mathbf{m}$.

The first condition is equivalent to demanding that the magnetic torque vanishes if the magnetic system is in equilibrium. As $\delta E = 0$ means that the energy is extremal, but not necessarily minimal, one also has to demand that $\delta^2 E \geq 0$. In reality, this amounts to calculating the first order and second order derivatives of the total energy. If the energy depends on multiple variables, one also has to evaluate the Hessian determinant.

The Brown equations tell us when a system is in equilibrium, but not how this can be reached. Classical physics teaches us however that the magnetisation M_s precesses in an effective magnetic field H_{eff} according to

$$\frac{\partial M_s}{\partial t} = -\gamma\mu_0 M_s \times H_{\text{eff}} \quad (1.53)$$

with $\gamma = \frac{2\mu_B}{\hbar} = 1.76 \times 10^{-11} \text{ T}^{-1}\text{s}^{-1}$ the absolute value of the gyromagnetic ratio of an electron. This equation does not lead to equilibrium however as it does not contain any dissipative terms. Due to electron - phonon interactions or due to the interaction with impurities in the lattice, the precession of the magnetisation will be damped and spiral towards the effective field as is shown in figure 1.8. The evolution of M_s is described by the Landau - Lifshitz (LL) equation

$$\frac{\partial M_s}{\partial t} = -\gamma_L \mu_0 M_s \times H_{\text{eff}} - \frac{\lambda \mu_0}{M_s} M_s \times (M_s \times H_{\text{eff}}) \quad (1.54)$$

where γ_L is the LL gyromagnetic ratio¹⁹ and λ a damping parameter.

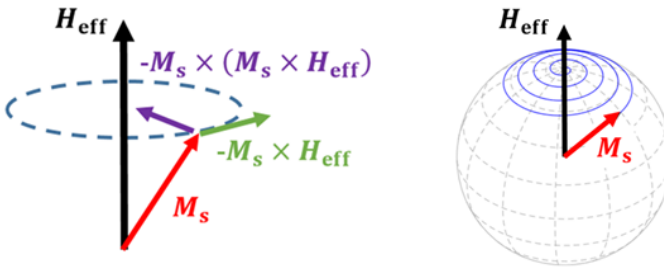


Figure 1.8: Left: The first term in the LL equation 1.54 leads to precession of the magnetisation vector around the effective field while the second term includes dissipative effects. Right: Due to a combination of precession and damping, the magnetisation will spiral towards the effective field.

¹⁹The reason for this notation will become clear in equation 1.57.

There exists also another, less intuitive form of the LL equation 1.54, which is called the Landau - Lifshitz - Gilbert (LLG) equation

$$\frac{\partial \mathbf{M}_s}{\partial t} = -\gamma \mu_0 \mathbf{M}_s \times \mathbf{H}_{\text{eff}} + \frac{\alpha}{M_s} \mathbf{M}_s \times \frac{\partial \mathbf{M}_s}{\partial t} \quad (1.55)$$

with α is a phenomenological dimensionless damping parameter, typically of the order 0.01 to 0.3. Both equations can be transformed to the other however. By calculating $\mathbf{M}_s \times \frac{\partial \mathbf{M}_s}{\partial t}$ of equation 1.55, we find

$$\mathbf{M}_s \times \frac{\partial \mathbf{M}_s}{\partial t} = -\gamma \mu_0 \mathbf{M}_s \times (\mathbf{M}_s \times \mathbf{H}_{\text{eff}}) - \alpha M_s \frac{\partial \mathbf{M}_s}{\partial t} \quad (1.56)$$

as the norm of the magnetisation vector is conserved, i.e. $\frac{\partial |\mathbf{M}_s|^2}{\partial t} = 0$. Substituting this expression in equation 1.55 again, we can rewrite the LLG equation in the *form* of the Landau - Lifshitz equation

$$\frac{\partial \mathbf{M}_s}{\partial t} = -\frac{\gamma \mu_0}{1 + \alpha^2} \mathbf{M}_s \times \mathbf{H}_{\text{eff}} - \frac{\alpha \gamma \mu_0}{M_s (1 + \alpha^2)} \mathbf{M}_s \times \mathbf{M}_s (\times \mathbf{H}_{\text{eff}}) \quad (1.57)$$

Comparing 1.54 with 1.57, we can see that in the case of low damping, both equations behave the same with $\gamma = \gamma_L$ and $\lambda = \gamma \alpha$. For high damping however, we find for the LL equation that $\frac{\partial \mathbf{M}_s}{\partial t} \rightarrow \infty$ for $\lambda \rightarrow \infty$, but on the other hand for the LLG equation that $\frac{\partial \mathbf{M}_s}{\partial t} \rightarrow 0$ for $\alpha \rightarrow \infty$. The former is unphysical however as one would expect a slower time evolution for a larger damping. In conclusion, the LLG as well as the LL equation describe the same evolution for small damping constants, but in systems with high damping the LLG equation is more physical.

1.5 Magnetic domains and hysteresis

If only exchange energy would exist, the ferromagnet would always be in a uniform state and micromagnetics would be a rather boring field in physics as there would be little to explore. Taking into account demagnetisation energy however gives rise to complex, but interesting magnetic structures. As can be seen in equation 1.44, the only way to minimize the demagnetisation energy is by eliminating the magnetostatic field, which can only be done by avoiding the magnetic volume and surface charges, i.e. the divergence of the magnetisation inside the ferromagnet has to vanish and the magnetisation has to be parallel to the boundaries. On its turn, this increases the

exchange energy as the magnetisation will have to rotate inside the magnet and domain walls will need to be formed. Energy minimalisation in micromagnetics is thus a fragile equilibrium between minimizing the magnetostatic energy on the one hand and exchange energy on the other hand. This gives rise to the formation of magnetic domains. Taking into account other energy terms such as the magnetocrystalline energy, will only lead to a higher degree of complexity.

In ferromagnets with a finite size, such as squares and disks on the order of $1\ \mu\text{m}$, this equilibrium between the demagnetisation energy and the exchange energy leads to the typical flux closure state, called the Landau domain structure as can be seen in figures 1.9a and 1.9b. In the middle of these nanostructures, the magnetisation is obliged to rotate out of the plane due to the exchange energy and thus gives rise to a magnetic vortex core. This vortex, which is a topologically stable entity, is characterized by a polarisation (in or out of the plane) and a rotation sense (clockwise or counter clockwise). Magnetic domains can be imaged with techniques such as magnetic force microscopy (MFM). The magnetic contrast in a MFM image is proportional to the second derivative of the stray field, generated outside the sample. A typical MFM image of a permalloy ($\text{Ni}_{80}\text{Fe}_{20}$ alloy) nanosquare is shown in figure 1.9c. Although the vortex core in the middle of the square cannot be resolved as the lateral resolution of a standard MFM tip is approximately 30 nm, the domain walls are clearly visible.

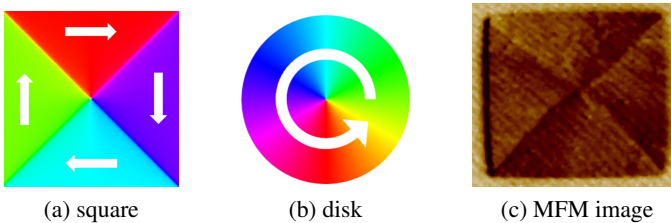


Figure 1.9: Figure (a): Micromagnetic simulation of a Landau domain in a magnetic square (size = $2\ \mu\text{m}$) with a vortex core in the middle. The white arrow indicates the direction of the magnetisation. Figure (b): flux closure state in a nanodisk and simultaneously indicating the colour scale (in plane magnetisation) used in MuMax³. The magnetisation vector is tangent to a circle. Figure (c): MFM image of a magnetic nanosquare.

When measuring the magnetisation m as a function of the external field $B_{\text{ext}} = \mu_0 \mathbf{H}_{\text{ext}}$, one often finds a hysteresis effect, indicating that the magnetic state of a system depends on its history. An out-of-plane hysteresis loop of a CoPt multilayer can be seen in figure 1.10. Due to the high magnetocrystalline anisotropy of CoPt, perpendicular to the thin film, it is energetically favourable for the magnetisation to be oriented out of the plane, although the demagnetisation energy favours an in-plane direction. Typical associated parameters with a field loop are the coercivity $B_c = \left| \frac{B_{c,1} - B_{c,2}}{2} \right|$ which equals the half of the width of the hysteresis loop, the remanence m_r which is the magnetisation at vanishing external field and (if applicable) the shift $B_{\text{cb}} = \left| \frac{B_{c,1} + B_{c,2}}{2} \right|$ of the hysteresis loop. The shift usually vanishes, unless under specific circumstances such as exchange bias, which will be discussed in the next chapter. The exact shape of the hysteresis loop depends along which crystallographic axis the external field is applied, deposition conditions, defects,...

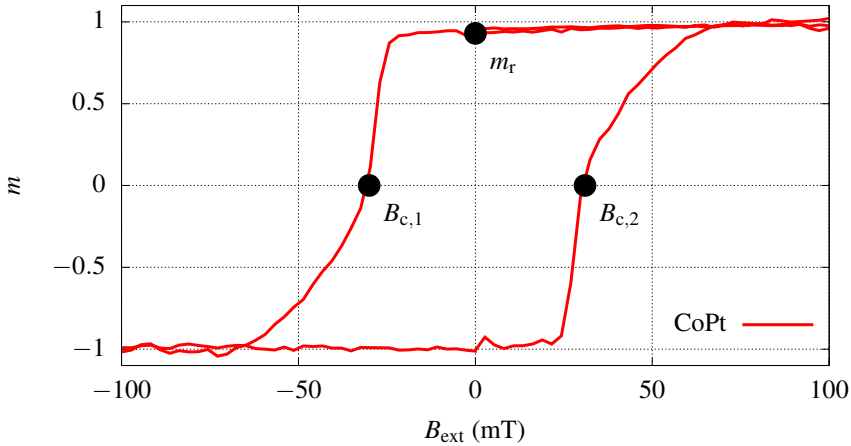


Figure 1.10: Experimental out-of-plane hysteresis loop of a $[\text{Co}(1\text{nm})\text{Pt}(1\text{nm})]_{20}$ multilayer. Due to the strong perpendicular anisotropy, the magnetisation favours an out-of-plane orientation which leads to a high coercivity $B_c \approx 30$ mT and high remanence $m_r \approx 1$. In this case no shift is present, i.e. $B_{\text{cb}} = 0$ mT.

1.6 Stoner Wohlfarth model

The Stoner Wohlfarth model[10] (1948) is one of the most simple magnetic systems that can be solved analytically, but clearly demonstrates the concepts of hysteresis, coercivity, irreversibility and the complex nature of magnetism. Analogous techniques will be used when discussing the interfacial interaction between a ferromagnet and an antiferromagnet.

In this model[11], one considers a uniform magnetised elliptical particle with uniaxial anisotropy²⁰ or (in this case equivalently) a uniform in-plane magnetised thin film with a magnetocrystalline anisotropy axis. We will assume that the magnetisation vector rotates coherently which is only the case for small particles and that the anisotropy axis coincides with the long axis of the particle.

Taking into account uniaxial anisotropy and Zeeman energy, we can write the total energy density of such a particle as

$$\epsilon(\beta) = -K_{\text{FM}} \cos^2(\beta) - \mu_0 H_{\text{ext}} M_{\text{FM}} \cos(\beta - \gamma) \quad (1.58)$$

where β is the angle that the magnetisation vector makes with respect to the uniaxial axis and γ is the angle that the external field H_{ext} makes with respect to the uniaxial axis, as can be seen in figure 1.11.

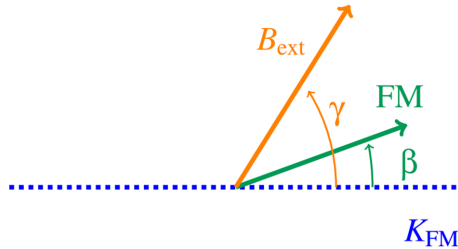


Figure 1.11: Definition of the angles β and γ that the FM magnetisation vector and the external field make with the uniaxial anisotropy axis K_{FM} .

²⁰For a uniform magnetised elliptical particle, the anisotropy constant K_{FM} is induced by shape anisotropy with easy axis along the long axis of the ellipsoid, as can be seen in equation 1.48. If applicable, one can also take into account magnetocrystalline anisotropy when its easy axis coincides with the long principal axis of the ellipsoid. In that case, K_{FM} represents some effective value.

To determine the angles β^* , which correspond to the stable equilibria positions of the magnetisation vector of the FM particle, one has to find the extrema of the energy density, together with the requirement that the energy is minimal

$$\frac{\partial \varepsilon}{\partial \beta} = \sin(\beta^*) \cos(\beta^*) + h \sin(\beta^* - \gamma) = 0 \quad (1.59)$$

$$\frac{\partial^2 \varepsilon}{\partial \beta^2} = \cos(2\beta^*) + h \cos(\beta^* - \gamma) > 0 \quad (1.60)$$

where we have introduced the dimensionless variable $h = \frac{\mu_0 H_{\text{ext}} M_{\text{FM}}}{2K_{\text{FM}}}$.

For reasons of clearness, we will first take a look at the cases $\gamma = 0$ and $\gamma = \frac{\pi}{2}$ to demonstrate the physics of this model. Afterwards, we will solve it for arbitrary angles γ .

Case 1: $\gamma = 0$

The solutions of equation 1.59 are given by $\beta^* = 0$ and $\beta^* = \pi$, corresponding to positive and negative saturation respectively. The stability requirement shows that $\beta^* = 0$ is minimal for $h > -1$ and $\beta^* = \pi$ is minimal for $h < 1$. The third solution $\cos(\beta^*) = -h$ can only exist for $|h| < 1$, but due to the condition $h^2 - 1 > 0$ this is an energy maximum and so this solution can be discarded. This leads to the conclusion that for $\gamma = 0$ the hysteresis loop is rectangular with switching fields $\mu_0 H_{c,1} = -\frac{2K_{\text{FM}}}{M_{\text{FM}}}$ and $\mu_0 H_{c,2} = \frac{2K_{\text{FM}}}{M_{\text{FM}}}$ as can be seen in figure 1.12 (red line).

This also clearly demonstrates that the state of a magnetic system depends on its history as in the region $|h| < 1$ both solutions are stable. The energy landscape for different magnitudes of the external field ($\gamma = 0$) is shown in figure 1.13. At positive saturation ($h = 2$) only 1 minimum is present, i.e. $\beta^* = 0$. For decreasing but still positive external fields ($0 < h < 1$) however, $\beta^* = \pi$ becomes a relative minimum. For $-1 < h < 0$, the position $\beta^* = \pi$ becomes the absolute minimum and when the external field reaches the switching field ($h = -1$), the energy barrier disappears and the magnetisation vector will switch from the position $\beta^* = 0$ towards the position $\beta^* = \pi$, i.e. from positive towards negative saturation. This switching is an irreversible transition. Remark also that the energy curves corresponding to the external fields $\pm h$ are shifted by 180° with respect to each other as $\varepsilon(-h, \beta) = \varepsilon(h, \pi \pm \beta)$.

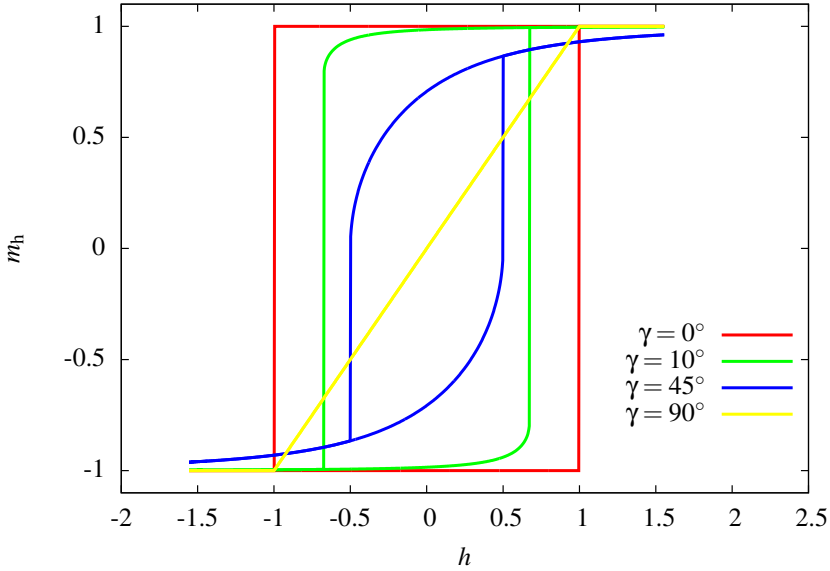


Figure 1.12: Simulated hysteresis loops corresponding to the Stoner Wohlfarth model. Different curves correspond to different angles γ that the external field makes with respect to the anisotropy axis. m_h represents the magnetisation projected on the external field. Looking to the case of an in-plane magnetised thin infinite film, typical values for cobalt were used, i.e. $M_{\text{FM}} = 1400 \text{ kA/m}$ and $K_{\text{FM}} = 4.5 \times 10^5 \text{ J/m}^3$.

The coercivity of the hysteresis loop for $\gamma = 0$ is given by

$$B_c = \mu_0 \left| \frac{H_{c,1} - H_{c,2}}{2} \right| = \frac{2K_{\text{FM}}}{M_{\text{FM}}} \quad (1.61)$$

which is often called the anisotropy field in literature.

Case 2: $\gamma = \frac{\pi}{2}$

In the case $\gamma = \frac{\pi}{2}$, i.e. when the magnetic field is perpendicular to the easy axis, we find that $\beta^* = \frac{\pi}{2}$ is an energy minimum for $h > 1$, $\beta^* = -\frac{\pi}{2}$ for $h < -1$ and $\sin(\beta^*) = h$ for $|h| < 1$. As $\sin(\beta^*)$ represents the component parallel to the magnetic field, the field loop is a straight line along the diagonal for $|h| < 1$ as can be seen from the yellow line in figure 1.12.

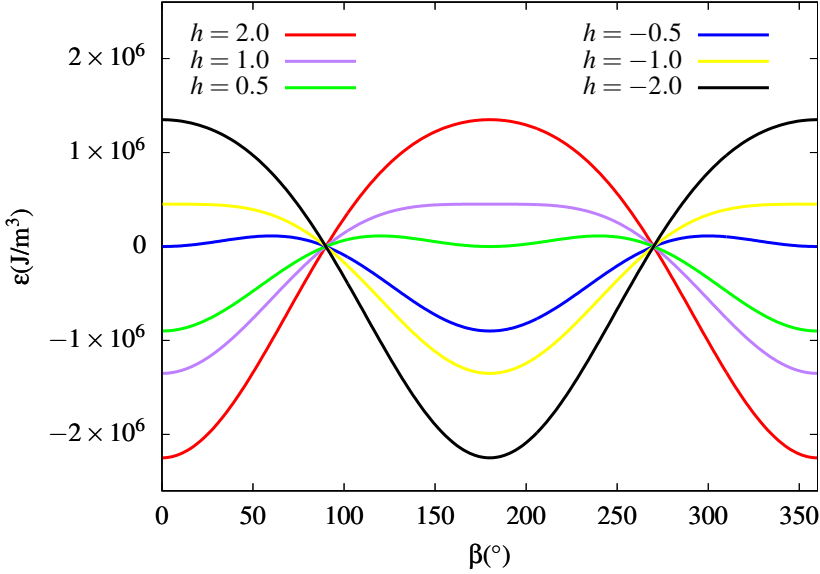


Figure 1.13: Simulated energy landscape for different values of h with $\gamma = 0$. Typical values for a thin infinite cobalt film with an in-plane anisotropy were used, i.e. $M_{\text{FM}} = 1400 \text{ kA/m}$ and $K_{\text{FM}} = 4.5 \times 10^5 \text{ J/m}^3$.

Case 3: general angles γ

For general angles γ , the hysteresis loops will be between these 2 extremes. Solving the stability equations 1.59, one finds (see appendix A) that the magnitude of the switching field is given by

$$h = \left[\frac{1}{\cos^{\frac{2}{3}}(\gamma) + \sin^{\frac{2}{3}}(\gamma)} \right]^{\frac{3}{2}} \quad (1.62)$$

One can easily see that for $\gamma = \frac{\pi}{4}$, the coercivity is only half of its maximal attainable value, i.e. the anisotropy field. Hysteresis loops for different angles γ are shown in figure 1.12.

1.7 Micromagnetic modelling using MuMax³

Analytical solutions for micromagnetic problems are very rare and limited, even when examining (seemingly) simple models such as the Stoner Wohlfarth model, discussed in the previous section. When studying ferromagnets which have a finite size, so the demagnetisation energy cannot be expressed as a simple shape anisotropy anymore, or when considering a sample, existing of many grains with different anisotropy axes, one has to resort to numerical methods.

In this thesis, we will use MuMax³[12] as a micromagnetic simulation program. This open source software²¹ relies on a finite difference discretisation to solve the LLG equation in the form as given in 1.57 and in fact only requires a NVIDIA GPU. More details about the GPU-optimisation of MuMax³ can be found in [13].

²¹For more information, visit our website <http://mumax.github.io/>

ANTIFERROMAGNETS AND EXCHANGE BIAS

*A new type of magnetic anisotropy has been discovered
which is best described as an exchange anisotropy.
This anisotropy is the result of an interaction between
an antiferromagnetic material and a ferromagnetic material.*

Meiklejohn and Bean, *New Magnetic Anisotropy*[14]

2.1 Antiferromagnets

When discussing the Heisenberg exchange interaction (equation 1.29), we have noticed that a negative exchange integral J leads to an antiferromagnetic (AFM) ordering of neighbouring spins. An antiferromagnet such as CoO or NiO can be seen as consisting of 2 sublattices which are coupled antiparallel, so no net macroscopic magnetisation is present and no magnetostatic field is generated. Analogous to ferromagnets, one can calculate[3] the susceptibility χ_m in the paramagnetic regime

$$\chi_m = \frac{C'}{T + \theta_N} \quad (2.1)$$

with θ_N in most cases a positive constant. Experiments show that antiferromagnetic ordering happens under a specific temperature, called the Néel temperature, not equal to θ_N . More interesting in our case, is the susceptibility of an antiferromagnet at low temperatures $T \ll T_N$. Considering that an antiferromagnet can be described by 2 sublattices M_1 and M_2 , their energy in an external field B_{ext} is given by

$$E = \lambda M_1 \cdot M_2 - B_{\text{ext}} \cdot (M_1 + M_2) \quad (2.2)$$

assuming $\lambda > 0$, $|\mathbf{M}_1| = |\mathbf{M}_2| = M$ and a high anisotropy along its Néel axis¹. The first term in equation 2.2 describes the interaction between the 2 sublattices and the second term the coupling of the sublattices to the external field. Defining ϕ as the angle that the sublattices make with the Néel axis (figure 2.1) and assuming the external field is applied perpendicular to the Néel axis, we find for small canting angles ϕ that

$$E = \lambda M^2 \cos(\pi - 2\phi) - 2MB_{\text{ext}} \sin(\phi) \quad (2.3)$$

$$\approx -\lambda M^2 (1 - 2\phi^2) - 2MB_{\text{ext}}\phi \quad (2.4)$$

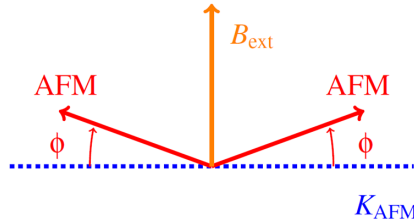


Figure 2.1: Canting of the AFM sublattices in an external field B_{ext} .

Stability requires $\frac{dE}{d\phi} = 0$ and so we find as solution $\phi^* = \frac{B_{\text{ext}}}{2\lambda M}$. The second derivative shows that this is always an energy minimum. Defining $\chi_{\perp} = \frac{M_{\text{tot},\perp}}{B_{\text{ext}}}$ with $M_{\text{tot},\perp} = 2M \sin(\phi^*) \approx 2M\phi^*$ due to the presence of the 2 sublattices, we find for the perpendicular susceptibility that $\chi_{\perp} \approx \frac{1}{\lambda}$, which is approximately constant as can also be seen in figure 2.2.

In case a strong magnetic field is applied parallel to a *weak anisotropy* axis of an AFM, the 2 sublattices will orient themselves perpendicular to the anisotropy axis to minimize the total energy of the system. This phenomenon is called the *spin flop* transition[15]. Experiments have shown that also another metamagnetic transition, called the *spin flip* transition, can occur. If a magnetic field, applied along an axis with *strong anisotropy*, reaches some critical value, the 2 (originally antiparallel) AFM sublattices will orient themselves parallel in the field direction. In the case of TbCu_2 , one has observed this spin flip transition in magnetic fields higher than 2T, if applied along the crystallographic $\langle 100 \rangle$ direction[16].

¹If 2 AFM sublattices are perfectly antiparallel to each other, the Néel axis is defined as the axis parallel to a spin direction of the AFM sublattices.

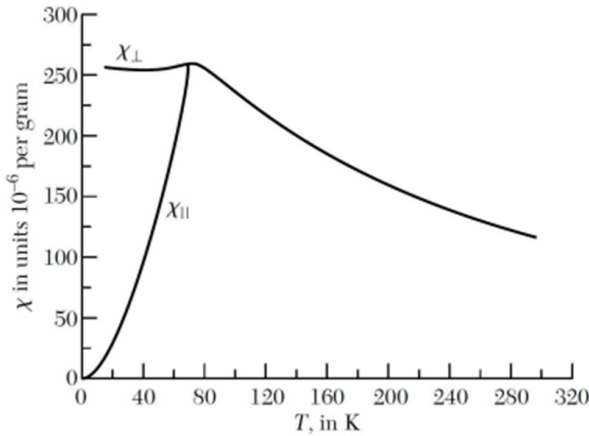


Figure 2.2: Susceptibility of the antiferromagnetic MnF_2 . [17] The kink in the curve happens at the Néel temperature T_N . χ_{\perp} represents the perpendicular susceptibility and χ_{\parallel} the susceptibility if the magnetic field is applied parallel to the Néel axis. The susceptibility of a polycrystalline antiferromagnet will be a combination of both.

Due to the specific antiparallel ordering of spins in an antiferromagnet, a crystallographic plane can be compensated or uncompensated, depending on whether, respectively, both AFM sublattices or only one sublattice is present in this plane. In CoO for example (figure 2.3), the (111) plane, indicated by the grey triangle, is uncompensated and (100) plane compensated. A perfect uncompensated interface has a net magnetic moment which can couple to a ferromagnet whereas a compensated interface can give rise to spin flop coupling, very similar to the spin flop effect as discussed above.

2.2 Discovery of exchange bias

In 1956, Meiklejohn and Bean [14, 19] made a surprising discovery while studying small Co nanoparticles (size 10 - 100 nm) with a CoO shell, obtained through oxidation. When cooling these particles in a magnetic field to a temperature (in this case 77 K) below T_N , they observed a unidirectional shift of the hysteresis loop as can be seen in figure 2.4, left (solid line). When no magnetic field was applied during cooling, no shift was found (dashed line in figure 2.4, left) and so the loop was centered around $H_{\text{ext}} = 0$.

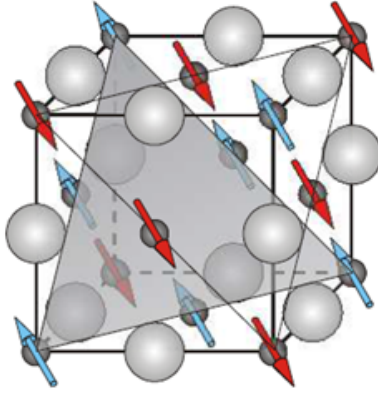


Figure 2.3: Antiferromagnetic ordering in CoO (NaCl structure). The spins belonging to the same AFM sublattice are drawn in the same colour. The (111) planes are uncompensated and (100) planes are compensated. Similar ordering is also present in NiO and MnO. Reproduced from [18].

While measuring the average magnetic torque τ (figure 2.4, right, curve (b)) for a collection of randomly oriented particles in a very strong magnetic field, they found that

$$\tau(\theta) = -\frac{\partial \epsilon}{\partial \theta} = -K_{\text{ex}} \sin(\theta) \quad (2.5)$$

where θ represents the angle between the magnetisation and the cooling field direction. By integrating this equation, one finds that the energy density linked to this torque is given by

$$\epsilon(\theta) = -K_{\text{ex}} \cos(\theta) \quad (2.6)$$

which shows that the only energy minimum is given by $\theta^* = 0$. This cannot be explained by a uniaxial anisotropy for which $\epsilon(\theta) = -K_{\text{FM}} \cos^2(\theta)$ and the energy minima are given by $\theta^* = 0$ and $\theta^* = \pi$.

They explained this (in their own words) *new magnetic anisotropy*[14, 19] by considering frozen uncompensated spins at the interface between the ferromagnetic Co and antiferromagnetic CoO.

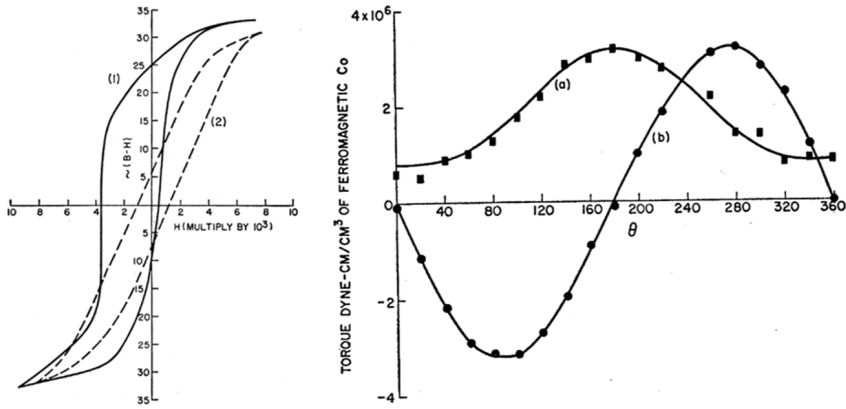


Figure 2.4: Left: Solid line represents the field cooled hysteresis loop as obtained by Meiklejohn and Bean. A shift is clearly present. Dashed line is zero field cooled case. Right, curve (b): average torque measurement varies as $\sin(\theta)$ with θ the angle between the field cooling direction and the external field. Reproduced from [19].

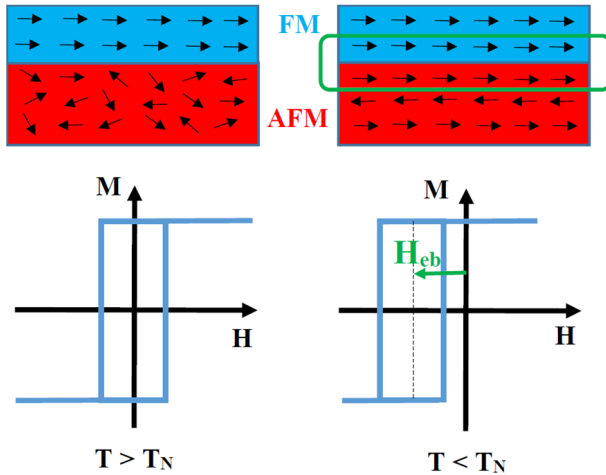


Figure 2.5: Exchange bias due to the coupling of a FM with an uncompensated AFM interface. Left: Above the Néel temperature T_N , no anti-ferromagnetic ordering is present. Right: When the AFM is cooled in an external field below T_N , a shift H_{eb} of the hysteresis loop is induced as the AFM spins stay pinned during a reversal of the FM due to a high anisotropy.

When cooling an uncompensated AFM/FM bilayer in an external field below the Néel temperature (figure 2.5), the uncompensated AFM spins at the interface, coming from a paramagnetic state, will orient themselves parallel² to the saturated ferromagnet in the direction of the cooling field. Assuming these AFM spins are afterwards frozen in this configuration due to a high anisotropy, they give rise to a unidirectional anisotropy, shifting the hysteresis loop antiparallel to the field cooling direction, in case of positive as well as negative coupling constants between the FM and the AFM.

Including this new energy term, we can write the total surface energy density σ of a ferromagnetic layer³ (thickness t_{FM} and anisotropy constant K_{FM}) in an external field H_{ext} as

$$\sigma = -\mu_0 H_{\text{ext}} M_{\text{FM}} t_{\text{FM}} \cos(\beta) - K_{\text{FM}} t_{\text{FM}} \cos^2(\beta) - J_{\text{I}} \cos(\beta) \quad (2.7)$$

assuming the uniaxial anisotropy axis of the ferromagnet is parallel to the field cooling direction and labeling this as the reference direction. As this apparent shift of the hysteresis loop is an interface effect, we have introduced the parameter $J_{\text{I}} = K_{\text{ex}} t_{\text{FM}}$ as the surface energy density, related to the interaction between the ferromagnet and antiferromagnet.

Stability conditions show that the coercivity B_{c} (as defined in the Stoner Wohlfarth model in section 1.6 and figure 1.10) and the bias field B_{eb} , representing the shift of the hysteresis loop, are given by

$$B_{\text{c}} = \left| \frac{B_{\text{c},1} - B_{\text{c},2}}{2} \right| = \frac{2K_{\text{FM}}}{M_{\text{FM}}} \quad (2.8)$$

$$B_{\text{eb}} = \left| \frac{B_{\text{c},1} + B_{\text{c},2}}{2} \right| = \frac{J_{\text{I}}}{M_{\text{FM}} t_{\text{FM}}} \quad (2.9)$$

This shows that a unidirectional anisotropy gives rise to a shifted hysteresis loop. To derive a theoretical expression for the bias field, we have assumed that the external field was applied parallel to the field cooling direction and thus the spin direction of the frozen uncompensated AFM spins. Clearly, there is no reason why this condition should be satisfied in experiments, nor does it impose any fundamental restrictions in a theoretical or micromagnetic model.

²Assuming a positive coupling constant between the ferromagnet and antiferromagnet.

³Not taking into account demagnetisation energy

A more detailed analysis[20] shows that in antiferromagnets with a high anisotropy, the angular dependence of the bias field can be described as

$$B_{\text{eb}}(\theta_{\text{uc}}) = -\frac{J_{\text{I}}}{M_{\text{FM}}t_{\text{FM}}} \cos(\theta_{\text{uc}}) \quad (2.10)$$

where θ_{uc} is the angle between the direction of the frozen uncompensated AFM spins and the direction corresponding to positive values of the external field. One can easily see that the bias field vanishes if both are perpendicular ($\theta_{\text{uc}} = \frac{\pi}{2}$), as in this case the symmetry between the direction of the external field and the direction of the frozen AFM spins is not broken.

It is also important to note that the terminology of *negative* exchange bias, as follows from this simple model, means that the hysteresis loop is shifted in a direction antiparallel to the field cooling direction. This does not necessarily mean antiparallel with respect to the direction corresponding to positive values of the external field, as this has no real physical meaning. In case $\theta_{\text{uc}} = \pi$ (equation 2.10), the hysteresis loop would be shifted towards positive values of H_{ext} for $J_{\text{I}} > 0$, but still antiparallel with respect to the field cooling direction. The case of *positive* exchange bias fields will be discussed in section 3.7.

In the model of Meiklejohn and Bean (equation 2.7), one assumes that the uncompensated AFM macrospin has an infinite anisotropy and so cannot rotate or make an irreversible transition, i.e. switch together with the FM macrospin during reversal. As this simple model cannot explain some additional effects which are often observed after field cooling, e.g. the enhanced coercivity of the exchange biased loop in figure 2.4, a more advanced model[20] is needed. This will be discussed in section 3.2, together with its implementation in MuMax³.

2.3 Alternative models for exchange bias

Historically, the shift of the hysteresis loop was explained by Meiklejohn and Bean due to the presence of fixed uncompensated spins at the FM/AFM interface. Even though this remains the basic idea up to this day, other mechanisms are available to generate exchange bias or a shifted loop. It is clear however that every model should break uniaxial symmetry, whether it be due to the exchange interaction at the interface or the presence of another macroscopic effective field in the ferromagnet.

2.3.1 Mauri model

As the exchange stiffness inside an antiferromagnet is typically almost an order lower than the exchange stiffness inside a ferromagnet, Mauri[21] assumed it is energetically more favourable to form a domain wall in the AFM (figure 2.6), rotating parallel to the FM/AFM interface.

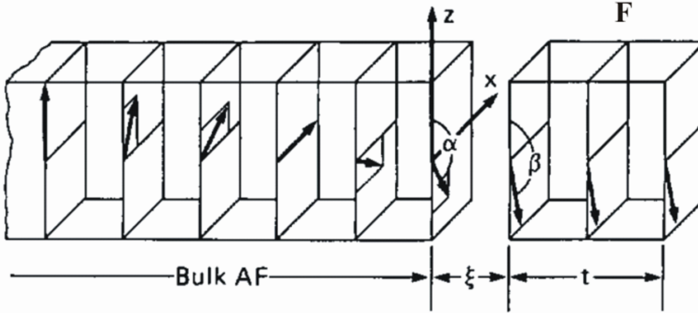


Figure 2.6: Formation of a planar domain wall in the AFM, according to the model of Mauri[21]. t is the thickness of the FM layer and ξ is the interface region between the FM and the AFM. The uniaxial anisotropy of the AFM is parallel to the z -axis. Only one AFM sublattice is shown.

The total surface energy density in this model is given by

$$\begin{aligned} \sigma(\beta, \phi) = & -\mu_0 H_{\text{ext}} M_{\text{FM}} t_{\text{FM}} \cos(\gamma - \beta) - J_1 \cos(\beta - \alpha) \\ & + J_A (1 - \cos(\alpha)) \end{aligned} \quad (2.11)$$

with γ and β the angles that the external field and the FM macrospin make with respect to the uniaxial AFM anisotropy axis (z -axis) and α the twist angle of an AFM sublattice. The first term in equation 2.11 is the Zeeman energy of the FM layer, the second term is the interface interaction between the FM and the uncompensated AFM macrospin and the last term corresponds to the domain wall energy in case of an infinite thick antiferromagnet. The constant $J_A = 2\sqrt{A_{\text{AFM}}K_{\text{AFM}}}$ is the surface energy density needed to rotate the AFM domain wall over an angle⁴ of 90° . The parameters A_{AFM} and K_{AFM} are the exchange stiffness and the uniaxial anisotropy constant of the antiferromagnet, respectively. The Mauri model takes into

⁴The surface energy difference between the positions $\alpha = 0$ and $\alpha = \pi$ is then given by $4\sqrt{A_{\text{AFM}}K_{\text{AFM}}}$.

account the anisotropy energy of the AFM by considering the domain wall energy and it allows for a rotation of the AFM spins, moving away from the infinite AFM anisotropy model of Meiklejohn and Bean (equation 2.7). For a Co(2.5nm)/NiO bilayer, one finds[22] that $J_A \approx 0.66 \text{ mJ/m}^2$. One can show[20] that the bias field B_{eb} is given by

$$B_{\text{eb}} = - \frac{J_I J_A}{M_{\text{FM}} t_{\text{FM}} \sqrt{J_I^2 + J_A^2}} \quad (2.12)$$

Because only unidirectional energy terms are present in this model and so $B_c = 0$, it cannot explain the enhanced coercivity in an exchange biased hysteresis loop and it can only be applied in case of low anisotropy constants K_{AFM} , as otherwise no domain wall is formed in the antiferromagnet. We will discuss this model in greater detail in section 3.2, together with a more advanced Meiklejohn and Bean model.

2.3.2 Malozemoff model

In this model[23] one takes into account the roughness of the FM/AFM interface due to alloying, resulting into a random distribution of uncompensated AFM spins at the interface and thus local variations in the bias field. Malozemoff[23] proposes that, in order to minimize this interface interaction, the antiferromagnet breaks up into several frozen domains, separated by frozen domain walls, perpendicular to the interface. He proved that these antiferromagnetic domains have a characteristic length scale given by $L_D = \pi \sqrt{\frac{A_{\text{AFM}}}{K_{\text{AFM}}}}$, determined by the interplay between the magnetocrystalline anisotropy and exchange energy. He then argued that the local interface energy density is given by $J_I = \pm \frac{z\lambda}{a^2}$ with z a factor of the order unity depending on the position of the defect, λ an exchange constant⁵ and a the lattice constant of the antiferromagnet. Averaging J_I over a domain of the size L_D leads to a net surface energy density. As an expression for the bias field, he finds that

$$B_{\text{eb}} = \frac{2z\sqrt{A_{\text{AFM}}K_{\text{AFM}}}}{\pi^2 M_{\text{FM}} t_{\text{FM}}} \quad (2.13)$$

which is very similar to what was found in the model of Mauri if $J_I \gg J_A$.

⁵Unit of λ is Joules

2.3.3 Summary of models producing exchange bias

A schematic representation of the Meiklejohn and Bean model, the Mauri model and the model of Malozemoff is shown in figure 2.7.

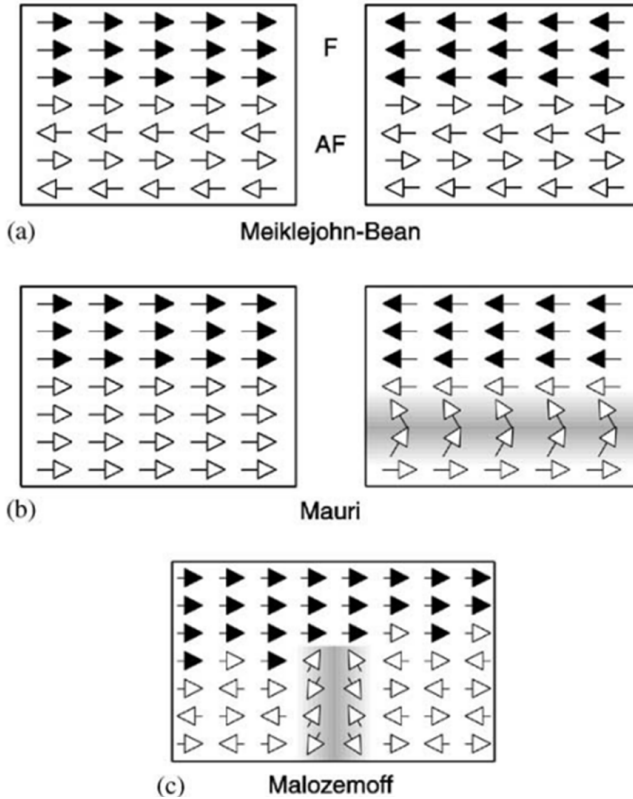


Figure 2.7: Possible mechanisms to generate exchange bias. (a) Meiklejohn and Bean model: frozen uncompensated AFM spins at the FM/AFM interface. (b) Mauri model: planar AFM domain wall. (c) Malozemoff model: exchange bias due to interfacial roughness. The grey area in (b) and (c) represents the AFM domain wall. Remark that in the Mauri model the domain wall rotates parallel to the FM/AFM interface. Reproduced from [24].

2.3.4 Positive and negative loop shifts

Experiments[25] have shown that if the FM has a net remanent state m_r at a temperature $T \approx T_N$, one can tune the direction of the loop shift and the magnitude of the bias field without applying an external field when cooling the sample. When sputtering a FM material while applying an external field on the substrate, one can induce a uniaxial anisotropy in the FM. This can result in a net remanent state of the FM, which then applies a net effective field on the AFM. Due to the coupling between the FM and AFM, the uncompensated AFM spins will be oriented in a direction parallel to the FM, in case of a parallel interface coupling. While cooling the sample, some of these uncompensated AFM spins become frozen, thus leading to a macroscopic exchange bias field. Depending if the average remanent state of the FM was parallel or antiparallel with respect to the external field during a field sweep, one can thus obtain negative as well as positive loop shifts.

The bias field as a function of the remanent⁶ state m_r for a Co/CoO bilayer is shown in figure 2.8. This demonstrates that if the average remanence $m_r \approx 0$, one can in fact obtain a bias field $B_{\text{eb}} \approx 0$ and indicates that the interface interaction between the FM and the AFM is more important than the influence of an external field on the AFM layer. The purpose of the cooling field is thus to saturate the FM rather than aligning the uncompensated AFM spins. This justifies the approximation that we can neglect the Zeeman energy of the AFM in case of low magnetic fields.

2.3.5 Loop shift due to the DMI interaction

Apart from the creation of a domain wall in the AFM or pinning AFM spins due to a high anisotropy, also other mechanisms are available for producing shifted hysteresis loops, even at compensated AFM interfaces. An example of such a mechanism is the Dzyaloshinskii-Moriya interaction[26, 27, 28] (DMI). This higher order exchange interaction is only present in systems with a broken inversion symmetry and arises from the spin orbit coupling. In FM/AFM perovskite⁷ structures for example, the distortion of the lattice leads to a displacement of the oxygen atoms, perpendicular to the connection between the FM - AFM bond, as is shown in figure 2.9(b).

⁶The remanent state m_r was measured around the Néel temperature $T_N \approx 300$ K of CoO.

⁷The structure of perovskites is given by ABX_3 where X is typically oxygen, A a smaller and B a larger cation. An example of a perovskite is the antiferromagnetic LaFeO_3 .

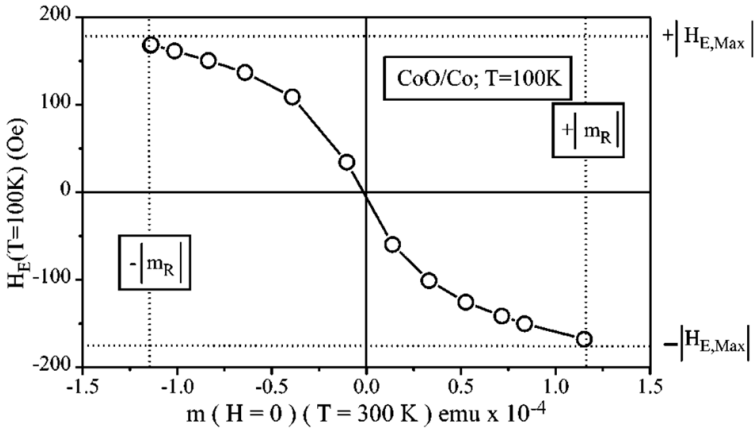


Figure 2.8: Evolution of the exchange bias field (here labeled as H_E) in a Co/CoO bilayer, measured at a temperature of 100 K, as a function of the remanent state $m_r = m(H = 0)$ of the FM. Note that no field was applied while cooling the sample below T_N . One can thus obtain positive as well as negative loop shifts. Reproduced from [25].

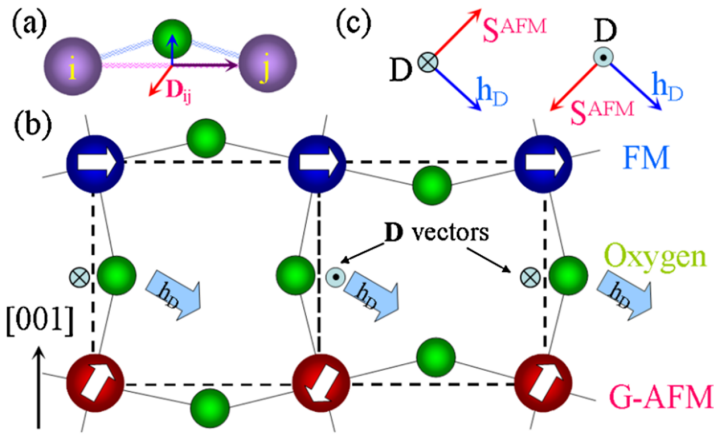


Figure 2.9: DMI interaction at a compensated FM/AFM interface, leading to a shifted hysteresis loop. Reproduced from [29].

The energy contribution due to the DMI interaction at the interface between a ferromagnet and an antiferromagnet is given by

$$E_{\text{DMI}} = \sum_i \mathbf{D}_i \cdot (\mathbf{S}_{i,\text{FM}} \times \mathbf{S}_{i,\text{AFM}}) \quad (2.14)$$

summing over only the FM/AFM spin pairs at the interface. In contrast to the Heisenberg exchange interaction, this is an antisymmetric interaction. The vector \mathbf{D}_i represents the strength of the DMI interaction and is oriented perpendicular to the plane created by the FM - oxide - AFM bond as is shown in figure 2.9. As the displacement between 2 neighbouring oxygen atoms is in an opposite direction, the vectors \mathbf{D}_i are oriented antiparallel for 2 neighbouring bonds, i.e. $\mathbf{D}_i = (-1)^i \mathbf{D}$. For antiferromagnets with a compensated plane at the interface, we also have that $\mathbf{S}_{i,\text{AFM}} = (-1)^i \mathbf{S}_{\text{AFM}}$. Using vector calculus, we can rewrite the expression for the DMI energy as

$$E_{\text{DMI}} = - \sum_i \mathbf{H}_D \cdot \mathbf{S}_{i,\text{FM}} \quad (2.15)$$

The vector $\mathbf{H}_D = \mathbf{D} \times \mathbf{S}_{\text{AFM}}$ can be seen as an effective field acting on the FM spins and points in the same direction for all FM - oxide - AFM bonds at the interface, thus giving rise to a net unidirectional effective field which leads to a shifted hysteresis loop. It is important to note that the DMI interaction (if present) is usually 2 or 3 orders smaller than the Heisenberg exchange interaction.[29]

One has also shown that ferro-electric polarisation[29] or even interfacial strain[30] between a FM and a non FM layer can induce a shift of the hysteresis loop. The former through the DMI interaction and the latter due to a change in the magnetic structure at the FM/non FM interface.

2.4 Technological applications

Although Louis Néel stated in his Nobel lecture *Magnetism and the Local Molecular Field* (1970) that antiferromagnets *are extremely interesting from the theoretical viewpoint, but do not seem to have any applications*, history has turned out to be quite different. The most well known applications of exchange bias are found in GMR or TMR spin valve sensors in the form of reading heads in hard drives and MRAM devices. We will now briefly discuss some applications of exchange bias and the interfacial coupling between a FM and an AFM in general.

2.4.1 GMR spin valve sensors

When a current flows through a conductor, conduction electrons will scatter on phonons and impurities in the lattice, resulting into a temperature dependent electrical resistance. In experiments, one has observed however that the resistivity of a conductor is increased by a small amount if it is placed inside an external magnetic field. This effect, called *ordinary magnetoresistance* (OMR), originates from the helical motion of charged particles in a magnetic field, which leads to an increased path length and thus more scattering. The corresponding resistance change (typically about 1% in a field of 1T) is positive for all metals (whether ferromagnetic or not) and is highest when the magnetic field is applied perpendicular to the current direction.

In 1856, William Thomson[31] discovered that when a ferromagnet is magnetised in an external field, its resistivity depends on the angle between the magnetisation and the current direction. He found that the resistance of Ni and Fe strips decreased when the magnetisation vector was perpendicular to the current direction and that the resistance was highest when both were parallel. This change in resistivity, called *anisotropic magnetoresistance* (AMR), hardly exceeds 5% at room temperature however and originates from the spin orbit interaction. Compared to OMR, the AMR effect is already measurable in much lower magnetic fields and is used e.g. in rotation sensors.

It took approximately another 130 years until the next big step was taken in the domain of magnetoresistive sensors by the discovery[32, 33] of the *giant magnetoresistance* (GMR) effect by Albert Fert and Peter Grünberg in 1988. Both scientists were awarded with the Nobel prize Physics in 2007 for their independent discovery of the GMR effect. When 2 ferromagnetic layers are separated by a non magnetic spacer, e.g. Cu or Cr, they can be coupled into an antiparallel orientation by making use of the RKKY interaction⁸, creating an artificial antiferromagnet in a vanishing external field. While studying the transport properties of electrons in an Fe/Cr/Fe trilayer, Grünberg[33] noticed that the resistance of this stack was lowered when both Fe layers were saturated in the same direction, thus achieving a high and low resistance state, corresponding to antiparallel (AP) and parallel (P)

⁸By varying the thickness of the non magnetic spacer, one can achieve an oscillatory coupling constant between the 2 FM layers, leading to a preferential parallel or antiparallel orientation of the 2 FM layers.

oriented Fe layers respectively. At room temperature, a resistance decrease of approximately 6% was found between the 2 states. When using $(\text{FeCr})_n$ multilayers however, Fert[32] found a resistance decrease of 50% at a temperature of 4 K. A schematic representation of the GMR effect is shown in figure 2.10.

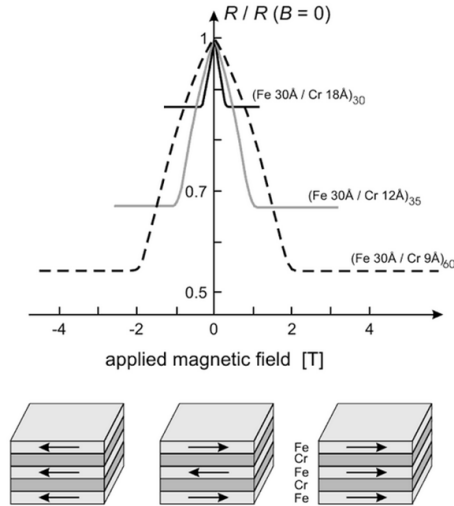


Figure 2.10: Schematic representation of the GMR effect, as was found by Fert. At vanishing field ($B = 0$ T) the FM layers are oriented antiparallel due to the RKKY interaction. The resistance R decreases while aligning both layers, leading to saturation if the Fe layers are oriented parallel. Reproduced from [34].

The GMR effect relies on the spin dependent scattering of conduction electrons and can be explained as follows. In 3d4s metals such as Fe, Co and Ni, electrons of the 4s conduction band can scatter into the exchange spin split 3d conduction band while conserving their spin orientation. As according to Fermi's golden rule, the scattering probability depends on the final density of states and as scattering happens around the Fermi level, this induces an asymmetry in resistivity between spin up and spin down electrons. The 3d band of the majority spin carriers (spin up by convention, see e.g. figure 1.5 for Co) is shifted downwards due to the exchange splitting (section 1.3.4) and thus has (in general) a lower density of states at the Fermi level compared to the minority spin carriers (spin down), which re-

sults in a lower scattering rate and thus a lower resistivity. Neglecting spin flip scattering, the total current can be considered as existing of 2 independent current channels according to the Mott model[35]: a contribution due to spin up and one due to spin down electrons. The total conductivity σ is then given by $\sigma = \sigma_{\uparrow} + \sigma_{\downarrow}$ and so for the resistance R we obtain $\frac{1}{R} = \frac{1}{R_{\uparrow}} + \frac{1}{R_{\downarrow}}$.

In case a current flows through 2 ferromagnetic layers which are magnetised antiparallel (see the experiment of Fert in figure 2.10 at $B = 0$ T), both spin polarisations will see a high resistance path, leading to an in total high resistance. When the FM layers are oriented parallel however, there will be spins with a high resistance and spins with a low resistance, leading to an in total low resistance. By changing the direction of the magnetisation of one FM layer, parallel or antiparallel with respect to the other FM layer, one can thus create 2 states: low and high resistance respectively. The strength of the GMR effect is usually characterized by $\frac{\Delta R}{R_P} = \frac{R_{AP} - R_P}{R_P}$ with R_{AP} the measured resistance when the ferromagnetic layers are antiparallel and R_P the resistance when the FM layers are parallel.

Due to the strong coupling between the FM layers, a high magnetic field is needed to saturate both layers in the same direction. This appeared to be a major drawback, even though GMR sensors had a remarkable higher magnetoresistive ratio compared to AMR sensors. Searching for alternatives, but still eager to use this GMR effect, one soon invented the (probably) most famous application of giant magnetoresistance: the GMR spin valve sensor. A spin valve (figure 2.11, left) consists of 2 ferromagnetic layers, separated by a thin non magnetic metallic spacer. In contrast to the trilayer and multilayered stacks as were designed by Grünberg and Fert, the spacer is made thick enough to decouple the 2 FM layers. One of the ferromagnetic layers is pinned due to the exchange bias interaction with an antiferromagnetic layer and is thus set as a reference direction. As the free ferromagnetic layer can easily be switched through the application of an external field, one can create a high and low resistance regime. GMR spin valve sensors were commercialized very fast and started to replace the AMR sensors in magnetic reading heads already around 1994 - 1995.

In a GMR spin valve reading head, 2 geometries are possible (figure 2.12), depending on the position of the metallic contacts, guiding the current. When the contacts are placed on one layer only (CIP configuration), the

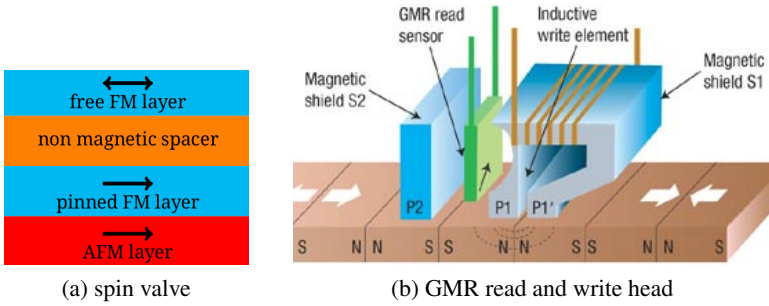


Figure 2.11: Left: Schematical drawing of a spin valve. Right: The use of a GMR spin valve reading head (reproduced from [36]) in hard disk drives.

current flows parallel to the FM/AFM interface. When the FM layers and the metallic spacer are thin, the electrons will travel through both layers. It is clear that in this case the mean free path of the electrons is important as otherwise only one layer would be sampled and thus the effect would disappear. In the second configuration (CPP), the current flows perpendicular to the FM/AFM interface. In reading heads the orientation of the pinned layer is chosen perpendicular to the free layer when no magnetic field is present. When the head passes over a stray field produced by 2 antiparallel domains, the free layer deflects a bit up or down due to the interaction with this stray field, leading to a difference in resistance and thus a (positive or negative) voltage signal if one keeps the current constant. This sequence of voltage signals and the absence of voltage signals can be converted into 1's and 0's. As ferromagnetic material, one typically uses CoFe or NiFe and as antiferromagnet FeMn or IrMn.

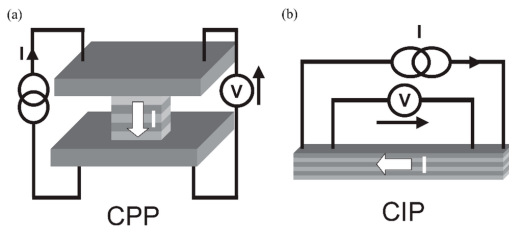


Figure 2.12: In GMR spin valve reading heads 2 geometries are possible. Left: CPP in which the current flows perpendicular to the FM/AFM interface and CIP in which the current flows parallel to the FM/AFM interface.

2.4.2 TMR spin valve sensors

Some years before the discovery of the GMR effect by Fert and Grünberg, another magnetoresistive effect was reported by Jullière[37] in 1975, called tunneling magnetoresistance (TMR). In this case, the metallic spacer in the spin valve (figure 2.11, left) is replaced by a thin insulating layer (e.g. MgO or Al₂O₃) and the stack behaves as a magnetic tunnel junction (MTJ). One can calculate[38] that the conductance $G = \frac{dI}{dV}$, associated with the tunneling of an electron between 2 metals is proportional to $D_1(E_F)D_2(E_F)$ for small bias voltages, with D_1 and D_2 the density of states of the 2 metals. Assuming no spin flip during tunneling, we can consider the current as existing of 2 independent spin channels again and so the total conductance is given by $G_{\text{tot}} = G_{\uparrow} + G_{\downarrow}$. In case the magnetisations of 2 identical FM layers (with exchange split energy bands) in the MTJ are parallel, we find that $G_P \propto D_{\uparrow}^2(E_F) + D_{\downarrow}^2(E_F)$ and when the layers are antiparallel we find that $G_{AP} \propto 2D_{\uparrow}(E_F)D_{\downarrow}(E_F)$ as then the majority spin carriers become minority spin carriers and vice versa. As was the case in the GMR effect, the difference in conductance (and thus also in resistance) between 2 parallel or antiparallel oriented FM layers results from the exchange splitting of the energy bands. The pinning of one FM layer is achieved by coupling it to an AFM layer, similar to the GMR spin valve.

As Jullière measured a TMR ratio of only 14% in an Fe/GeO/Co stack at 4 K and no effect was found at room temperature, little attention was given to this discovery in contrast to the GMR effect. In 1995 however, TMR ratio's of up to 15% were found at room temperature by Miyazaki and Moodera, which led to a regained interest in magnetic tunnel junctions. A record value[39] of TMR = 1010% was obtained in a CoFeB/MgO/CoFeB stack at a temperature of 5K and a TMR ratio of 500% at room temperature. In 2004, TMR reading heads were commercialized by Seagate. TMR sensors have many advantages such as a higher magnetoresistive ratio, a higher output voltage and a lower temperature dependence compared to AMR and GMR spin valve sensors.

A nice historical overview of magnetoresistive effects, corresponding typical MR ratio's and applications is shown in figure 2.13. Except from the AMR reading head, each of the mentioned technologies uses exchange bias to pin the ferromagnetic reference layer.

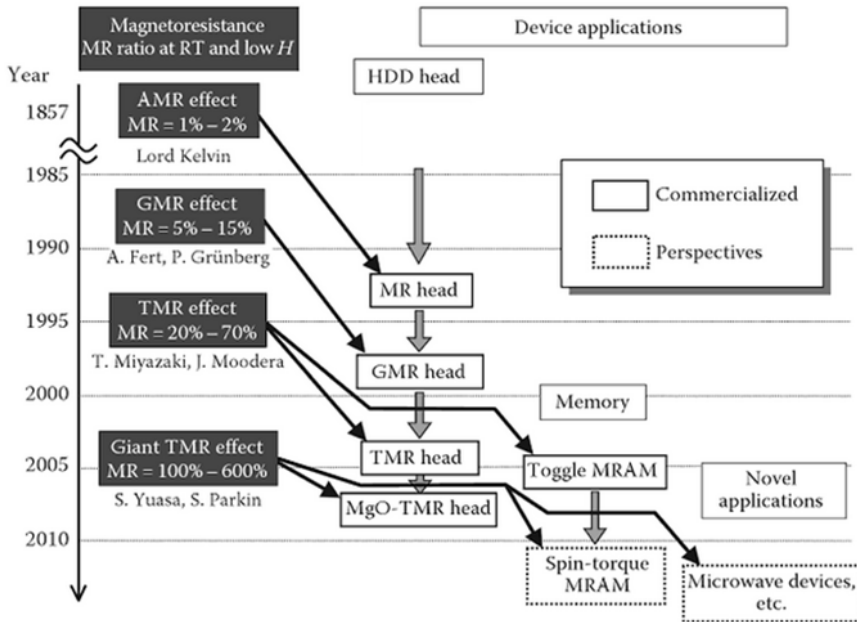


Figure 2.13: Overview (2011) of magnetoresistive effects and their applications. Reproduced from [40].

2.4.3 MRAM devices

GMR or TMR spin valves can not only be used as magnetic sensors or to read data, but also to store data as is done in magnetoresistive random access memory (MRAM) devices. A schematic example of such a MRAM device, existing of many individual MRAM cells in a typical crosspoint architecture, is shown in figure 2.14. By probing the resistance of the MTJ, one can determine if the memory element is in a 1 or 0 state.

To be able to locally switch only 1 MRAM cell without affecting neighbouring cells and thus to enhance the stability of a MRAM device, the free FM layer is often replaced by a synthetic AFM whose easy axis makes an angle of 45° with respect to the bit and word lines (figure 2.14). Switching is done by applying a specific current sequence to the desired bit and word line, creating a combination of 2 perpendicular magnetic fields on the MRAM cell. This mechanism is called toggle MRAM.

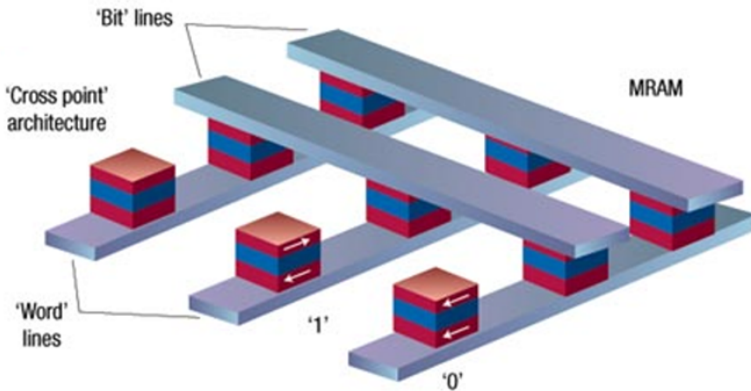


Figure 2.14: Drawing of a MRAM device, consisting of many individual TMR spin valves. Reproduced from [41].

Another and today more promising way to switch the free FM layer is by using spin transfer torque[42, 43]. This effect can be explained by considering a spin valve. An unpolarised current will become spin-polarised when flowing through the pinned FM layer due to the spin dependent scattering at the interface. When this current then passes through the free FM layer, these polarised electrons will try to align their spin parallel to the magnetisation of the free layer. This change in spin orientation leads to a net transfer of angular momentum of the current towards the free layer due to the conservation of angular momentum and thus leads to a torque on the magnetisation of the free layer. If the current is high enough, typically of the order 10^7 A/cm², it can lead to the switching of the magnetisation of the free FM layer in a direction parallel to the (almost) fixed layer. By applying a current in the reverse direction, thus from the free layer to the fixed layer, one can pull the magnetisation of the free layer away from the fixed layer. The reason is that the fixed layer mostly reflects electrons with a polarisation that is not parallel to its magnetisation as the fixed layer cannot absorb this angular momentum and thus these electrons will once again move back through the free layer, applying a torque on the free layer and trying to switch the free layer in a direction antiparallel to the fixed layer.

The advantages of MRAM devices are that they do not lose data when the power is cut off (non-volatile) as the data is not stored by means of an electric charge. Furthermore, they use less power and have a fast access time

on the order of several ns. Investigations on this new technology are still in full progress however. In 2016, a paper[44] was published by IBM and Samsung in which they report to have made an 11 nm sized spin transfer torque MRAM chip, switching data in 10 ns with a write current of $7.5 \mu\text{A}$. The commercialization of MRAM chips is expected to explode in the next few years. Since 2008, the company EverSpin has sold already more than 60 million MRAM chips.

2.4.4 HDD technology

On a hard disk, bits are written by the formation of magnetic domains in a FM layer through the application of an external field induced by the writing head, as can be seen in figure 2.11. In order to downsize these magnetic domains and thus increase storage density, extra stabilisation of these domains is required in order to compensate for the energy penalty, associated with the formation of domain walls in the FM. This can be done e.g. by coupling the FM layer to an antiferromagnet. To achieve this extra stabilisation of the FM domains however, one would need to be able to locally switch the direction of the bias field together with the underlying FM domain.

Albisetti et al.[45] have shown that, after cooling an IrMn/CoFeB bilayer in a uniform external field H_{fc} below the Néel temperature, one can locally switch the frozen AFM grains (and thus the exchange bias direction) by locally heating (while cooling the whole sample under T_N) with a hot atomic force microscopy tip in contact mode and applying an external field H_{ext} opposite to the field cooling direction. After removal of the hot tip and the external field, the FM domains were oriented antiparallel to the original field cooling direction H_{fc} . The principle is shown in figure 2.15.

In this way, one can write magnetic domains of arbitrary shape in the ferromagnetic layer. One can erase these domains by again locally heating above the Néel temperature and applying an external field in the direction of the original bias field H_{fc} . The stability of these domains is guaranteed by the local bias field and its resolution is determined by the spread of the thermal field due to the hot tip. Although they wrote FM domain structures on the order of 1 to $2 \mu\text{m}$, one has shown[46] that a thermal resolution of approximately 20 nm could be obtained in a graphene oxide film by using an atomic force microscopy tip.

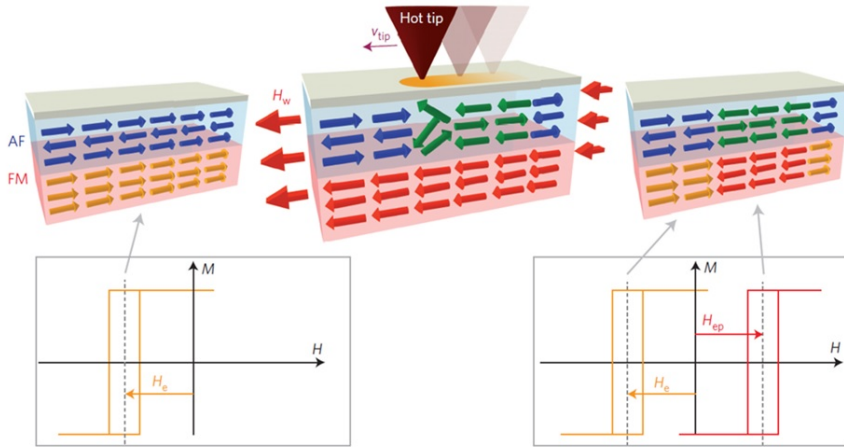


Figure 2.15: Schematic representation of the local switching of the bias field direction. Top left: Field cooled case. Top middle: By locally heating the AFM with a hot SPM tip and meanwhile applying an external field, one can locally switch the direction of the bias field (top right). Reproduced from [45].

Apart from providing extra stabilisation of magnetic domains in a thin film, exchange bias can also provide a way to beat the superparamagnetic limit[47]. For very small magnetic nanostructures or nanoparticles, the thermal energy $E_{\text{th}} = k_B T$ can become comparable to the uniaxial anisotropy energy $E_{\text{anis}} = K_{\text{FM}} V$ with V the volume of the particle or to the shape anisotropy. In this case, the particle becomes superparamagnetic and thus flips randomly due to thermal fluctuations in the absence of an external field. Stabilisation can be achieved by choosing FM materials with a high anisotropy, e.g. CoPt or FePt for which K_{U} is of the order $1 \times 10^6 \text{ J/m}^3$. Another way to beat the superparamagnetic limit would be by coating the FM nanoparticle with an antiferromagnet, as exchange bias dictates an extra preferential direction and thus has the potential to increase stability. Furthermore, this interface coupling leads to an enhanced coercivity. It has been shown[48] that by coupling a CoPt multilayer to IrMn, the out-of-plane anisotropy can be stabilized up to higher temperatures. Whereas the remanence of the uncoupled CoPt layer disappeared around $T = 375 \text{ K}$, it only vanished around 400 K for the exchange biased CoPt/IrMn layer.

2.4.5 Compensated antiferromagnetic interfaces

Also compensated antiferromagnetic interfaces can have some interesting technological applications. As we will discuss later (chapter 4), the coupling of such an interface with a ferromagnet induces an enhanced coercivity, perpendicular to the Néel axis of the antiferromagnet and thus leads to a uniaxial contribution instead of a unidirectional anisotropy as in the case of exchange bias. This perpendicular spin flop coupling can stabilize magnetic domain structures in ferromagnets, which are otherwise not stable[49] or can also lead to lower switching fields in nanomagnets[50] when the induced easy axis is perpendicular to the applied field.

2.5 Modelling of antiferromagnets

When investigating complex phenomena, such as exchange bias, one usually first resorts to simple theoretical models as these can give some indications about the dependence of these phenomena on the physical parameters. One often uses the macrospin approach as a first step. In this approximation, one assumes that each magnetic subsystem (e.g. the FM or an AFM sublattice) is in a uniform state and so can be replaced by a single vector. A magnetic system can then be fully characterised by defining the relevant angles and the stability positions can be found by minimizing the total energy of the system, analogous to what was done in the Stoner Wohlfarth model (section 1.6). Although the macrospin model can capture the essential physics of a magnetic system in most cases, is easy to implement and one can calculate hysteresis loops, it is not a very realistic approach when dealing with polycrystalline antiferromagnets as e.g. no training effects can be taken into account. Also systems containing magnetic vortices or systems in which the magnetostatic coupling between multiple nanostructures plays an important role, cannot or can hardly be described in these models due to the complex nature of the demagnetisation energy.

To avoid these limitations and to improve the understanding of antiferromagnets in general, numerical software packages were developed (e.g. Vampire[51]) in which one models the antiferromagnet at the discrete atomic level. Due to the smallness of the lattice constant however, these calcula-

tions require a lot of computing time as many lattice points (atoms) are needed to be taken into account and so only smaller magnetic structures (typically of the order 100 nm) can be studied within reasonable efforts and without making use of supercomputers.

In order to investigate static effects due to the interface coupling between a FM and an AFM, it is not necessary however to model an AFM on the atomic scale as in most cases the high frequency dynamics are not important. So a micromagnetic approach can be a very valuable tool and provide a golden mean between simple analytical models and a full atomistic description of an antiferromagnet. One often uses custom, in-house developed modelling codes which are not freely accessible to the scientific community and can only be used for specific cases. Although also some open source micromagnetic solvers, e.g. OOMMF[52] and Nmag[53] are available, these do not explain how one can take into account the interface interaction between a ferromagnet and an antiferromagnet.

In this thesis, we will study how the framework of MuMax3[12], a free open source micromagnetic simulation program, can be used to model compensated and uncompensated AFM interfaces and demonstrate that we can take into account phenomena such as exchange bias, spin flop coupling and athermal training by using an effective micromagnetic approach. We will show that these effects can easily be implemented in MuMax³ without making any changes to the internal code. The advantages are that one can simulate micrometer sized magnetic structures, take into account the magnetostatic energy of the ferromagnet which is often neglected in analytical models and apply thermal fluctuations. The bias field will be implemented as a real exchange coupling between the FM and the AFM, rather than just being replaced by an effective external field, present in the ferromagnet. One can model the microstructure of an antiferromagnet (or ferromagnet) by dividing it into several grains[54]. This allows the user to locally vary coupling constants, direction of anisotropy axes, anisotropy constants, etc.

Another big advantage of using MuMax³, compared to other micromagnetic solvers, is its high computing performance by making use of GPU's to speed up the calculation of the magnetostatic field, which requires the most computing time. Figure 2.16 shows the performance of MuMax³ compared to OOMMF (CPU) and when using different NVIDIA GPU's.

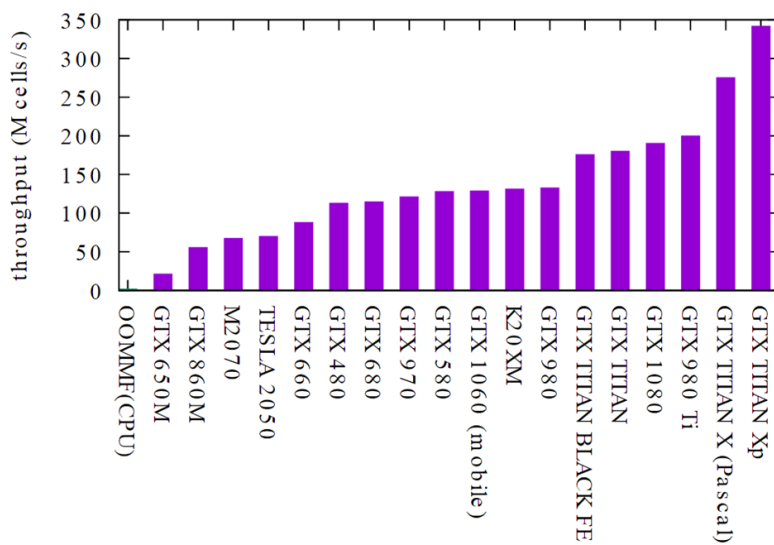


Figure 2.16: GPU performance of MuMax³ for a 2D simulation containing approximately 4 million cells. The image shows how many cells can have their torque evaluated per second. Taken from <http://mumax.github.io/>

MODELLING UNCOMPENSATED AFM INTERFACES IN MUMAX³

Paper I*Modelling exchange bias with MuMax³[1]**Interface structure: a hard nut to crack*

Miguel Kiwi, [55]

3.1 Introduction

As is very common in physics, a more systematic investigation of the exchange bias phenomenon, showed that the rigid model of Meiklejohn and Bean, as defined in section 2.2, was too simplistic. One of the reasons, leading to a refinement of this theory was that the bias field, estimated by using the exchange integral for the interaction between a Co and CoO atom, is an order or even two orders too high compared to the experimental data.[20, 56] For a Co(40nm)/CoO(2.5nm) bilayer, one typically finds that $B_{\text{eb}} \approx 20$ mT. Using equation 2.9, we obtain that the *average* coupling constant J_{I} is given by $J_{\text{I}} \approx 1.1$ mJ/m².

A first estimate for the theoretical value of J_{I} for CoO can be found as follows. As CoO has a NaCl crystal structure[57], we can see that the (111) surface is an uncompensated interface and only contains Co atoms. The grey triangle in figure 2.3 effectively contains $n = 3 \times \frac{1}{6} + 3 \times \frac{1}{2} = 2$ Co²⁺ atoms. Labeling the lattice constant of CoO as $a = 4.27 \times 10^{-10}$ m, the area of this grey surface is given by $A = \frac{\sqrt{3}a^2}{2}$ and thus one can estimate that the coupling constant J_{I} is given by $\frac{nJ_{\text{AFM}}}{A} \approx 4$ mJ/m² where $J_{\text{AFM}} = 2$ meV

is the absolute value of the exchange integral[58] of the antiferromagnetic CoO. This result is approximately a factor 4 higher than one typically finds from experiments and leads to the conclusion that maybe not all uncompensated spins contribute to exchange bias, maybe some AFM spins are compensated or other effects have to be taken into account. If one would use J_{FM} instead of J_{AFM} , the discrepancy would be even higher.

Another piece of the puzzle was found by noticing that exchange bias is often accompanied by an enhanced coercivity. As the FM/AFM interface is often not perfect due to impurities or defects, one can expect that a transition region is present at the interface with a lowered coercivity. AFM spins with a bulk anisotropy constant will stay pinned during a reversal of the FM and lead to exchange bias, while spins with a lowered anisotropy constant can, depending on the strength of the interface coupling J_{I} , possibly rotate together with the FM and thus lead to an enhanced coercivity. This mechanism of rotatable and pinned AFM spins is supported by training effects which are present in most polycrystalline FM/AFM bilayers. One has noticed that the bias field B_{eb} and the coercivity B_{c} decrease for an increasing number of hysteresis cycles n . This training effect can be split into 2 contributions: thermal and athermal training.

Athermal training predominantly happens in the first hysteresis loop and originates from the fact that AFM spins can be in a frustrated state after field cooling or due to a small coupling between the AFM grains.[59] The size of this effect thus depends on the initial state of the AFM. Often this also leads to an asymmetric hysteresis loop for $n = 1$, which is a typical signature of athermal training.

Thermal training results from thermal fluctuations which depin frozen AFM spins during the hysteresis loop and is present for $n \geq 1$. In general, this effect is smaller than athermal training. Experiments[60, 61, 62] as well as theoretical considerations[63] have shown that the evolution of the bias field B_{eb} as a function of the number of hysteresis cycles n is given by

$$B_{\text{eb}}(n) = B_{\text{eb}}^{\infty} + \frac{\kappa}{\sqrt{n}} \quad (3.1)$$

where B_{eb}^{∞} is the bias field after a large number of hysteresis cycles and κ a temperature dependent constant, specific for each system. The difference between thermal and athermal training can clearly be seen in figure 3.1.

In the rigid Meiklejohn and Bean model (section 2.2), one assumes that the AFM has an infinite anisotropy. Clearly, such a theory cannot take into account rotatable AFM spins and thus cannot produce any training effects or explain the enhanced coercivity of the loop after field cooling. Although the model of Mauri could explain the discrepancy between the magnitude of the theoretical and the experimental bias field (equation 3.12) by the introduction of a planar domain wall in the antiferromagnet, it could not provide any answers about the origin of the enhanced coercivity.

In this chapter, we will first discuss a more advanced model, which includes rotatable AFM spins and was first proposed by Radu[20]. We will implement this model in MuMax³ and demonstrate that we can reproduce experimental data[60] of an exchange biased Co/CoO bilayer. Finally, also the origin of positive exchange bias will be discussed.

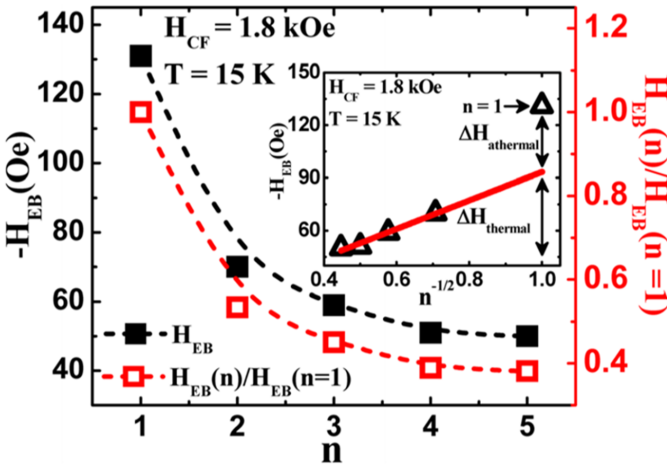


Figure 3.1: Athermal ($n = 1$) and thermal training ($n \geq 1$) for an IrMn(15nm)/CoFe(10nm) bilayer. The athermal component does not satisfy the power law (see inset) as given in equation 3.1 as it results from frustration in the AFM after field cooling. Reproduced from [64].

3.2 Exact solution for uncompensated AFM spins

Following the model of Radu[20], the total surface energy of an infinite, thin FM layer coupled to an uncompensated AFM can be written as

$$\begin{aligned} \sigma(\beta, \phi) = & -\mu_0 H_{\text{ext}} M_{\text{FM}} t_{\text{FM}} \cos(\gamma - \beta) - J_{\text{I}} \cos(\beta - \phi) \\ & - K_{\text{AFM}} t_{\text{AFM}} \cos^2(\phi) - J_{\text{A}} \cos(\phi) \end{aligned} \quad (3.2)$$

The first term is the Zeeman energy of the FM, the second term is the interfacial coupling between the FM and the AFM layer, the third term is the uniaxial anisotropy energy of the AFM layer and the last term represents the energy to form a planar domain wall in the AFM, as was discussed in the model of Mauri¹, section 2.3.1. The definitions of the angles γ , β and ϕ are shown in figure 3.2. The difference with the rigid model of Meiklejohn and Bean (equation 2.7) is that this more advanced model allows for a rotation of the AFM macrospin with respect to its anisotropy axis.

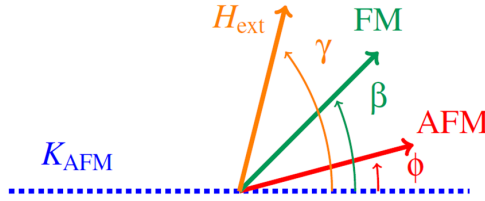


Figure 3.2: The angles γ , β and ϕ are defined with respect to the uniaxial axis (blue line) of the uncompensated antiferromagnetic macrospin.

Analogous to what was discussed in the Stoner Wohlfarth model and the Mauri model, the energy extrema can be found by simultaneously solving the equations $\frac{\partial \sigma}{\partial \beta} = 0$ and $\frac{\partial \sigma}{\partial \phi} = 0$. The angles β^* and ϕ^* , which extremise the total energy of the system, are determined by

$$\begin{aligned} \frac{\partial \sigma}{\partial \beta} &= -\mu_0 H_{\text{ext}} M_{\text{FM}} t_{\text{FM}} \sin(\gamma - \beta^*) + J_{\text{I}} \sin(\beta^* - \phi^*) = 0 \\ \frac{\partial \sigma}{\partial \phi} &= -J_{\text{I}} \sin(\beta^* - \phi^*) + t_{\text{AFM}} K_{\text{AFM}} \sin(2\phi^*) + J_{\text{A}} \sin(\phi^*) = 0 \end{aligned}$$

¹A constant energy shift has no influence on the position or the stability of the extrema.

For reasons of simplicity we will assume that the parameters J_I , J_A and K_{AFM} are positive and $\gamma = 0$, i.e. the external field is applied parallel to the anisotropy axis of the antiferromagnet.

Case 1: $K_{\text{AFM}} \neq 0$, $J_A = 0$

We will first discuss the case in which no domain wall is formed in the antiferromagnet, i.e. $J_A = 0$. For low coupling constants J_I , we can expect that the AFM layer will not switch together with the FM and so the reversal of the FM will happen through a continuous rotation of the FM magnetisation vector as a unidirectional anisotropy will be induced by the AFM. This spring type of behaviour does not lead to a coercivity and so the bias field B_{cb} can be derived² from $\beta^* = \frac{\pi}{2}$, i.e. the FM is perpendicular to the applied external field.[65] Two different sets of solutions (equations 3.3 and equations 3.4) can be found

$$\cos(\phi^*) = -\frac{\mu_0 H_{\text{cb}} M_{\text{FM}} t_{\text{FM}}}{J_I} \quad \text{and also} \quad \cos(\phi^*) = 0 \quad (3.3)$$

$$\cos(\phi^*) = -\frac{\mu_0 H_{\text{cb}} M_{\text{FM}} t_{\text{FM}}}{J_I} \quad \text{and also} \quad \sin(\phi^*) = \frac{J_I}{2K_{\text{AFM}} t_{\text{AFM}}} \quad (3.4)$$

To determine when these solutions are energy minima, one should demand

$$\frac{\partial^2 \sigma}{\partial \beta^2} = J_I \sin(\phi^*) > 0 \quad (3.5)$$

$$\frac{\partial^2 \sigma}{\partial \phi^2} = 2K_{\text{AFM}} t_{\text{AFM}} \cos(2\phi^*) + J_I \sin(\phi^*) > 0 \quad (3.6)$$

$$\text{Hess}(\theta, \phi) = \left(\frac{\partial^2 \sigma}{\partial \beta^2} \right) \left(\frac{\partial^2 \sigma}{\partial \phi^2} \right) - \left(\frac{\partial^2 \sigma}{\partial \phi \partial \beta} \right)^2 > 0 \quad (3.7)$$

$$= 2K_{\text{AFM}} t_{\text{AFM}} J_I \cos(2\phi^*) \sin(\phi^*) > 0 \quad (3.8)$$

²Due to the reversible behaviour, the hysteresis loop has a vanishing coercivity. Although $\beta^* = 0$ and $\beta^* = \pi$ are stable solutions in the case $\phi^* = 0$ for $J_I < K_{\text{AFM}} t_{\text{AFM}}$, they can only be used to define an average shift of the hysteresis loop by defining $B_{\text{shift}} = \left| \frac{B_{\text{ext}}(\beta^* = \pi) + B_{\text{ext}}(\beta^* = 0)}{2} \right|$ where $B_{\text{ext}}(\beta^* = \pi)$ and $B_{\text{ext}}(\beta^* = 0)$ are the external fields at which the solutions $\beta^* = \pi$ and $\beta^* = 0$ lose stability, respectively. Due to the asymmetry of the hysteresis loop, this does not coincide however with the definition $B_{\text{cb}} = B_{\text{ext}}(\langle m \rangle = 0)$ which one uses to define the bias field in case of a vanishing coercivity. This is shown in Appendix B. The asymmetry of the hysteresis loop complicates the discussion, together with the fact that $\beta^* = \frac{\pi}{2}$ can be stable, even for a vanishing bias field. For a full analysis one should resort to numerical simulations, as will be discussed in section 3.5.

For the solution $\phi^* = \pm \frac{\pi}{2}$, as determined by the set 3.3, the third condition is not satisfied as this leads to a saddle point and a vanishing bias field³. The other set of solutions (equations 3.4) are only consistent with each other and determine that $\beta^* = \frac{\pi}{2}$ is an extremum when the external field at that moment given by

$$\mu_0 |H_{c,b}| = \frac{J_1}{M_{\text{FM}} t_{\text{FM}}} \sqrt{1 - \left(\frac{J_1}{2K_{\text{AFM}} t_{\text{AFM}}} \right)^2} \quad (3.9)$$

Demanding that $\beta^* = \frac{\pi}{2}$ is an energy minimum does not necessarily lead to exchange bias, but can also lead to coercive fields with this magnitude. As will be discussed later, numerical analysis shows that the bias field vanishes for $J_1 \geq K_{\text{AFM}} t_{\text{AFM}}$ and that the solution $\beta^* = \frac{\pi}{2}$ is stable as long as $J_1 \leq 2K_{\text{AFM}} t_{\text{AFM}}$. This leads to the conclusion that equation 3.9 represents the absolute value of the bias field for $J_1 \leq K_{\text{AFM}} t_{\text{AFM}}$ and thus $B_{\text{eb}} = -\mu_0 |H_{c,b}|$ with $B_{\text{c}} = 0$. In case $K_{\text{AFM}} t_{\text{AFM}} \leq J_1 \leq 2K_{\text{AFM}} t_{\text{AFM}}$, the bias field is turned into coercivity, i.e. $B_{\text{c}} = \mu_0 |H_{c,b}|$ with $B_{\text{eb}} = 0$. So we find that AFM spins with $J_1 \leq K_{\text{AFM}} t_{\text{AFM}}$ are pinned and lead to exchange bias while AFM spins with $J_1 \geq K_{\text{AFM}} t_{\text{AFM}}$ rotate together with the ferromagnet and lead to an enhanced coercivity.

For a very strong anisotropy, so $K_{\text{AFM}} \rightarrow \infty$, one recovers the bias field as was found by Meiklejohn and Bean (equation 2.9), i.e. $B_{\text{eb}} = -\frac{J_1}{M_{\text{FM}} t_{\text{FM}}}$. For CoO one typically finds that the average value of J_1 is of the order 0.1 to 1 mJ/m², approximately a factor 10 lower than the theoretical predicted value. This leads to the conclusion that in polycrystalline antiferromagnets only a few percent of the spins are pinned.

Another important result is that this equation shows an explicit dependence of the bias field on the thickness of the antiferromagnet⁴, which is not present in the model of Meiklejohn and Bean. The advanced model, as defined in equation 3.2, also predicts that there exists a critical thickness $t_{\text{AFM,c}} \leq \frac{J_1}{K_{\text{AFM}}}$ under which no exchange bias is present. In this case, the

³The solution $\phi^* = \pm \frac{\pi}{2}$ is the limiting case of the set 3.4 as $|\sin(\phi^*)| \leq 1$ and $\beta^* = \frac{\pi}{2}$ is not a solution anymore for $J_1 \geq 2K_{\text{AFM}} t_{\text{AFM}}$.

⁴Experiments show that the relation between the bias field and the AFM thickness is often much more complicated. The $\frac{1}{t_{\text{F}}}$ law is applied to all models describing exchange bias and has been verified in experiments, unless in the case of very thin and very thick FM layers.

AFM spins rotate together with the FM layer and thus lead to an enhanced coercivity, but not to a bias field. For a Ni₈₀Fe₂₀(6.5nm)/IrMn bilayer[66], one finds that the critical thickness is around $t_{\text{AFM,c}} = 3$ nm. In realistic FM/AFM systems one can expect that rotatable as well as pinned uncompensated AFM spins are present.

Case 2: $K_{\text{AFM}} = 0, J_{\text{A}} \neq 0$

This case reduces to the model of Mauri, introduced in section 2.3.1. As the AFM macrospin is set to rotate against a unidirectional axis and no uniaxial anisotropy energy terms are present in the total surface energy, the ferromagnet will always reverse through continuous coherent rotation. For $\beta^* = \frac{\pi}{2}$, the equilibria are determined by

$$\cos(\phi^*) = -\frac{\mu_0 H_{\text{eb}} M_{\text{FM}} t_{\text{FM}}}{J_{\text{I}}} \quad \text{and also} \quad J_{\text{I}} \cos(\phi^*) = J_{\text{A}} \sin(\phi^*)$$

Using $\cos^2(\phi^*) + \sin^2(\phi^*) = 1$, one finds that the bias field B_{eb} is given by

$$B_{\text{eb}} = -\frac{J_{\text{I}} J_{\text{A}}}{M_{\text{FM}} t_{\text{FM}} \sqrt{J_{\text{I}}^2 + J_{\text{A}}^2}} \quad (3.10)$$

Assuming the weak coupling limit $J_{\text{I}} \ll J_{\text{A}}$, we find that

$$B_{\text{eb}} \approx -\frac{J_{\text{I}}}{M_{\text{FM}} t_{\text{FM}}} \quad (3.11)$$

which amounts to the maximal attainable exchange bias field (equation 2.9).

In case of strong coupling between the ferromagnet and the antiferromagnet and so $J_{\text{I}} \gg J_{\text{A}}$, the bias field is determined by

$$|B_{\text{eb}}| \approx \frac{2\sqrt{A_{\text{AFM}} K_{\text{AFM}}}}{M_{\text{FM}} t_{\text{FM}}} \ll \frac{J_{\text{I}}}{M_{\text{FM}} t_{\text{FM}}} \quad (3.12)$$

This shows that in this case the value of the bias field is reduced compared to the rigid Meiklejohn and Bean model, as the energy is spread over the length of the AF domain wall, which is of the order $\sqrt{\frac{A_{\text{AFM}}}{K_{\text{AFM}}}}$. By evaluating the second order derivatives of the total surface energy, one can discriminate between two regions in this model[20]. In case $J_{\text{I}} < 2\sqrt{A_{\text{AFM}} K_{\text{AFM}}}$, the twist in the antiferromagnet becomes unstable at a certain critical angle⁵ ϕ_{c} and the AFM macrospin returns to $\phi = 0$ as $\beta \rightarrow \pi$, comparable to

⁵In the limiting case that $J_{\text{I}} = 2\sqrt{A_{\text{AFM}} K_{\text{AFM}}}$, the critical angle is given by $\phi_{\text{c}} = \frac{\pi}{2}$.

pinned AFM spins. If $J_I > 2\sqrt{A_{\text{AFM}}K_{\text{AFM}}}$, the antiferromagnetic domain wall will rotate (approximately) together with the ferromagnetic layer towards $\beta \rightarrow \pi$, analogous to a rotatable AFM spin but without introducing any coercivity. It is important to note that we assumed the AFM layer has an infinite thickness and so AFM spins, far way from the interface, are pinned. For a thin AFM, the twist angle ϕ can become unstable at a certain critical value, leading to a 180° switching of the AFM sublattices, which is in fact nothing else than a rotatable AFM spin.

As antiferromagnetic ordering happens under the Néel temperature, one would also expect the exchange bias field B_{eb} to disappear at $T = T_N$. Experiments[67] have shown however that for thin antiferromagnets, which usually exist of small AFM grains rather than being a perfect uniform layer as was assumed in the macrospin approach of Meiklejohn and Bean, the bias field vanishes at a lower temperature, called the blocking temperature $T_B < T_N$. Using numerical calculations[68], Wee has shown that thermal fluctuations can lead to a depinning of partial domain walls and thus a vanishing bias field. This does not mean however that the AFM is decoupled from the FM as an enhanced coercivity is still observed up to $T \approx T_N$ [69]. In case of thick antiferromagnets, one usually observes that $T_B \approx T_N$.

Case 3: $K_{\text{AFM}} \neq 0, J_A \neq 0$

These cases have to be solved numerically.

3.3 Approximated solution for uncompensated AFM spins

In a mathematical system with multiple variables, it is not always possible to find an analytical solution and so one often has to approximate the exact equations. For high anisotropy constants K_{AFM} and low coupling constants J_I , one can assume that the canting angle ϕ , which the antiferromagnet makes with its easy axis, is rather small. In this case, one can approximate the trigonometric formula's using a Taylor expansion. For small canting angles ϕ , we can write that

$$\begin{aligned} \cos(\beta - \phi) &\approx \cos(\beta) \left(1 - \frac{\phi^2}{2}\right) + \phi \sin(\beta) \\ \cos^2(\phi) &\approx 1 - \phi^2 \end{aligned}$$

retaining only second order in ϕ . The total surface energy density can be approximated by

$$\begin{aligned} \sigma(\beta, \phi) \approx & -\mu_0 H_{\text{ext}} M_{\text{FM}} t_{\text{FM}} \cos(\beta) - J_{\text{I}} \cos(\beta) \left(1 - \frac{\phi^2}{2}\right) \\ & - J_{\text{I}} \phi \sin(\beta) + K_{\text{AFM}} t_{\text{AFM}} \phi^2 \end{aligned} \quad (3.13)$$

with $\gamma = 0$, $J_{\text{A}} = 0$ and dropping constant energy terms. Minimizing this energy towards the angle ϕ , we find

$$\frac{\partial \sigma}{\partial \phi} = J_{\text{I}} \phi^* \cos(\beta) - J_{\text{I}} \sin(\beta) + 2K_{\text{AFM}} t_{\text{AFM}} \phi^* = 0 \quad (3.14)$$

Solving this system for ϕ^* , we obtain

$$\phi^*(\beta) = \frac{J_{\text{I}} \sin(\beta)}{J_{\text{I}} \cos(\beta) + 2K_{\text{AFM}} t_{\text{AFM}}} \quad (3.15)$$

Assuming that the AFM is always in the energy minimum, we can use this solution ϕ^* to construct an *effective* surface energy density $\sigma_{\text{eff}}(\beta, \phi^*(\beta))$ which depends only on the FM angle β

$$\begin{aligned} \sigma_{\text{eff}}(\beta) \approx & -\mu_0 H_{\text{ext}} M_{\text{FM}} t_{\text{FM}} \cos(\beta) - J_{\text{I}} \cos(\beta) \\ & - \frac{J_{\text{I}}^2 \sin^2(\beta)}{2[J_{\text{I}} \cos(\beta) + 2K_{\text{AFM}} t_{\text{AFM}}]} \end{aligned} \quad (3.16)$$

Minimizing this effective surface energy density towards β , assuming continuous rotation⁶ so that $\beta^* = \frac{\pi}{2}$ is a stable solution, we find that the bias field is given by

$$B_{\text{eb}} \approx -\frac{J_{\text{I}}}{M_{\text{FM}} t_{\text{FM}}} \left(1 - \frac{J_{\text{I}}^2}{8K_{\text{AFM}}^2 t_{\text{AFM}}^2}\right) \quad (3.17)$$

which is the first order approximation of the exact solution as given in equation 3.9 and shows the consistency of this method. The second term in equation 3.16 corresponds to the model of Meiklejohn and Bean with an infinite anisotropy K_{AFM} whereas the third term will allow a small canting of the uncompensated AFM spin and thus leads to a small reduction of the maximal bias field $B_{\text{eb,max}} = -\frac{J_{\text{I}}}{M_{\text{FM}} t_{\text{FM}}}$. A similar approach will be used in chapter 4 when discussing the influence of a compensated AFM interface on a ferromagnet.

⁶This is in accordance with the assumption that ϕ is small

As we have assumed small canting angles and assumed this state is the global energy minimum⁷ for the AFM, the solution of rotatable AFM spins was lost as no irreversible transitions are allowed due to the nature of this approximation. It is thus important to remark that, in order to take into account training effects in uncompensated antiferromagnets, it is not sufficient in micromagnetic simulations to model the bias field as a static external field on the ferromagnet. The exact energy terms thus have to be taken into account.

3.4 Implementation of uncompensated AFM interfaces

In MuMax³, we can model an uncompensated antiferromagnet as a pseudo ferromagnetic layer by adding one extra layer with cell thickness t_{AFM} to the simulation box and by coupling this layer to the nearest ferromagnetic layer. We can then attribute some effective parameters such as an anisotropy constant to the AFM layer, as one would do for a normal FM layer. As in MuMax³ a scaling factor is available for the exchange field, one can rescale the exchange field between 2 regions (and by extension also between the FM and AFM layer) to obtain the desired surface energy density J_I , as was defined in the advanced Meiklejohn and Bean model in equation 3.2.

The problem is however that in MuMax³[12] the exchange stiffness and the corresponding exchange energy are attributed to the *volume* of a cell, rather than being defined at the interface between 2 cells. One thus has to map a 2D interface effect to a 3D simulation, i.e. one has to divide the surface energy density J_I between 2 micromagnetic cells to set a volume energy density ϵ . The exchange energy density $\epsilon_{\text{exch},1}$ attributed to a micromagnetic cell with normalised magnetisation vector \mathbf{m}_1 and saturation magnetisation M_s , due to the interaction with a neighbouring cell with normalised magnetisation vector \mathbf{m}_2 and equal saturation magnetisation M_s , is given by

$$\epsilon_{\text{exch},1} = -\frac{1}{2}M_s \cdot \mathbf{B}_{\text{exch},1} \quad (3.18)$$

⁷This is the limit of our approximated solution as we renormalised the total energy $\sigma_{\text{eff}}(\beta, \phi^*(\beta))$ by substituting the solution which minimizes the energy of the AFM macrospin.

with the exchange field defined as

$$\mathbf{B}_{\text{exch},1} = \frac{2A_{\text{ex}}}{M_s} \left(\frac{\mathbf{m}_2 - \mathbf{m}_1}{\Delta^2} \right) = -\mathbf{B}_{\text{exch},2} \quad (3.19)$$

where A_{ex} is the exchange stiffness and Δ the separation between the 2 cells.

When 2 cells have different exchange stiffnesses and saturation magnetisations however, the exchange field is defined by using the harmonic mean α_{H} of the quantity $\frac{A_{\text{ex}}}{M_s}$, i.e.

$$\mathbf{B}_{\text{exch},1} = 2S\alpha_{\text{H}} \left(\frac{\mathbf{m}_2 - \mathbf{m}_1}{\Delta^2} \right) \quad (3.20)$$

$$\alpha_{\text{H}} = \left(\frac{2}{\frac{M_1}{A_1} + \frac{M_2}{A_2}} \right) \quad (3.21)$$

where an arbitrary dimensionless scaling factor S is introduced, which allows us to rescale the exchange field between 2 different regions.

One can calculate the value of the scaling factor S , required to obtain a surface energy density J_1 , by equating the theoretical surface energy density (equation 3.2 with a constant energy shift) as defined in the model of Meiklejohn and Bean

$$\sigma_{\text{I}} = -J_1 [\cos(\beta - \phi) - 1] \quad (3.22)$$

with the surface energy density between the FM/AFM layer as is defined in MuMax³

$$\begin{aligned} \sigma_{\text{I}} = & -\frac{1}{2} \left[\frac{M_{\text{FM}} 2S\alpha_{\text{H}}}{C_z^2} \mathbf{m}_{\text{FM}} \cdot (\mathbf{m}_{\text{AFM}} - \mathbf{m}_{\text{FM}}) \right] C_z \\ & - \frac{1}{2} \left[\frac{M_{\text{AFM}} 2S\alpha_{\text{H}}}{C_z^2} \mathbf{m}_{\text{AFM}} \cdot (\mathbf{m}_{\text{FM}} - \mathbf{m}_{\text{AFM}}) \right] C_z \end{aligned} \quad (3.23)$$

where $C_z = t_{\text{AFM}}$ is the cell size perpendicular to the interface. We find that the scaling factor S has to be given by

$$S = \frac{J_1 C_z}{\alpha_{\text{H}} (M_{\text{FM}} + M_{\text{AFM}})} \quad (3.24)$$

Saturation magnetisation of the AFM layer

To divide the interface energy density J_I equally between a FM and an AFM cell, one has to set the saturation magnetisations (as micromagnetic input parameters in MuMax³) of the ferromagnet and antiferromagnet to equal values, i.e. $M_{\text{FM}} = M_{\text{AFM}}$. Only in this case, one can associate⁸ a symmetric exchange stiffness A_I at the FM/AFM interface given by $A_I = \frac{J_I C_z}{2}$ and so the FM as well as the AFM cell receives in MuMax³ an energy density contribution which is given by

$$\epsilon_{\text{ex}} = -A_I \left(\frac{m_2 - m_1}{C_z^2} \right) \cdot m_1 \quad (3.25)$$

due to the interface interaction and is thus independent of the saturation magnetisation. As no magnetostatic energy is taken into account for the AFM layer, the restriction $M_{\text{FM}} = M_{\text{AFM}}$ has no influence on the energy terms in our micromagnetic simulations. If every term in the effective field, present in an AFM cell, scales as $\frac{1}{M_{\text{AFM}}}$, this amounts to a rescaling of the time in the Landau-Lifshitz-Gilbert equation 1.55. The direction of the effective field however is not changed and thus still points in the direction of minimal energy. One can take into account the Zeeman energy for the AFM layer by appropriately rescaling the magnitude of the external field. To conclude, one only has to introduce the correct scaling factor S (equation 3.24) in MuMax³ corresponding to a certain value of J_I . By dividing the AFM layer into several grains, one can locally vary the coupling constant J_I by varying the scaling factor S at the FM/AFM interface and one can thus model rotatable as well as pinned AFM grains in one simulation.

Evaluation of the exchange energy density

As a consequence of the introduction of pinned antiferromagnetic spins, the continuity requirement⁹ of the magnetisation M in the micromagnetic framework is broken. When the FM is reversed to an antiparallel state with the field cooling direction, the frozen AFM spins make an angle of 180° with the FM. Because the approximation of the exchange energy density between 2 neighbouring spins, as follows from the Taylor expansion of the Heisenberg Hamiltonian, is only valid when the angle between the magnetisation vectors in 2 neighbouring cells is small (typically smaller than

⁸In the FM cell we have an exchange stiffness A_{FM} and in the AFM cell an exchange stiffness A_{AFM} . This association is purely pro forma, i.e. the interaction behaves as if there would be an exchange stiffness A_I between the FM and AFM cell.

⁹See section 1.4.1.

25°), one could be concerned about the evaluation of the exchange energy in our model. This is not a problem however as we do not rely on the continuity condition anymore because the surface energy density linked to the interface interaction has the form $\sigma_1 = -J_1 \cos(\beta - \phi)$ as was defined in the advanced Meiklejohn and Bean model (equation 3.2). Whereas in the discrete atomic model the exchange interaction is defined by the Heisenberg Hamiltonian and so by the cosine of the angle between 2 spins, this is replaced by $(\nabla m)^2$ in the micromagnetic theory, as can be seen in equation 1.32. In MuMax³ however, this exchange energy is approximated by a cosine again and so in our non-continuous model, the used exchange stiffnesses are correct and no renormalisation of the parameters is needed.

Dynamics in the AFM layer

As was pointed out already, the interaction between an uncompensated AFM and a FM layer is modelled by considering the AFM as a pseudo ferromagnetic layer and by correctly matching the energy terms between the theoretical Meiklejohn and Bean model and the implementation of the exchange energy in MuMax³. As exchange bias and athermal training are static effects, precession is not important in our simulations. To correctly implement the dynamics of antiferromagnets, one should move to an atomic scale, consider a cell size equal to the lattice constant and take into account the 2 sublattices. This atomistic approach would lead to very small time steps due to the high frequency precession (order of several hundreds of GHz) of the AFM spins, induced by the exchange interaction between the 2 sublattices[70, 71].

3.5 Testing the micromagnetic model

To test the implementation of our micromagnetic model for uncompensated spins, an infinite FM/AFM bilayer was simulated. Both layers have a thickness $t_{\text{AFM}} = t_{\text{FM}} = C_z = 3.5$ nm and the demagnetisation energy of the ferromagnet was not considered in order to compare our results with the theoretical curves (section 3.2) in the macrospin approach. For the FM typical parameters of permalloy (Py) were used, i.e. $A_{\text{FM}} = 1.3 \times 10^{-11}$ J/m, $M_{\text{FM}} = 800$ kA/m and no magnetocrystalline anisotropy was taken into account. For the AFM layer we set $M_{\text{AFM}} = M_{\text{FM}}$ as discussed in section 3.4 and $A_{\text{AFM}} = A_{\text{FM}}$ as this is not a critical parameter due to the uniformness of both layers.

The FM and AFM layer were coupled using the scaling factor S , as discussed above and hysteresis loops were simulated for different cases. The result of these simulations is shown in figure 3.3. Reduced units were used

$$j_A = \frac{J_A}{\kappa} \quad k_A = \frac{K_{\text{AFM}}t_{\text{AFM}}}{\kappa} \quad j_I = \frac{J_I}{\kappa}$$

with $K_{\text{AFM}} = 1 \times 10^5 \text{ J/m}^3$ (if not 0 or infinite) and $\kappa = K_{\text{AFM}}t_{\text{AFM}} = 0.35 \text{ mJ/m}^2$ a constant scaling factor. Theoretical results (see equations 2.9, 3.9 and 3.10) are not shown as they almost coincide with the simulated curves.

One can see that in the case $j_A = 0$, $k_A = 1$, the bias field vanishes for $j_I \geq 1$ as then the AFM spins rotate together with the FM and induce an enhanced coercivity. As was discussed in [20], three types of hysteresis loops (figure 3.4) can be distinguished. For $j_I \leq 1$, the ferromagnet exhibits continuous rotation as the almost pinned antiferromagnet induces a unidirectional anisotropy and so the bias field is given by equation 3.9. In case $1 \leq j_I \leq 2$, the AFM first rotates reversibly and afterwards switches irreversibly together with the FM towards negative saturation. In this case, equation 3.9 represents the enhanced coercivity¹⁰ instead of the bias field. When $j_I \geq 2$, the AFM rotates irreversibly with the ferromagnet which also leads to an enhanced coercivity. The function $j_A = 0$, $k_A = \infty$ represents the theoretical curve as was originally predicted by Meiklejohn and Bean, given in equation 2.9. Also the approximated solution (purple line in figure 3.3) of the bias field for $k_A = 1$, as follows from equation 3.17, is shown for comparison. It is clear that the small canting angle approximation is not valid anymore when the AFM rotates together with the FM.

When $k_A = 0$ and $j_A = 1$ (blue line in figure 3.3), the uncompensated AFM layer was coupled to an underlying pinned layer to induce the unidirectional anisotropy, related to the parameter J_A . No irreversible switching of the AFM can be observed as the energy term $J_A \cos(\phi)$ in equation 3.2 can only induce exchange bias.

In case j_A as well as k_A are different from zero (yellow line), no closed analytical expression for the bias field is available. When $j_I \lesssim 1.7$, only a bias field with a vanishing coercivity can be obtained as the AFM layer does not switch together with the ferromagnet.

¹⁰Also in this case, $\beta^* = \frac{\pi}{2}$ is an extremum of the total energy as was discussed before.

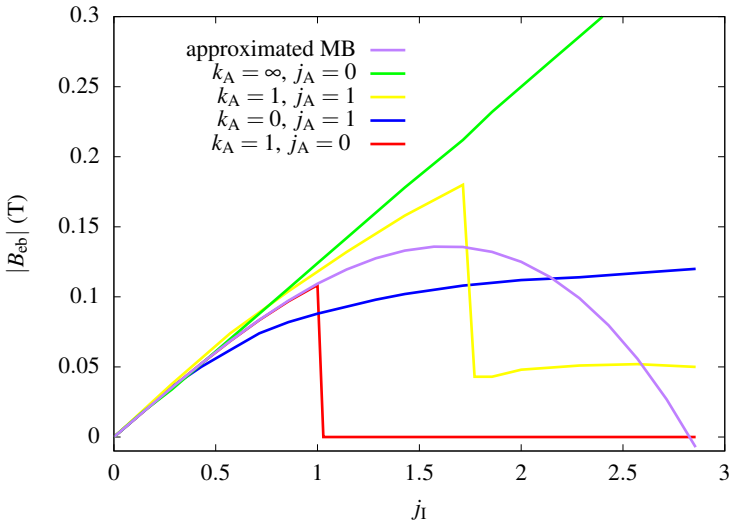


Figure 3.3: Simulated curves for different values of the reduced parameters k_A and j_A as a function of the reduced interface coupling j_I . The purple line represents the approximated solution for small canting angles as is given in equation 3.17.

For $j_I \gtrsim 1.7$, the AFM rotates together with the FM layer, leading to a finite coercivity analogous to the case in which $j_I > 1$ with $j_A = 0$ (red line). This results in a reduction of the bias field, induced by the unidirectional energy term $J_A \cos(\phi)$. As expected, one can thus obtain a finite exchange bias field as well as an enhanced coercivity in this regime, which leads to the conclusion that the yellow curve can be qualitatively described by a combination of the red and the blue curves. Due to the coupling of the antiferromagnet with the underlying pinned layer, the critical value $j_I = 1$ has shifted towards $j_I \approx 1.7$.

It is clear (see figure 3.5) that also the $\frac{1}{j_{\text{FM}}}$ dependence of the bias field is satisfied. A small difference between the micromagnetic model and the analytical solution is found because the external field was applied at an angle of 1° with the field cooling direction to break the symmetry in the system. This shows that our implementation of the advanced Meiklejohn and Bean model in MuMax³ is correct and can be used to study more advanced magnetic systems, e.g. training effects in a polycrystalline antiferromagnet.

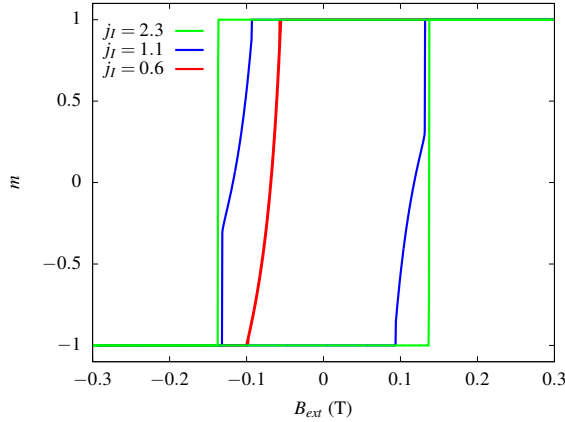


Figure 3.4: In case $k_A \neq 0$ and $j_A = 0$, one can discriminate between 3 types of hysteresis loops, depending on the reduced coupling constant j_I . Only for $j_I \leq 1$ (red curve) a non vanishing value for the bias field is observed. Notice that for $j_I \leq 2$, the angle $\beta^* = \frac{\pi}{2}$, corresponding to $m = 0$, is a stable solution as discussed in section 3.2.

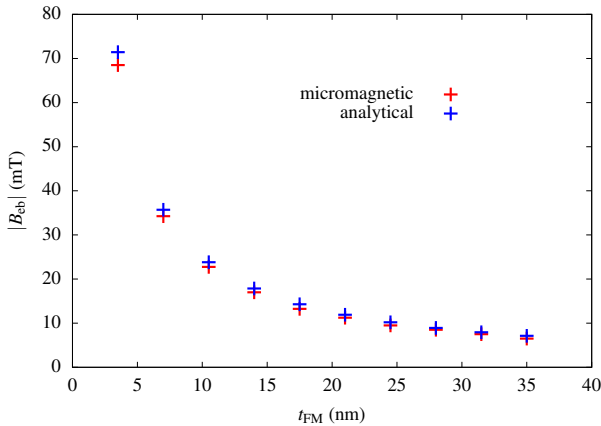


Figure 3.5: Ferromagnetic thickness dependence of the bias field. The small difference between the analytical curve and the simulated values arises from the introduction of a small angle to break the symmetry in the system.

3.6 Example: Training effects in a Co/CoO bilayer

3.6.1 Introduction

As discussed, the unidirectional shift of the hysteresis loop and the athermal training effect are two key features of the exchange bias phenomenon in most polycrystalline FM/AFM bilayers. In this section, we will show that we can reproduce experimental data of a polycrystalline Co/CoO bilayer. Using a Voronoi tessellation, MuMax³ allows us to consider a FM or AFM layer as consisting of many individual grains (coupled or uncoupled), which have their own set of parameters. By defining a local varying coupling constant between both layers, we can generate the shift of the hysteresis loop due to pinned uncompensated spins and the athermal training effect due to rotatable uncompensated spins in the AFM. The results from these micromagnetic simulations are compared to experimental data of a Co(30nm)/CoO(3nm) bilayer as reported by Dias et al in [60].

We also demonstrate that we can reinitialise the bilayer to an apparent field cooled state and that the reversal mechanism between the ascending and descending branch in the first hysteresis loop can be different, as has frequently been noticed[72].

3.6.2 Micromagnetic model

The ferromagnetic material (in our case Co) is divided into grains with an average grain size of 12 nm using a 2D Voronoi tessellation. The parameters for the Co layer are those which are typically found in literature: a saturation magnetisation M_{FM} of 1400 kA/m and an exchange stiffness of 30 pJ/m. The uniaxial anisotropy axes of the grains are distributed around 0° (parallel to the field cooling direction) according to a normal distribution[60, 73] with a standard deviation $\sigma = 10^\circ$. Within each grain the uniaxial anisotropy direction and the magnetocrystalline anisotropy constant K_{FM} is taken to be the same.

The bottom layer, with a thickness of 3 nm, represents the antiferromagnetic CoO layer and is also divided into grains with the same grain size, but not coinciding with the FM grains. The grains are divided into 2 types¹¹: rotatable and pinned AFM grains, in a ratio of 7:3 respectively. The pin-

¹¹See the discussion of the advanced Meiklejohn and Bean model in section 3.5

ning density is not a fixed a priori known parameter. Typical values for the pinning density of an antiferromagnet can range from a few percent[56], up to 80% for an epitaxial CoO(3 nm)/Fe/Ag(001) stack[74]. Both types have their own uniaxial anisotropy constant, given by $K_{\text{AFM,rot}}$ and $K_{\text{AFM,pin}}$, and their anisotropy axes are randomly distributed in the xy plane. Although possible, the AFM intergrain interaction was not taken into account.

The simulation box was discretised into 10 FM + 1 AFM cells in the z direction. The cell size was chosen to be $2.5 \times 2.5 \times 3 \text{ nm}^3$ with a total number of $512 \times 512 \times 11$ cells. To eliminate finite size effects, periodic boundary conditions (10, 10, 0) were applied in the x and y direction and so a macroscopic sample was approximated. Field cooling was simulated by starting from an initial uniform magnetisation (in the AFM as well as in the FM) that was relaxed in an external field of 100 mT, a field larger than necessary to saturate the FM. Two subsequent hysteresis loops were simulated along the field cooling direction with $|B_{\text{ext}}|$ between 0 and 100 mT. Using the Brown model[12] 10 K thermal fluctuations were applied at each field step (step size = 0.5 mT) during 0.5 ns to eliminate any metastable equilibrium states. This is not sufficiently long however to induce thermal training effects. After thermal fluctuations have been applied, the system was relaxed so a quasistatic hysteresis loop was obtained.

3.6.3 Results

In order to match our simulations with the experimental hysteresis loop[60] we used that $K_{\text{FM}} = 2.0 \times 10^4 \text{ J/m}^3$ and a standard deviation σ of 10° for the distribution of the uniaxial FM axes. The fact that the ferromagnetic anisotropy constant is an order of magnitude lower than bulk hcp cobalt can be explained by stacking faults and the coexistence of the fcc and hcp phase in the considered sample.[75, 76, 60]

The bulk AFM anisotropy¹² constant[77, 78] $K_{\text{AFM,pin}} = 2.7 \times 10^7 \text{ J/m}^3$ is attributed to the pinned grains while the anisotropy constant of the rotatable grains is set approximately 10 times lower, i.e. $K_{\text{AFM,rot}} = 2.0 \times 10^6 \text{ J/m}^3$. The exchange stiffness A_{A} inside the AFM grains was chosen to be 4.0 pJ/m, a value similar to that of other antiferromagnets such as IrMn and

¹²One typically finds[58] an anisotropy energy of $J_{\text{K}} = 3 \text{ meV}$ per Co^{2+} ion in CoO. In a NaCl structure, there are 4 Co ions per unit cell and so one finds that $K_{\text{AFM}} = \frac{4J_{\text{K}}}{a^3} \approx 2.5 \times 10^7 \text{ J/m}^3$ with $a = 0.427 \text{ nm}$ the lattice constant of CoO.

FeMn.[79] From the enhanced Meiklejohn and Bean model (section 3.2), it follows that as long as $K_{\text{AFM,pin}}$ and A_A are high enough so that the pinned grains are almost fixed and each rotatable grain is homogeneous within itself, the exact value of these parameters is not crucial in our model. An AFM grain will be pinned when $K_{\text{AFM,pin}}t_{\text{AFM}}$ is larger than the local coupling parameter J_I , as is the case in our simulations. $K_{\text{AFM,rot}}$ has been chosen in such a way that we are able to reproduce the experimental data. As coupling constants at the interface between the FM and AFM layer we found that $A_{\text{I,pin}} = 6.9 \times 10^{-12}$ J/m and $A_{\text{I,rot}} = 1.1 \times 10^{-11}$ J/m. These are realistic values as we can expect that $A_A \leq A_I \leq A_{\text{FM}}$ for a Co/CoO bilayer.

Exchange bias field and coercivity

Using the model and the parameters described above, we obtained the hysteresis loop displayed in figure 3.6. The average x and y components of the ferromagnetic layer are shown. For the bias field and coercivity one finds for the first hysteresis loop that $B_{\text{eb}} = 35$ mT and $B_c = 42$ mT and for the second hysteresis loop that $B_{\text{eb}} = 22$ mT and $B_c = 29$ mT.

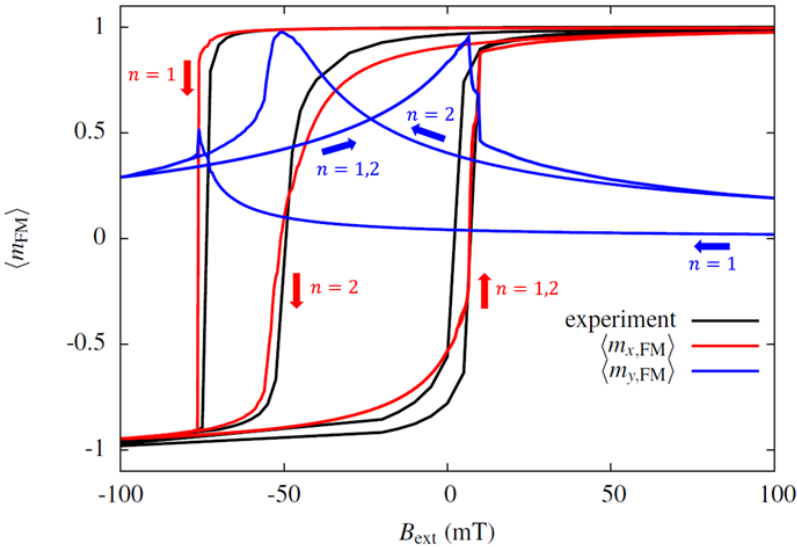


Figure 3.6: Hysteresis loop of the average x (red line) and y (blue line) component of the ferromagnetic Co layer. Black curves represent the experimental data[60] for $n = 1$ and $n = 2$.

When comparing the descending branch of the first and second hysteresis loop, one clearly observes the athermal training effect. The hysteresis loop width shrinks approximately 30%, which is a rather large effect. The difference in squareness between the descending and ascending branch of the first hysteresis loop is also prominent and is a typical feature of the athermal training effect. There is a good quantitative agreement between our macromagnetic simulations and the experimental data, reported by Dias et al.[60] Note that in our model no thermal training is present and no AFM intergrain interaction was taken into account, so we cannot reproduce the decrease in bias field and coercivity for $n = 2$.

As discussed in section 3.4, we can convert the exchange stiffnesses A_I into local surface energy densities J_I by using that $J_I = \frac{2A_I}{C_z}$ and so we get a surface energy density of approximately 4.6 mJ/m² and 7.3 mJ/m² for the pinned and rotatable grains, respectively. Although the coupling parameter J_I between the FM and AFM layer seems rather high, one has to take into account that a local coupling between the 2 layers was defined, i.e. J_I represents the surface energy density for a perfectly uncompensated AFM layer. Interface energies for ideal uncompensated surfaces range typically from several mJ/m² up to theoretical predicted values of 10 mJ/m²[80]. Most of the AFM grains in our model do not contribute to the exchange bias field however. Taking into account that only 30% of the AFM grains are pinned and that their anisotropy axis is randomly distributed in the positive x direction¹³, we get an effective surface energy density of $\frac{2}{\pi} \left(\frac{30 \times J_{I,\text{pin}}}{100} \right) \approx 0.88$ mJ/m² which is in accordance with typical values for CoO found in other experiments[81]. The average experimentally measurable coupling constant is often defined by using the rigid Meiklejohn - Bean model (section 2.9) from which it follows that $B_{\text{eb}} = \frac{\langle J_I \rangle}{M_{\text{FM}} t_{\text{FM}}}$ with t_{FM} the thickness of the ferromagnet. Using the experimental value for the average bias field $B_{\text{eb}} \approx 22$ mT, one obtains an average coupling constant $\langle J_I \rangle \approx 0.92$ mJ/m² which is approximately the same value. One has to bear in mind that only the effective coupling constant will determine the shift of the hysteresis loop. Choosing a different fraction of pinned AFM grains, only leads to a rescaling of the coupling constant $A_{I,\text{pin}}$. This can lead to a change in the shape of the hysteresis loop however, as one then changes the fraction of rotatable antiferromagnetic spins.

¹³Averaging $\cos(\alpha)$ over the angles $\alpha = -\frac{\pi}{2} \dots \frac{\pi}{2}$ leads to a factor $\frac{2}{\pi}$.

Athermal training effect and asymmetry

After field cooling, the AFM grains have their magnetisation close to their anisotropy axis which results in a random distribution of $m_{y,\text{AFM}}$ and so $\langle m_{y,\text{AFM}} \rangle \approx 0$. During the first field sweep towards negative saturation, the rotation direction of the FM and thus also of the rotatable AFM spins is determined by the initial net imbalance of the average y component $\langle m_y \rangle$ of the system. For $\langle m_y \rangle > 0$ the magnetic system will rotate counterclockwise, eventually leaving the system with an even larger net imbalance after negative saturation due to the interaction between the FM and AFM. Especially the AFM grains with an anisotropy axis almost perpendicular to the field cooling direction will contribute to this effect. The average orientation of rotatable AFM grains with anisotropy axes almost perpendicular to the field cooling direction ($\theta_u = 96^\circ$) and an initial $m_{y,\text{AFM}} < 0$ is illustrated in figure 3.7. After field cooling, its magnetisation (a) makes an angle of -56° with respect to the cooling field direction, due to the interaction with the saturated FM layer. As discussed, this grain will rotate counterclockwise during the first reversal of the FM and will relax towards position (b) in which $m_{y,\text{AFM}} > 0$. After the first cycle, one can see that the AFM grain makes an angle of 70° with respect to the field cooling direction and relaxes towards position (c) when the FM layer is saturated. Thus, the magnetisation of these AFM grains does not return to its initial field cooled state. From the second loop, the magnetisation of the grain switches only between positions (b) and (c). Rotatable AFM grains whose anisotropy axes are almost perpendicular to the externally applied magnetic field, but who have an initial $m_{y,\text{AFM}} > 0$ keep their positive y component at saturation.

In the second loop ($n = 2$), the FM and rotatable AFM grains will rotate coherently again, in this case counterclockwise due to $\langle m_y \rangle > 0$. Because after the first cycle the AFM layer also has a net y component $\langle m_{y,\text{AFM}} \rangle > 0$, perpendicular to the external field, it applies a torque on the FM layer and so results in lower value for the coercive field in the descending branch, which produces the athermal training effect. The same mechanism has been reported in [82]. In figure 3.8, one can see that the first hysteresis loops of the x and y components of the AFM layer are not closed. This results from a redistribution of the magnetisation of the rotatable AFM grains after the first hysteresis cycle, which leads to the fact that the descending branch in the first hysteresis loop is more rectangular than the ascending branch.

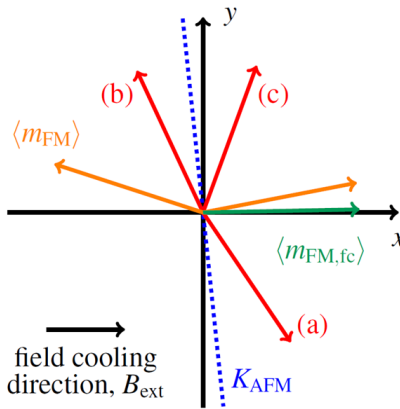


Figure 3.7: Average orientation of rotatable AFM grains (red arrows) with anisotropy axes (dashed blue line) almost perpendicular to the field cooling direction and initial $m_{y,AFM} < 0$. The average magnetisation $\langle m_{FM,fc} \rangle$ of the FM layer after field cooling is indicated by the green arrow. The average magnetisation of the FM layer at positive and negative saturation ($n = 2$) are indicated by the orange arrows. Position (a): magnetisation of rotatable AFM grain after field cooling. (b): magnetisation of rotatable AFM grain at $B_{ext} = -100$ mT during the first hysteresis loop. (c) magnetisation of rotatable AFM grain at $B_{ext} = 100$ mT after the first hysteresis loop.

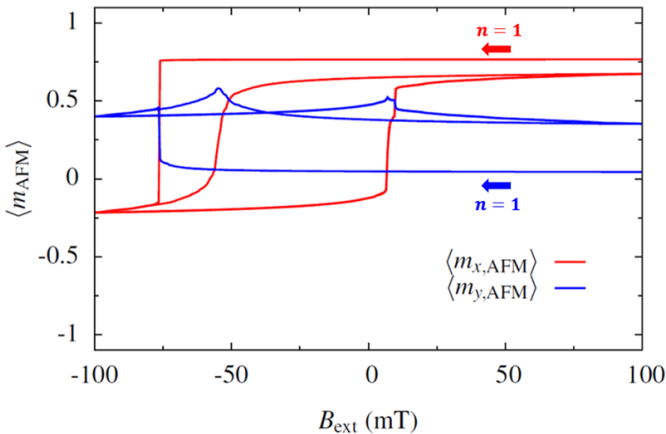


Figure 3.8: Hysteresis loop of the average x (red line) and y (blue line) component of the antiferromagnetic CoO layer.

This can also clearly be seen (figure 3.9) when comparing the magnetisation of the AFM grains in their field cooled state with their magnetisation after the first hysteresis loop. In figure 3.9a the AFM grains with a magnetisation aligned along the positive (green/orange domains) and negative (purple/blue domains) y axis are randomly and equally distributed after field cooling. After the first hysteresis cycle (figure 3.9b), there are however more AFM grains aligned along the positive y -direction than along the negative y -direction.

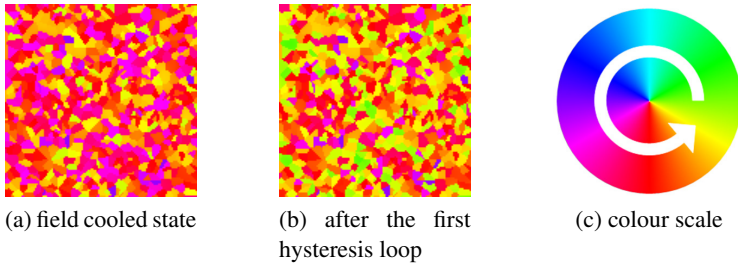


Figure 3.9: Magnetisation direction of the AFM grains in the CoO layer at $B_{\text{ext}} = 100$ mT. A quarter of the total simulation box is shown. Figure (a) shows the magnetisation of the AFM after field cooling, with $\langle m_{y,\text{AFM}} \rangle \approx 0$. Figure (b) shows the magnetisation after the first hysteresis loop, with $\langle m_{y,\text{AFM}} \rangle > 0$. In figure (c) the colour scale of the magnetisation has been displayed. Red: magnetisation along the positive x axis, green: magnetisation along the positive y axis.

A similar reasoning can be applied to regions in which $\langle m_y \rangle < 0$ after field cooling. The sign of $\langle m_y \rangle$ has no effect however on the average exchange bias field nor the training effect as the initial net imbalance after field cooling only determines the direction in which the FM rotates. In a real macroscopic sample, one could expect that regions with positive as well as negative net $\langle m_y \rangle$ imbalances are present.

Reinitialisation to an apparent field cooled state

The antiferromagnet can partially be restored to its initial field cooled state by performing an in plane field sweep, perpendicular to the field cooling direction as has been discussed in [83] and [84]. In this way, the y component of some rotatable AFM grains become negative¹⁴ again, which leads

¹⁴when considering the same symmetry breaking, i.e. that after field cooling $\langle m_y \rangle > 0$.

to a random distribution and so an average $\langle m_{y,\text{AFM}} \rangle \approx 0$ as in the initial field cooled state. After completing the first 2 field cycles (red line in figure 3.6), a field sweep along the y direction was simulated, in which $B_{\text{ext},y}$ starts from $0 \rightarrow B_{\text{max}} \rightarrow -B_{\text{max}} \rightarrow 0$. Taking into account that for $n = 1$ the reversal happens through coherent rotation so that $\langle m_{y,\text{AFM}} \rangle > 0$ after the training, we notice in figure 3.10 that the AFM grains (on average) behave reversible in the perpendicular hysteresis loop for $B_{\text{ext},y} \geq 0$, which is in the direction of the net $\langle m_{y,\text{AFM}} \rangle$ after the system was trained. In the area $B_{\text{ext},y} \leq 0$ some AFM grains make irreversible jumps from $m_y > 0$ to $m_y < 0$ and thus reinitialisation is achieved. If the value of B_{max} is too small, the bilayer will only be partly reinitialised.

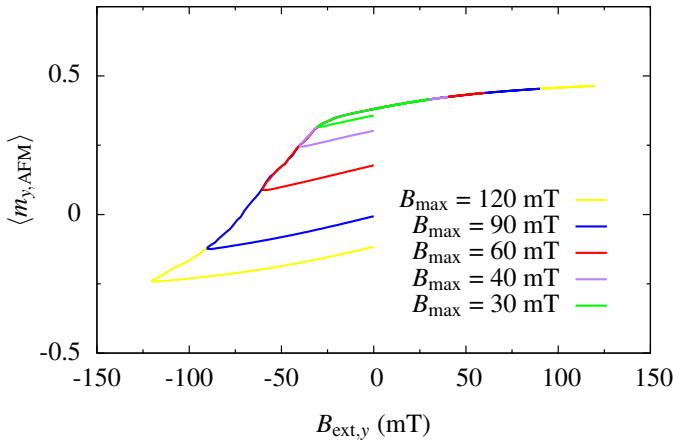


Figure 3.10: Field loop of the average y component of the AFM layer for different values of B_{max} . The external field is applied perpendicular to the field cooling direction in order to achieve reinitialisation of the AFM layer.

One can see that for $B_{\text{max}} \approx 90$ mT, the average y component of the AFM layer vanishes. Afterwards, 2 new field sweeps (blue line in figure 3.11) were simulated along the field cooling direction. As expected, we again notice the presence of the athermal training effect. In contrast to the field cooled loop, the reversal in the descending branch for $n = 1$ now happens through the formation of domains in the FM and thus corresponding domains in the AFM, which leads to large regions with $m_{y,\text{AFM}} > 0$ as well as $m_{y,\text{AFM}} < 0$ in the AFM. This can be seen in figure 3.12.

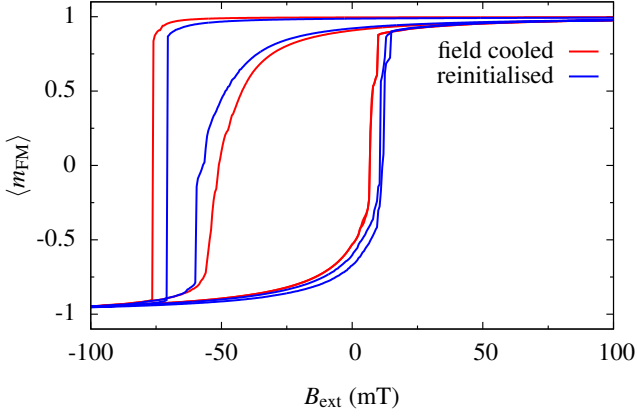


Figure 3.11: Hysteresis loop of the average x component of the FM layer. The red line represents the hysteresis loop after field cooling and the blue line represents the hysteresis loop after reinitialisation by applying a perpendicular magnetic field.

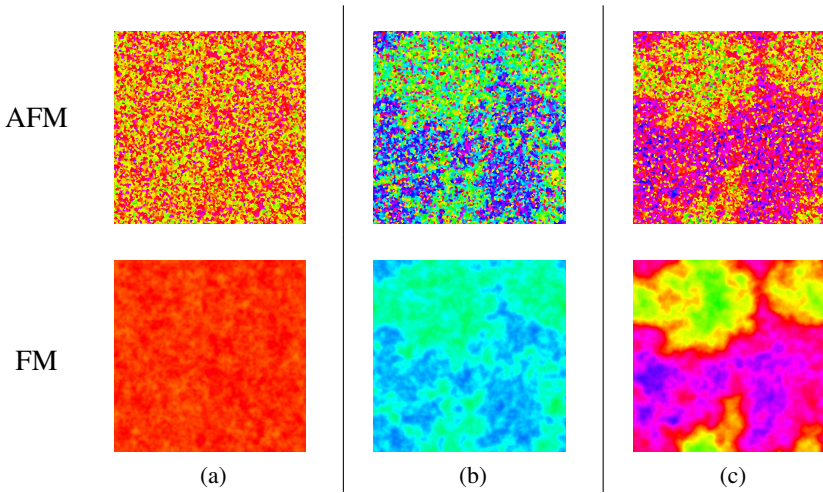


Figure 3.12: Magnetisation of the AFM (top) and corresponding FM (bottom) layer for the reinitialised ($B_m = 90$ mT) hysteresis loop. (a): for $n = 1$ at $B_{ext} = 100$ mT, (b): for $n = 1$ at $B_{ext} = -100$ mT, (c): for $n = 2$ at $B_{ext} = -45$ mT in the descending branch.

In this case, each side of the perpendicular hysteresis loop is irreversible. These AFM regions do not cease to exist, even when the ferromagnet is saturated and as such they exert a torque on their corresponding FM regions, as already discussed before in the field cooled case. The reversal in the ascending branch for $n = 1$ and all subsequent cycles, ascending as well as descending, happens through coherent rotation of the FM domains. Training can also be found for $n \geq 1$ due to a small reorientation of the AFM grains. The asymmetry in the reversal mechanism between the descending and ascending branch for $n = 1$ has been experimentally observed in Co/CoO bilayers by using polarized neutron reflectometry[72].

Also a second reinitialisation was simulated and a very similar loop, with corresponding training effect, was found. We can conclude that the net effect of applying a perpendicular hysteresis loop after the training effect will lead to a reinitialisation of the AFM layer and so to an apparent field cooled state, this without heating the sample above the Néel temperature.

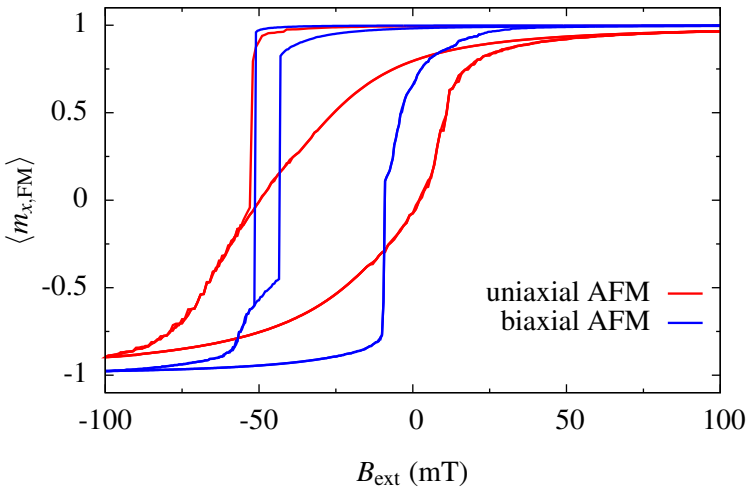


Figure 3.13: Hysteresis loop of a simulation in which the anisotropy axes of the FM grains ($K_{FM} = 2.0 \times 10^4 \text{ J/m}^3$) are randomly distributed and in which the anisotropy axes of the AFM grains ($K_{AFM,rot} = 2.0 \times 10^6 \text{ J/m}^3$) also have a random uniaxial distribution (red line) or have a random biaxial anisotropy (blue line).

In order to reproduce the experimental hysteresis loop[60], we have attributed a uniaxial normal anisotropy distribution to the FM grains and a random uniaxial distribution to the AFM grains. We have also performed simulations in which the anisotropy of the FM grains is randomly distributed and in which the AFM grains have a biaxial anisotropy. The results are shown in figure 3.13. Also in these cases athermal training was found. This shows that the model we propose is a general mechanism for obtaining training effects and is not limited to AFM grains with a uniaxial anisotropy.

3.7 Example: Positive exchange bias fields

Using the basic Meiklejohn and Bean model, one can only produce negative exchange bias for positive as well as negative coupling constants J_1 , assuming the antiferromagnet is in its global energy minimum after cooling. We also noted in section 2.3.4 that, in a first approximation, the Zeeman energy of the AFM doesn't need to be taken into account in case of low cooling fields as the interface coupling with the FM appeared to be the determining energy term.

Experiments [85, 86, 87] have however shown that also positive¹⁵ bias fields can be obtained, especially for high cooling fields. This is often explained by taking into account the Zeeman energy of the AFM during field cooling and considering an antiparallel coupling between the FM and AFM, as one has found e.g. in Co/FeF₂ bilayers[88]. An example[89] of the evolution of the exchange bias field as a function of the cooling field for an Fe(12nm)/MnF₂(60nm) bilayer can be seen in figure 3.14. Low cooling fields lead to negative exchange bias as follows from the Meiklejohn and Bean model. High cooling fields produce positive exchange bias in case of an antiparallel coupling between the ferromagnet and antiferromagnet.

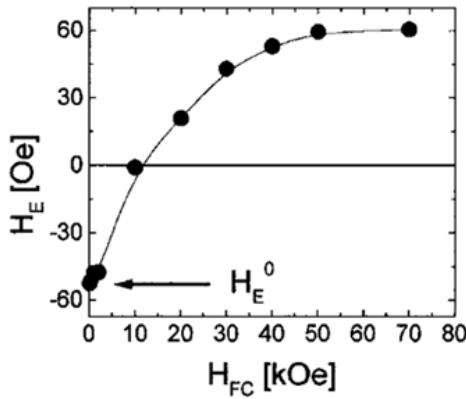


Figure 3.14: Evolution of the bias field as a function of the cooling field for an Fe(12nm)/MnF₂(60nm) bilayer. High cooling fields lead to positive exchange bias. Reproduced from [89].

¹⁵In case of positive exchange bias fields, the hysteresis loop is shifted in a direction parallel to the cooling field.

A model, similar to what was proposed by Kiwi[85] for compensated surfaces, can also be applied to an uncompensated antiferromagnet. Assuming that the cooling field H_{cf} couples to the AFM during field cooling, is oriented along $\gamma = 0$ and demanding that the ferromagnet is saturated in the same direction as the cooling field, we can write the total surface energy density as

$$\sigma(\phi) = J_I \cos(\phi) - K_{AFM} t_{AFM} \cos^2(\phi) - \mu_0 M_{AFM} t_{AFM} H_{cf} \cos(\phi) \quad (3.26)$$

dropping constant energy contributions. The first term is the interface coupling of the AFM with the saturated FM layer, the second term is the uniaxial anisotropy energy of the AFM and the last term is the Zeeman energy of the AFM. We assumed an antiparallel interface coupling between the ferromagnet and the antiferromagnet, but have defined the constant $J_I > 0$ for simplicity.¹⁶ The definition of the angle ϕ is shown in figure 3.15.

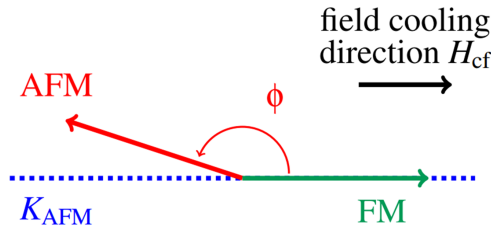


Figure 3.15: Definition of the angle ϕ which the AFM makes with respect to the field cooling direction H_{cf} and the uniaxial axis K_{AFM} . The ferromagnet FM is saturated along the field cooling direction.

Stability positions of the AFM angle ϕ can be found by calculating $\frac{\partial \sigma}{\partial \phi} = 0$. One obtains that the extrema are given by

$$\phi^* = 0 \quad (3.27)$$

$$\phi^* = \pi \quad (3.28)$$

$$\cos(\phi^*) = \frac{J_I - \mu_0 M_{AFM} t_{AFM} H_{cf}}{2K_{AFM} t_{AFM}} \quad (3.29)$$

¹⁶This means that $\phi^* = \pi$ is the global energy minimum for the antiferromagnet when no external field is present.

Calculating the second order derivative to determine when the solutions are minima or maxima shows that $\phi^* = 0$ is minimal for $\mu_0 H_{\text{cf}} \geq \frac{J_1 - 2K_{\text{AFM}}t_{\text{AFM}}}{M_{\text{AFM}}t_{\text{AFM}}}$ and $\phi^* = \pi$ is minimal for $\mu_0 H_{\text{cf}} \leq \frac{J_1 + 2K_{\text{AFM}}t_{\text{AFM}}}{M_{\text{AFM}}t_{\text{AFM}}}$. For the other solution, we find that the condition $\frac{\partial^2 \sigma}{\partial \phi^2} = -2K_{\text{AFM}}t_{\text{AFM}} \sin^2(\phi^*) > 0$ is never satisfied for $K_{\text{AFM}} > 0$. Thus, as can be expected due to the symmetry of the problem, we find that $\phi^* = 0$ and $\phi^* = \pi$ are the only 2 stable solutions, which have a stability overlap in the regions

$$\frac{J_1 - 2K_{\text{AFM}}t_{\text{AFM}}}{M_{\text{AFM}}t_{\text{AFM}}} \leq \mu_0 H_{\text{cf}} \leq \frac{J_1 + 2K_{\text{AFM}}t_{\text{AFM}}}{M_{\text{AFM}}t_{\text{AFM}}} \quad (3.30)$$

As we have assumed $H_{\text{cf}} > 0$ and $\gamma = 0$ for the cooling field and only AFM spins with $J_1 \leq K_{\text{AFM}}t_{\text{AFM}}$ can contribute to a positive (or negative) bias field as discussed in section 3.2, this inequality reduces to

$$0 \leq \mu_0 H_{\text{cf}} \leq \frac{J_1 + 2K_{\text{AFM}}t_{\text{AFM}}}{M_{\text{AFM}}t_{\text{AFM}}} \quad (3.31)$$

If the AFM spins hardly couple to the external field anymore after cooling¹⁷, we thus find that they lead to positive exchange bias if

$$\mu_0 H_{\text{cf}} \geq \frac{J_1 + 2K_{\text{AFM}}t_{\text{AFM}}}{M_{\text{AFM}}t_{\text{AFM}}} \quad (3.32)$$

in case the uncompensated AFM was oriented antiparallel to the FM at initialisation. This threshold value for the cooling field, leading to a stepwise function from $-|B_{\text{eb}}|$ to $+|B_{\text{eb}}|$, was confirmed by micromagnetic simulations.

If we assume a variable interface coupling parameter J_1 and a fixed anisotropy constant K_{AFM} , then the maximal cooling field that needs to be applied for all pinned AFM spins to contribute to positive exchange bias, is given by $\mu_0 H_{\text{cf}} = \frac{3K_{\text{AFM}}}{M_{\text{AFM}}}$ as these spins will become rotatable for $J_1 > K_{\text{AFM}}t_{\text{AFM}}$. At this point, the bias field B_{eb} as a function of the cooling field H_{cf} will saturate.

¹⁷The maximal value of the magnetic field during a field sweep is often much smaller than the cooling field. In an antiferromagnet with a variable coupling parameter J_1 , application of an external field on the antiferromagnet will only lead to a higher number of rotatable spins and thus a reduced bias field. Only when a field sweep is recorded in very high magnetic fields all pinned grains will have become rotatable ones.

The minimal field, necessary to start switching pinned antiferromagnetic spins towards a parallel orientation with the FM, is given by $\mu_0 H_{cf} = \frac{2K_{AFM}}{M_{AFM}}$ if they started from an initially antiparallel state. This corresponds to the anisotropy field as was discussed for a ferromagnet in the Stoner Wohlfarth model (section 1.6). Antiferromagnetic spins¹⁸ which were initially already parallel with the ferromagnet, are in a local energy minimum as follows from the stability overlap. For a polycrystalline antiferromagnet, we can assume that there will be a continuous transition between negative and positive exchange bias, depending on the magnitude of the cooling field H_{cf} , the variation of the anisotropy constant K_{AFM} , the variation of the interface coupling J_I or possibly even both.

As an example, we will consider a 10 nm thick antiferromagnet with a grain size of 12 nm and saturation magnetisation¹⁹ $M_{AFM} = M_{FM}/2$, coupled to a uniform ferromagnet with thickness of 10 nm. The ferromagnet has typical values of Py ($M_{FM} = 800$ kA/m and $A_{FM} = 1.3 \times 10^{-11}$ J/m) and no FM anisotropy was considered. The cell size was chosen to be $2.5 \times 2.5 \times 10$ nm³ and periodic boundary conditions were used to simulate an infinite thin film. The AFM layer has a uniform uniaxial anisotropy axis, but the anisotropy constants of the grains as well as the interface coupling J_I of the grains with the FM layer are varied. The value of the anisotropy constant K_{AFM} of the antiferromagnetic grains was randomly distributed between 0 and 2×10^5 J/m³ and likewise the value of J_I was randomly distributed between 0 and 2 mJ/m² with antiparallel coupling towards the ferromagnet. The cooling field was applied along the positive x axis (parallel to the uniaxial axis of the AFM), the ferromagnet was kept saturated in the field cooling direction and all antiferromagnetic grains were initialised along the negative x direction, corresponding to the global energy minimum when no cooling field is present. The antiferromagnet was relaxed in the cooling field, afterwards the cooling field was removed and the system relaxed again. The rotatable grains with $J_I > K_{AFM}t_{AFM}$ will switch back to an antiparallel position with respect to the ferromagnet. Depending on the magnitude of the cooling field, some pinned grains will make an irreversible transition from the antiparallel state with respect to the ferromagnet to the parallel position.

¹⁸Remark that AFM spins for which $J_I \leq K_{AFM}t_{AFM}$ stay frozen after field cooling.

¹⁹As we need to keep $M_{AFM} = M_{FM}$ in the micromagnetic code to retrieve the correct bias field, as discussed in section 3.4, we will rescale the external field applied on the antiferromagnet with a factor 2 which amounts to the same Zeeman energy.

Starting from this antiparallel state between the FM and the AFM, loops with different magnitudes for the cooling field H_{cf} , were simulated and the bias field was determined using the coercive fields. The result (red curve) is shown in figure 3.16. One can clearly see that for low cooling fields, the bias field is negative as expected. Ramping up the cooling field however leads to positive bias fields, even obtaining a vanishing exchange bias field when as many pinned AFM grains are oriented parallel as antiparallel after field cooling. As the maximal value of the anisotropy constant is given by $K_{AFM,max} = 2 \times 10^5 \text{ J/m}^3$, we expect that saturation of the curve will happen for $\mu_0 H_{cf,max} = \frac{3K_{AFM,max}}{M_{AFM}} \approx 1.5 \text{ T}$, which is in correspondence with figure 3.16. Also a polycrystalline AFM with uniaxial grains was simulated. As in this case the pinned AFM grains are randomly distributed, the bias field at maximal value is reduced by a factor $\frac{2}{\pi}$, compared to the uniaxial case.

The exact shape of these curves depends on the distribution of the coupling parameter J_I and anisotropy constant K_{AFM} in the AFM. Our simulated curve (figure 3.16) is also very similar to the experimental²⁰ curve (figure 2.8) in case the bias field was induced by a net remanent state of the ferromagnetic layer at $T \approx T_N$. Also remark that if the direction of the cooling field is unknown, one cannot use a field loop to distinguish between positive and negative exchange bias.

It is important to note that one cannot obtain positive exchange bias in case of a parallel coupling between the FM and the AFM. If we assume that the antiferromagnet is close to its global energy minimum after cooling in a low magnetic field, the uncompensated AFM will always be oriented in the direction of the FM and thus also in the direction of the cooling field. Increasing the cooling field will, at most, only increase the number of uncompensated spins in the direction parallel to the cooling field and thus in fact lead to a more negative bias field. On the other hand, it is highly unlikely that the AFM would be oriented antiparallel towards the FM after cooling in a low magnetic field. Increasing the cooling field would lead to a change from positive bias fields towards negative bias fields, something which has never experimentally been observed.

²⁰According to our definition, this corresponds to negative exchange bias as the direction of the net remanent state is in fact the relevant parameter.

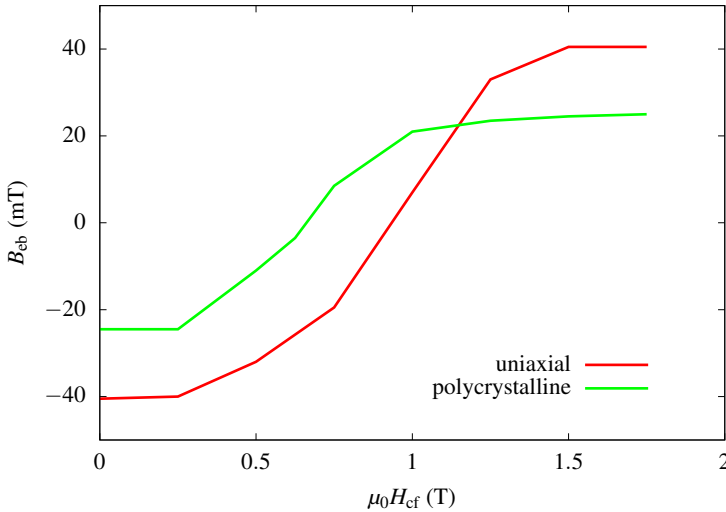


Figure 3.16: Bias field B_{eb} as a function of the cooling field $\mu_0 H_{cf}$. For large cooling fields, the bias field becomes positive.

To obtain positive exchange bias, one thus needs an antiferromagnetic interface coupling and a parallel orientation between the FM and AFM, induced by high cooling fields and stabilized by a high AFM anisotropy.

When in a thin film regions with positive as well as negative exchange bias fields²¹ are present, sometimes a double shifted hysteresis loop can be observed. This was found e.g. in a CrMn(12nm)/Co(90nm) bilayer[90], as is shown in figure 3.17 (left). After several field cycles ($n = 9$) however, the positive biased part disappears, showing that the antiferromagnetic CrMn spins, which were parallel to the Co layer, were in metastable state (local energy minimum) after cooling in a strong magnetic field, as already discussed. Experiments[87] in combination with micromagnetic simulations of a Ni/FeF₂ bilayer show that the double shifted hysteresis loop is only present when the size of the AFM domains with opposite bias fields is much larger than the FM domain wall width, as otherwise the effect of the frozen uncompensated AFM spins is averaged out over the typical FM domain size, leading to an apparent unbiased hysteresis loop.

²¹This corresponds to the transition region in figure 3.16 for intermediate cooling fields.

This mechanism of generating positive exchange bias through an antiferromagnetic coupling between the FM and AFM layer in combination with a strong cooling field, is supported by the study[91] of a LSMO/SRO bilayer, as can be seen in figure 3.17 (right). Although both materials are ferromagnetic, the 2 layers are coupled antiferromagnetically. As SRO has a very high coercivity²² (approximately 1 T), one can pin this layer in a direction (parallel or antiparallel) towards the external field that switches the LSMO layer, thus leading to positive or negative bias fields respectively.

The exact origin of positive bias fields is still under debate however and more systematic experimental and micromagnetic studies are needed.

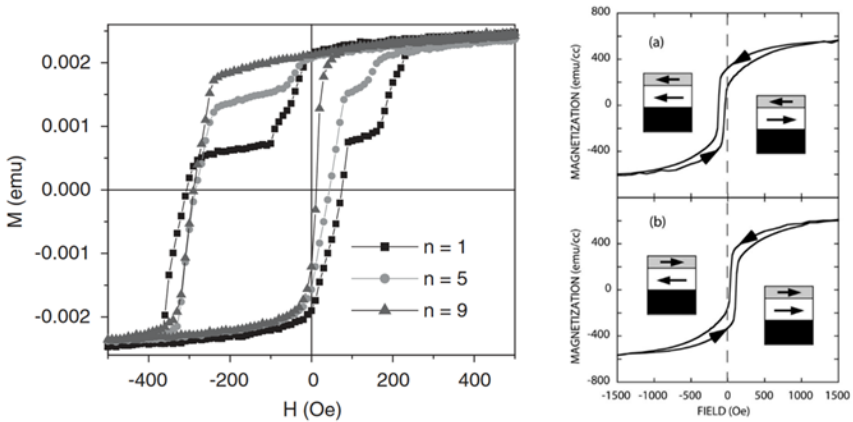


Figure 3.17: Left: hysteresis loop of a CrMn(12nm)/Co(90nm) bilayer, showing the double shifted loops. The loop, corresponding to positive exchange bias, disappears while training the sample. Right: Positive and negative biased hysteresis loop in LSMO/SRO bilayer. Black layer: STO seed layer, white layer: LSMO, grey layer: SRO. LSMO as well as SRO are both ferromagnets, but are coupled antiferromagnetically. Top: negative bias. Bottom: positive bias. Reproduced from [90] and [91].

²²In this system, the ferromagnetic SRO layer behaves analogous to the frozen AFM spins which have a high anisotropy constant.

3.8 Conclusions

Although MuMax³ was designed to study static and dynamic effects in ferromagnets, we have shown that we were able to model an uncompensated AFM interface by adding 1 extra pseudo ferromagnetic layer to the simulation box. Using this implementation, we were able to simulate the athermal training effect and obtain realistic results for an exchange biased bilayer, taking into account the local granular structure of the antiferromagnet. We can reach a good quantitative agreement between our micromagnetic simulations and the experimental data. This without the necessity to approximate the bias field as a static local varying magnetic field which cannot produce any training effects. We have shown that uncompensated rotatable grains in a polycrystalline antiferromagnet can be responsible for a reduction of the coercivity and the bias field, as has been confirmed by experimental data. The asymmetry between the descending and ascending branch in the first field cycle ($n = 1$) is induced by the metastable state of the rotatable AFM spins after field cooling. Through our simulations we have also confirmed that a bilayer, after the system was trained, can be reinitialised to an apparent field cooled state by applying an external magnetic field, perpendicular to the field cooling direction. By considering the cooling field on the pinned antiferromagnetic grains, one can also explain positive exchange bias fields in the case of an antiparallel coupling between the ferromagnet and the antiferromagnet.

MODELLING COMPENSATED AFM INTERFACES IN MUMAX³

Paper II

Modelling compensated antiferromagnetic interfaces with MuMax³[2]

Full micromagnetic calculations show the interfacial exchange coupling to be relatively strong with a perpendicular orientation between the ferro/antiferromagnetic axis directions, similar to the classic 'spin-flop' state in bulk antiferromagnets.

N. C. Koon, [92]

4.1 Introduction

In the previous chapter, we have noted that the theoretical predicted bias field is often a magnitude too large when comparing to experimental data. To explain this discrepancy, the concept of rotatable spins was introduced in the advanced Meiklejohn and Bean model, as was defined in section 3.2. If only a fraction f of the uncompensated AFM spins is frozen, then the bias field is reduced approximately with a factor $1 - f$. The rotatable spins lead to an enhancement of the coercivity and training effects.

Considering the spin structure of CoO (figure 2.3) however, it is clear that also compensated planes, e.g. the (001) plane, are present. As a compensated AFM interface has no net magnetic moment to which the ferromagnet can couple, one could assume that this interface interaction is of little or no importance. As is often the case in nature however, things are more complicated than they seem.

In section 2.1, we have shown that when an external field is applied perpendicular to the anisotropy axis of an antiferromagnet (figure 2.1), the 2 sublattices will cant towards the magnetic field. One could suspect that a similar effect will happen when coupling a ferromagnet to a compensated antiferromagnetic interface as both AFM sublattices will try to minimize their surface energy density. This second order interaction[93], also called spin flop coupling, induces a perpendicular coupling between the FM and the AFM and has experimentally been verified[49, 94, 95]. An example[49] of the presence of this spin flop coupling in a $\text{La}_{0.7}\text{Sr}_{0.3}\text{MnO}_3/\text{LaFeO}_3$ bilayer¹ is shown in figure 4.1.

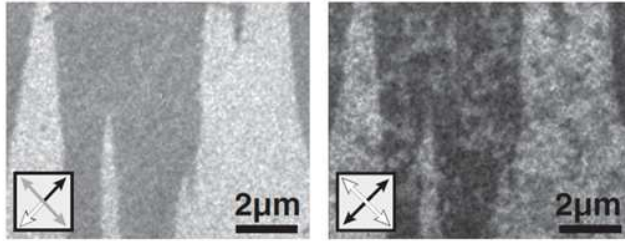


Figure 4.1: X-PEEM data of spin flop coupling in a LSMO/LFO bilayer at a temperature $T < T_C, T_N$. Left: ferromagnetic LSMO. The arrows indicate the direction of the FM magnetisation vector. Black is not present in the figure. Right: Antiferromagnetic LFO. The inset shows the axes along which the AFM spins are aligned. The image clearly shows a perpendicular coupling between the ferromagnet and the antiferromagnet. Note that both layers have a biaxial anisotropy in this case. Reproduced from [49].

As this canting is a reversible transition for the AFM and is symmetric in the case of positive as well as negative saturation of the ferromagnet, this interaction does not induce exchange bias, but leads to an enhanced coercivity. According to the model of Stiles and McMichael[96], spin flop coupling can be implemented in micromagnetic simulations[97] by introducing a biquadratic energy density term of the form

$$\epsilon_{\text{sf}} = K_{\text{sf}} (\mathbf{m}_{\text{FM}} \cdot \mathbf{n}_{\text{AFM}})^2 \quad (4.1)$$

¹We will abbreviate $\text{La}_{0.7}\text{Sr}_{0.3}\text{MnO}_3$ as LSMO and LaFeO_3 as LFO.

where \mathbf{n}_{AFM} is a unit vector, pointing along the Néel axis of the antiferromagnet at the interface. This energy term is minimal if the ferromagnet is oriented perpendicular to the AFM. It cannot explain any training effects in compensated antiferromagnetic interfaces however.

Although thus the origin of this spin flop coupling is pretty well understood, there are still a lot of questions unanswered, e.g. how can we relate this increase of coercivity to fundamental parameters and how and when can compensated AFM spins produce training effects?

In this chapter, we will explain how we can model spin flop coupling as well as training effects for a compensated AFM interface using MuMax³. In the next section, we will first consider a simple model of an AFM with a strong uniaxial anisotropy and show that for small canting angles spin flop coupling indeed induces a perpendicular anisotropy axis as given in 4.1.

4.2 Approximated solution for compensated AFM spins

We will consider an infinite in-plane magnetised FM film (with thickness t_{FM} and saturation magnetisation M_{FM}) coupled to a compensated antiferromagnet. Analogous to the case of an uncompensated AFM interface (sections 3.2 and 3.3), we will follow the macrospin approach and so the magnetic system can be characterized by defining the relevant angles. Labeling β and γ as, respectively, the angles which the FM and the external field H_{ext} make with the AFM anisotropy axis, we can write the total surface energy density σ of this system as

$$\sigma = -\mu_0 M_{\text{FM}} t_{\text{FM}} H_{\text{ext}} \cos(\gamma - \beta) + \varepsilon_{\text{K}}(\beta) t_{\text{FM}} + \sigma_{\text{AFM}}(\beta, \phi, \theta) \quad (4.2)$$

where the function $\varepsilon_{\text{K}}(\beta)$ represents the anisotropy energy density of the ferromagnet. If we assume, for simplicity, that the FM has a uniaxial anisotropy perpendicular to the Néel axis of the AFM, $\varepsilon_{\text{K}}(\beta)$ is given by

$$\varepsilon_{\text{K}}(\beta) = K_{\text{FM}} \cos^2(\beta) \quad (4.3)$$

The function $\sigma_{\text{AFM}}(\beta, \phi, \theta)$ in equation 4.2 describes the interaction of the AFM (total thickness t_{AFM}) with the FM and the internal interaction between the 2 AFM sublattices and is given by

$$\begin{aligned}
\sigma_{\text{AFM}}(\beta, \phi, \theta) = & -J_{\text{I}} \cos(\beta - \theta) + J_{\text{I}} \cos(\beta + \phi) \\
& -K_{\text{AFM}} t_{\text{AFM}} [\cos^2(\theta) + \cos^2(\phi)] \\
& -\delta t_{\text{AFM}} \cos(\theta + \phi)
\end{aligned} \tag{4.4}$$

where we have defined J_{I} as the coupling constant (surface energy density) between the FM and an AFM macrospin analogous to the Meiklejohn and Bean model, K_{AFM} the anisotropy constant of a sublattice and δ the energy density linked to the mutual interaction between the 2 AFM sublattices. The definition of the angles ϕ and θ , which the 2 AFM macrospins make with respect to their anisotropy axis, is shown in figure 4.2.

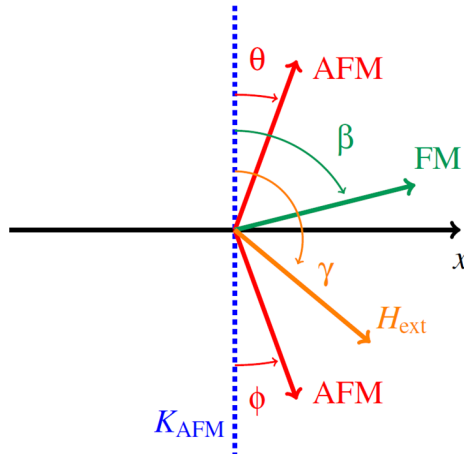


Figure 4.2: Definition of the AFM canting angles θ and ϕ , the FM angle β and the angle γ of the external field H_{ext} with respect to the AFM uniaxial anisotropy axis K_{AFM} .

As only the term σ_{AFM} in σ depends on the angles ϕ and θ , it suffices to calculate the derivatives of σ_{AFM} towards ϕ and θ in order to minimize the total energy of the AFM. This leads to equations for θ and ϕ as a function of the angle β .

Assuming small canting angles, we can expand the function σ_{AFM} up to second order in θ and ϕ , analogous to what we did in section 3.3 while discussing the approximated solution for the bias field, induced by uncompensated AFM spins.

$$\begin{aligned}
\sigma_{\text{AFM}} \approx & -J_{\text{I}} \left[\left(1 - \frac{\theta^2}{2} \right) \cos(\beta) + \theta \sin(\beta) \right] \\
& + J_{\text{I}} \left[\left(1 - \frac{\phi^2}{2} \right) \cos(\beta) - \phi \sin(\beta) \right] \\
& + K_{\text{AFM}} t_{\text{AFM}} (\theta^2 + \phi^2) + \frac{\delta t_{\text{AFM}}}{2} (\theta + \phi)^2 \quad (4.5)
\end{aligned}$$

leaving out constant energy terms. Minimizing this energy density by calculating $\frac{\partial \sigma_{\text{AFM}}}{\partial \theta}$ and $\frac{\partial \sigma_{\text{AFM}}}{\partial \phi}$, we find after the elimination of θ^* from the ϕ^* equation (and vice versa) an expression for θ^* and ϕ^* as a function of the ferromagnetic angle β

$$\theta^*(\beta) = \frac{J_{\text{I}} \sin(\beta) [-J_{\text{I}} \cos(\beta) + 2K_{\text{AFM}} t_{\text{AFM}}]}{4t_{\text{AFM}}^2 K_{\text{AFM}} (K_{\text{AFM}} + \delta) - J_{\text{I}}^2 \cos^2(\beta)} \quad (4.6)$$

$$\phi^*(\beta) = \frac{J_{\text{I}} \sin(\beta) [J_{\text{I}} \cos(\beta) + 2K_{\text{AFM}} t_{\text{AFM}}]}{4t_{\text{AFM}}^2 K_{\text{AFM}} (K_{\text{AFM}} + \delta) - J_{\text{I}}^2 \cos^2(\beta)} \quad (4.7)$$

These 2 equations show that for $\beta = \frac{\pi}{2}$ the angles of the AFM macrospins are symmetrical around the FM direction β , i.e. $\theta^* = \phi^*$. After substituting these angles $\theta^*(\beta)$ and $\phi^*(\beta)$, which minimize the AFM energy density σ_{AFM} , in equation 4.5, we find that

$$\sigma_{\text{AFM}}(\beta) \approx -\frac{\alpha \sin^2(\beta)}{1 - \frac{\alpha \cos^2(\beta)}{2t_{\text{AFM}} K_{\text{AFM}}}} \quad (4.8)$$

where we have defined the constant $\alpha = \frac{J_{\text{I}}^2}{2t_{\text{AFM}}(K_{\text{AFM}} + \delta)}$. Retaining only the lowest order approximation in $\frac{\alpha}{2t_{\text{AFM}} K_{\text{AFM}}}$ in the case of low coupling between the FM and the AFM, one finally obtains that

$$\sigma_{\text{AFM}}(\beta) \approx \alpha \cos^2(\beta) \quad (4.9)$$

This expression shows that equation 4.1 is in fact the low coupling approximation of the exact energy terms and describes spin flop coupling for small canting angles, i.e. the energy of the antiferromagnet is minimal when the ferromagnet is oriented perpendicular ($\beta^* = \frac{\pi}{2}$) to the AFM Néel vector. In this case, the AFM canting angles are given by

$$\theta^* = \phi^* = \frac{J_{\text{I}}}{2t_{\text{AFM}}(K_{\text{AFM}} + \delta)} \quad (4.10)$$

The total *effective* surface energy density can then be written as

$$\sigma_{\text{eff}} = -\mu_0 M_{\text{FM}} t_{\text{FM}} H_{\text{ext}} \cos(\gamma - \beta) + (K_{\text{FM}} t_{\text{FM}} + \alpha) \cos^2(\beta) \quad (4.11)$$

and the switching field B_c for $\gamma = \frac{\pi}{2}$ is given by

$$B_c = \frac{2}{M_{\text{FM}}} \left[K_{\text{FM}} + \frac{J_1^2}{2t_{\text{AFM}} t_{\text{FM}} (K_{\text{AFM}} + \delta)} \right] \quad (4.12)$$

in analogy to the anisotropy field in the Stoner Wohlfarth model (section 1.6). This shows that spin flop coupling leads to an enhanced coercivity[58] for a hysteresis loop measured perpendicular to the Néel vector of the AFM and only leads to a renormalization of the uniaxial anisotropy constant K_{FM} .

Given the parameters J_1 , K_{AFM} and δ , one can implement spin flop coupling in MuMax³ by adding a custom energy density ϵ_{sf} and a corresponding effective field B_{sf} term, defined as

$$\epsilon_{\text{sf}} := -\frac{1}{2} M_{\text{FM}} \cdot \mathbf{B}_{\text{sf}} = \frac{\alpha}{t_{\text{FM}}} \cos^2(\beta) \quad (4.13)$$

$$\mathbf{B}_{\text{sf}} = -\frac{2\alpha}{M_{\text{FM}} t_{\text{FM}}} (\mathbf{u} \cdot \mathbf{m}_{\text{FM}}) \mathbf{u} \quad (4.14)$$

with \mathbf{m}_{FM} the normalized magnetisation vector of the FM and \mathbf{u} the uniaxial anisotropy axis of the AFM. As expected, this spin flop model does not produce exchange bias. In case the 2 AFM macrospins couple with different strengths towards the FM, one can approximate the exact energy terms again for small canting angles (see Appendix H) and show that this in fact leads to exchange bias as a first order effect, given by $\sigma_{\text{AFM}}(\beta) = -[J_{1,\theta} - J_{1,\phi}] \cos(\beta)$ while neglecting higher order corrections.

4.3 Implementation of compensated AFM interfaces

Although the implementation of spin flop coupling as an induced uniaxial anisotropy is very efficient because only the ferromagnet needs to be taken into account, it has several drawbacks, e.g. these approximations are not valid anymore for strong coupling parameters J_1 and training effects cannot be taken into account, analogous to what was explained in section 3.3 for the approximated solution of uncompensated AFM spins. We will now explain how we can provide a full micromagnetic description of compensated antiferromagnetic interfaces in MuMax³.

4.3.1 Full micromagnetic description of spin flop coupling

In a micromagnetic approach, the atomic magnetic moments and their quantum mechanical interactions are averaged out over a larger length scale (order nanometers), but still small enough to resolve magnetic structures such as domain walls. This approach has been used for many years to model ferromagnets, where the exchange interaction does not allow for sharp changes in the magnetisation. In an antiferromagnet, where the magnetic moments alternate direction on consecutive atomic sites, this approach would result in a zero net magnetisation. However, at the micromagnetic scale, the two atomic sublattices of an AFM can be considered as two separate, smoothly varying ferromagnetically ordered lattices that are antiferromagnetically coupled and coincide in space.

Disregarding the atomic scale of these sublattices means that all the dynamics that play on this length scale (e.g. AFM spin waves) are lost, just like the high frequency part of the spin wave spectrum is also lost in a FM model when the local variations are averaged out. However, the static interaction between the 2 sublattices is not lost as the exchange interaction between the sublattices is included in the micromagnetic model.

For interfaces with thin FM and AFM layers, single micromagnetic layers can be used. As a micromagnetic cell can only contain one magnetisation vector in MuMax³, the coinciding cells of an AFM layer are separated into 2 different layers, which we will denote AFM₁ and AFM₂ (see figure 4.3). This separation in space has no physical implications. Even though the AFM₁ layer (figure 4.3) is not directly adjacent to the FM layer, a direct coupling can be established by adding a custom field and energy term (see Appendix C). A negative interlayer exchange stiffness A_{AFM} will ensure the antiferromagnetic coupling of the sublattices and a positive intralayer exchange stiffness A_{A} of the same magnitude will allow for the correct domain wall energy in the AFM (see Appendix C).

4.3.2 Limitations of our model

Due to this micromagnetic approximation of an AFM and its implementation in MuMax³, no high frequency dynamics due to the exchange interaction between the 2 AFM sublattices can be modelled in our simulations.

Thus, one should only use the `minimize()` or `relax()` function when modelling antiferromagnetic interfaces. When studying quasistatic configurations which are the result of an energy minimisation, precession does not need to be taken into account. This is the case for the problems studied in this thesis: exchange bias, spin flop coupling and athermal training.

In case of a thick antiferromagnet, one can expect that the AFM spins in the bulk will be pinned along the anisotropy axis and only the AFM spins at the interface region will be canted towards the ferromagnet. As introduced in the model of Mauri[21], a planar domain wall can be included by adding a third fixed layer² to the simulation box or by subdividing the AFM into several bilayers.

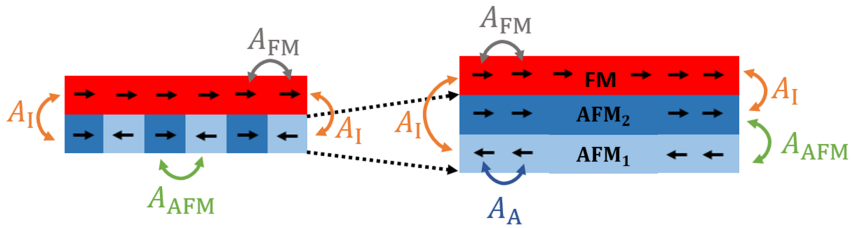


Figure 4.3: In our micromagnetic model, an atomic compensated AFM interface is replaced by 2 continuous AFM layers (blue). The FM (red) and AFM₁ layer can be coupled either by using periodic boundary conditions or by defining a custom field/energy term, see Appendix C. The AFM₂ layer is coupled to the FM by rescaling the exchange field and similar for the coupling between AFM₁ and AFM₂.

4.3.3 Implementation

As discussed, each AFM layer can be modelled as a pseudo-ferromagnetic layer with thickness t_{AFM} and sublattice anisotropy constant K_{AFM} . The interfacial exchange energy J_I and the energy density δ , linked to the mutual interaction between the 2 sublattices, can be defined in terms of exchange stiffnesses between the FM/AFM and the 2 AFM layers respectively, analogous to what was derived in section 3.4 for uncompensated spins.

²For this case one has to add an energy term $-J_a \cos(\phi) - J_a \cos(\theta)$ in the macrospin model (equation 4.4). The parameter J_a is the surface energy density to form a planar domain wall in the antiferromagnet.

Using the MuMax³ convention for the exchange energy density, one obtains that $A_I = \frac{J_1 C_z}{2}$ and $A_{AFM} = -\frac{\delta_{AFM} C_z}{2}$ with C_z the cell size perpendicular to the interface and A_{AFM} the intersublattice exchange stiffness. Taking into account only nearest neighbour interaction in the atomic description of an AFM, one can proof (Appendix C) that one has to set the intralayer exchange stiffness $A_A = |A_{AFM}|$ in our micromagnetic model to obtain the correct domain wall energy in the AFM.

Assuming that a micromagnetic system consists of 2 AFM sublattices + 1 FM layer, one can couple the FM layer with the nearest AFM layer (AFM₂ in figure 4.3) by rescaling the exchange stiffness using the scaling factor S , as given in equation 3.24 with $M_{FM} = M_{AFM}$. As in MuMax³ only nearest neighbouring cells are taken into account for the evaluation of the exchange energy, one has to couple the other AFM layer, labeled by AFM₁ in figure 4.3, with the FM layer by using periodic boundary conditions, perpendicular to the FM/AFM interface or by defining a custom field / energy term. The former approach can only be used however if the FM consists of 1 layer while the addition of a custom field / energy term is generally applicable.

Demagnetisation energy should be turned off in the AFM layers, as was the case in the implementation of an uncompensated AFM interface. For the practical implementation and an example of the code, see Appendix C.

It is also important to note that one can take into account compensated as well as uncompensated (rotatable as well as pinned) AFM spins in the same micromagnetic simulation. To model the compensated spins, the AFM is divided into 2 layers, each with a thickness equal to the total thickness of the AFM. To implement the uncompensated spins, it is sufficient to locally couple only 1 AFM layer to the FM layer (coupling constant J_1 and *total* anisotropy constant K_{AFM} as defined in section 3.2) or couple both AFM layers to the FM layer with an interface coupling $\frac{J_1}{2}$ as otherwise the exchange bias field due to the pinned uncompensated spins will be twice as high compared to the Meiklejohn and Bean model (section 3.2). In the latter case, K_{AFM} represents the sublattice anisotropy constant and the AFM layers should (locally) be decoupled from each other, i.e. $\delta = 0$. So in summary, one can conclude that one is able to model a mixed compensated and uncompensated AFM interface using MuMax³.

4.4 Testing the micromagnetic model

To compare the coercivity B_c derived from the small angle approximation (equation 4.12) with the coercivity when the exact energy terms are taken into account, a simple system was studied with $t_{\text{AFM}} = t_{\text{FM}} = 3$ nm, $M_{\text{FM}} = 1400$ kA/m, $\delta = 1 \times 10^6$ J/m³ and $K_{\text{AFM}} = 7 \times 10^5$ J/m³. Demagnetisation energy was turned off in the FM (macrospin approach) and the anisotropy in the FM layer was neglected. To avoid metastable states, 2 consecutive hysteresis loops were simulated each time for H_{ext} parallel³ and perpendicular to the uniaxial anisotropy axis of the AFM.

The coercivity of the second hysteresis loop is shown in figure 4.4, together with the small angle approximation, as defined by equation 4.12. One can see that, for these parameters, the small angle approximation of our model is valid up to $J_1 \approx 2$ mJ/m² where the relative error is around 5%.

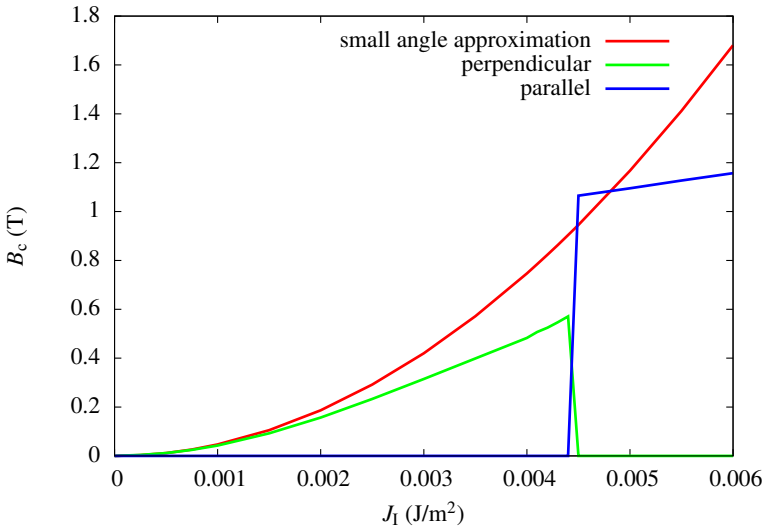


Figure 4.4: Coercivity B_c as a function of the coupling constant J_1 . The small canting angle approximation (red curve) is valid up to $J_1 \approx 2$ mJ/m². The breakdown of the canted spin flop state happens around $J_1 \approx 4.5$ mJ/m² and leads to a vanishing coercivity for a hysteresis loop measured perpendicular (green curve) to the Néel vector of the antiferromagnet.

³In fact, H_{ext} is set at a small angle of 1° with the defined directions to introduce a slight asymmetry. A small deviation from a stable energy minimum has a minimal effect.

In figure 4.5, the minimized total surface energy density (without Zeeman) of the system for different coupling constants J_1 is shown, while rotating the FM angle β . For low J_1 , the minima are at the angles $\beta = \pm \frac{\pi}{2}$ which represent the global energy minima. This corresponds to what was discussed in the small canting angle approximation, as can be seen in equation 4.13. Even though the approximation is not valid anymore around $J_1 \approx 2 \text{ mJ/m}^2$, the spin flop state is still the global energy minimum and will lead to a vanishing coercivity for a hysteresis loop, measured parallel to the Néel vector, i.e. along one of the AFM easy axes, as can be seen in figure 4.4.

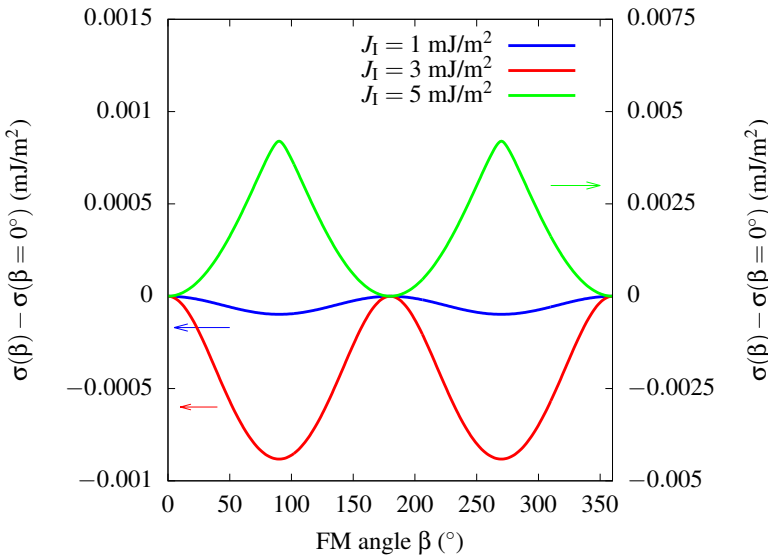


Figure 4.5: Minimal surface energy density curves σ as a function of the FM rotation angle β . A spin flip transition happens for $J_1 \approx 4.5 \text{ mJ/m}^2$ which leads to the fact that the spin flop state is not the global energy minimum anymore. Each curve was shifted by $\sigma(\beta = 0^\circ)$. The values of the curve for $J_1 = 5 \text{ mJ/m}^2$ correspond to the scale on the right.

At $J_1 \approx 4.5 \text{ mJ/m}^2$ however, the shape of the energy function changes because the canted spin flop state is not the global energy minimum anymore as a spin flip transition occurs, analogous to the metamagnetic spin flip transition of an antiferromagnet in a strong magnetic field, which was mentioned in section 2.1. In this case the interface coupling J_1 overcomes

the intersublattice interaction δ resulting in a parallel⁴ orientation of the 2 AFM layers. Due to the strong magnetocrystalline anisotropy of the AFM, the global energy minima are now given by $\beta = 0$ and π , i.e. parallel to the easy axes of the AFM, and the direction perpendicular to the Néel vector becomes a hard axis. This leads to a finite coercivity in the hysteresis loop parallel to the Néel vector in figure 4.4 and a vanishing coercivity at $J_1 \approx 4.5 \text{ mJ/m}^2$ for the perpendicular hysteresis loop.

⁴For small canting angles with respect to the AFM anisotropy axis, one can proof (Appendix G) that the 2 AFM macrospins have to be parallel if they are oriented in the same anisotropy direction, as can be expected due to the symmetry of the system.

4.5 Example: Spin flop coupling in LSMO/LFO square nanostructures

4.5.1 Introduction

As a first demonstration of our micromagnetic model for spin flop coupling, we will reproduce experimental X-PEEM data⁵ of epitaxial grown $\text{La}_{0.7}\text{Sr}_{0.3}\text{MnO}_3(35\text{nm})/\text{LaFeO}_3(3.8\text{nm})$ square nanostructures as has been reported by Takamura[98]. They noticed that in a full bilayer (see figure 4.1), the Néel vector of the compensated antiferromagnetic LFO was oriented perpendicular⁶ to the domain structure in the ferromagnetic LSMO layer, in accordance with spin flop coupling between a ferromagnet and compensated antiferromagnet.

In the $2\ \mu\text{m}$ LSMO/LFO squares, two types of FM domain structures could be observed, as has been displayed in figure 4.6 (d). The authors argued that they result from variations in the local bias field, induced by the DMI interaction similar to what was discussed in section 2.3.5. For low bias fields, the usual Landau structure (with a displaced vortex) is found and for higher local bias fields a z-type domain. A corresponding perpendicular domain structure was found in the AFM. For a single uncoupled LSMO square (figure 4.6 (c)) only the typical Landau domain structure was observed. This implicates that variations in the local bias field B_b can change the domain structure of the LSMO layer and thus also of the AFM. Remark that the average macroscopic bias field vanished, but not on the micrometer scale of the FM squares and that no external field was applied during cooling.

4.5.2 Micromagnetic model

The ferromagnetic LSMO has biaxial anisotropy with easy axes oriented along the crystallographic $\langle 110 \rangle$ directions, i.e. along the sides of the $2 \times 2\ \mu\text{m}^2$ squares. The anisotropy energy density (see figure 1.6) is given by $\epsilon_K = K_c(\mathbf{c}_1 \cdot \mathbf{m})^2(\mathbf{c}_2 \cdot \mathbf{m})^2$ with \mathbf{m} the normalized magnetisation, \mathbf{c}_1 along

⁵X-ray photoemission electron microscopy uses the difference in absorption rate between left and right circularly polarized light (XMCD) for a ferromagnet or the difference between parallel and perpendicular linear polarized light (XMLD) with respect to the magnetisation axis of an antiferromagnet. XMCD gives directional information (parallel or antiparallel) and XMLD gives axial information (parallel or perpendicular).

⁶Remark that this is not always the case. Sometimes a parallel orientation is found. In this case spin flop coupling is facilitated by the biaxial anisotropy of both layers.

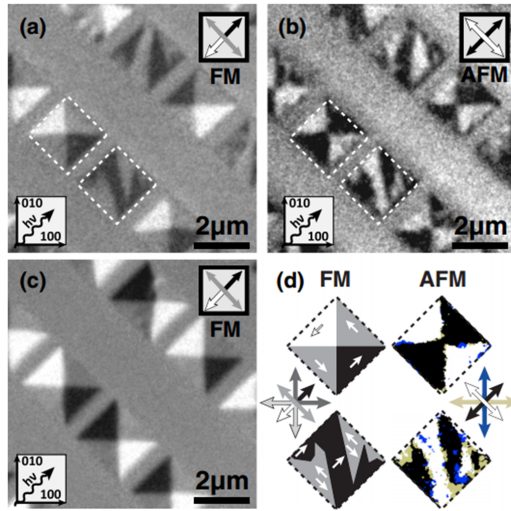


Figure 4.6: X-PEEM data of the LSMO/LFO nanosquares. Figure (a): Landau domains and z-domains in the LSMO squares with perpendicular coupled domain structures in the antiferromagnetic LFO (figure b). Figure (c): only Landau domain structures can be found when the LSMO is not coupled to the LFO layer. Figure (d): schematical representation of the 2 domain configurations found in (a). Reproduced from [98].

the x -axis and c_2 along the y -axis of our simulation box. The bilayer was divided into $512 \times 512 \times (2 \text{ AFM} + 1 \text{ FM})$ cells with a lateral cell size of 3.9 nm and thickness⁷ of 35 nm. For the ferromagnetic LSMO, we used typical parameters[98]: $M_{\text{FM}} = 400 \text{ kA/m}$, $A_{\text{FM}} = 1.8 \text{ pJ/m}$ and $K_{\text{c,FM}} = 1.6 \text{ kJ/m}^3$.

As experiments[98, 99] show that in the LFO layer 60 % of the AFM domains have their biaxial easy axes along the $\langle 110 \rangle$ directions and 40 % their easy axes along the $\langle 100 \rangle$ directions, the anisotropy axes were distributed accordingly for the AFM layer by using a Voronoi tessellation⁸. As parameters for the AFM, we used: $\delta = 1.25 \times 10^5 \text{ J/m}^3$, $K_{\text{c,AFM}} = 1.5 \text{ kJ/m}^3$ and for the interaction between the AFM and FM that $J_1 = 0.17 \text{ mJ/m}^2$.

⁷For a rescaling of the AFM parameters to achieve the correct energy, see Appendix C.

⁸It is clear that in an AFM grain the direction of the anisotropy axis, etc. should be set the same in the 2 AFM layers as they represent the 2 AFM sublattices.

4.5.3 Results

Starting from a random state in the FM and semi-random⁹ in the AFM, the system was relaxed towards equilibrium after the application of some thermal fluctuations (70 K during 0.2 μ s). The FM and the sum of the absolute value of the magnetisation of the 2 AFM layers (at remanence) are shown in figure 4.7. In this case, it is the AFM who orients itself perpendicular to the FM as the ferromagnetic domain structure is strongly determined by the demagnetisation energy. A similar effect was also observed in NiO/Fe and CoO/Fe nanodisks.[100]

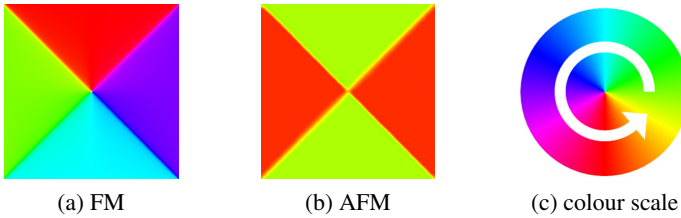


Figure 4.7: Spin flop coupling in a LSMO/LFO nanosquare for $B_b = 0$ mT, initialized from a random state. Figure (a): typical Landau domain structure in the ferromagnetic LSMO. Figure (b): sum of the absolute values of the magnetisation of the 2 antiferromagnetic LFO layers. In figure (c), the colour scale of the magnetisation is shown. The magnetisation vector is tangent to a circle.

In the experimental data, shown in figure 4.6 (a), also z-domains were found in the FM and corresponding perpendicularly coupled domains in the AFM. The authors state, by comparing the data to a micromagnetic simulation of only the FM layer, that these domain structures appear for bias fields above a threshold of approximately 9 mT and correspond to a vortex that is displaced towards the corner of a square. To test this hypothesis, a field sweep of the FM/compensated AFM square was performed with an external field, representing the bias field B_b , applied along one of the diagonals of the square. Starting from remanence, as shown in figure 4.7, it appears that the flux closed vortex state is stable for $B_b < 8$ mT.

⁹30% of the AFM grains were initialised along the x -axis, 30% along the y -axis, 20% along one diagonal of the square and 20% along the other diagonal. The sublattices were initialised each time antiparallel to each other.

For a bias field of 8 mT, the vortex gets displaced towards the corner of the square and for $B_b > 8$ mT z-domains¹⁰ are formed in the FM and a corresponding perpendicular domain structure in the AFM layers. These 3 magnetic configurations are shown in figure 4.8. Note that the domain wall in the AFM is induced by the initial Landau state.

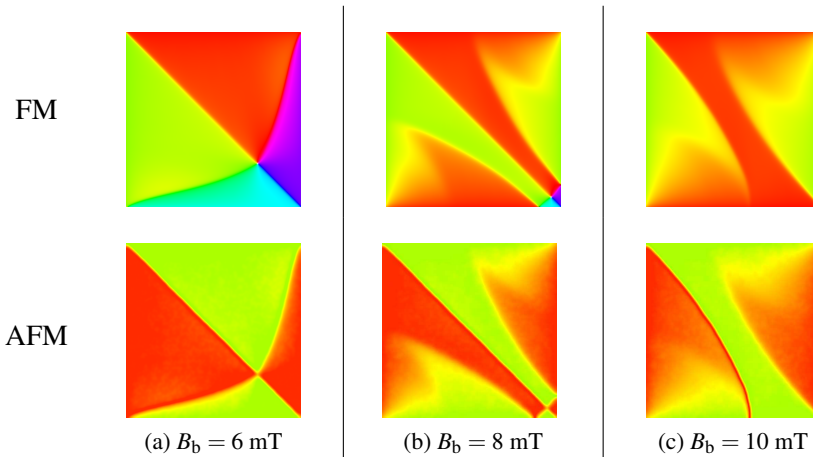


Figure 4.8: Magnetic configurations in the LSMO/LFO square for different bias fields B_b . (a): Landau state for $B_b = 6$ mT. (b): vortex displaced towards the corner for $B_b = 8$ mT. (c): z-domain for $B_b = 10$ mT. Top row represents the FM layer and bottom row represents the corresponding AFM domain structure. Each time the sum of the absolute value of the magnetisation of the 2 AFM layers is shown.

When returning from saturation however, the FM does not return towards the vortex state for $0 < B_b < 8$ mT. The supposition thus arises that these z-domains can also be stable in lower bias fields, as opposed to what was stated by the authors in [98]. Furthermore, it is clear that the z-state as measured in figure 4.6(d) should be associated with figure 4.8c rather than figure 4.8b. The FM square in their micromagnetic simulation (see figure 4 in [98]) was not saturated enough to achieve the complete z-domain in the ferromagnet¹¹.

¹⁰When the LSMO is not coupled to the LFO, no bias field can be present and thus only Landau states are formed in the ferromagnet.

¹¹Private communication with Erik Folven.

When initializing the ferromagnet from a completely random state¹², using different random seeds, only Landau domain structures were found for $B_b = 0$ mT. Relaxing different random states in a bias field $B_b = 5$ mT, z-domains as well as domains with a displaced vortex were formed. The result is shown in figure 4.9. Remark that also another variant of the z-domain can be found due to the symmetry of the system, if the bias field B_b is applied in the same direction, along the same diagonal axis. This is in correspondence to the experimental data, as shown in figure 4.6 (a). So in fact, one can obtain in total 8 equivalent FM z-domain configurations for 4 different bias field directions, as can be seen in figure 4.10. For the AFM as a whole, only 4 different states can be discerned due to the symmetry between the sublattices, because e.g. figures 4.10(a) and 4.10(c) are indistinguishable for the antiferromagnet.

The magnetic domain configuration 4.9a was stable in our simulations, even while applying thermal fluctuations for a longer simulation time of $2 \mu\text{s}$ and increasing temperature. It is not clear however if these states also appear in the experimental data as only a small part of the squares are shown. Due to the limited simulation time, it is possible that these states are thermally not stable when considering macroscopic measurement times. However, the experimental data shows that also metastable states are present, e.g. the uppermost nanosquare in figure 4.6(a), which is not in a complete Landau state.

For $B_b \geq 7.5$ mT, only z-domains were formed. This shows that the appearance of the z-domains are indeed intimately linked to the presence of a bias field, but they can be stable for lower bias fields. In case the bias field was applied along one of the sides of the LSMO/LFO square, no z-states were generated and only Landau domain structures were present, in case the FM layer was not in a saturated state.

¹²Each time 10 simulations were performed with a different random seed, for the same bias field B_b .

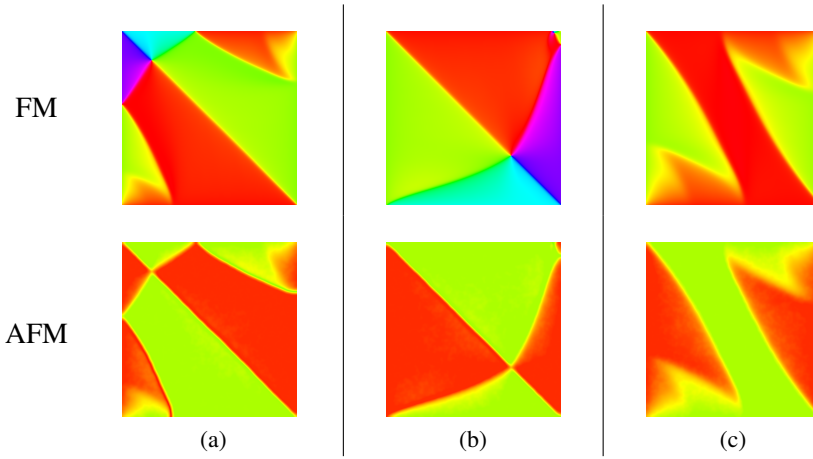


Figure 4.9: FM (top) and corresponding AFM (bottom) domain structures for $B_b = 5$ mT, started from a random configuration in the FM layer, initialized with different random seeds. For the AFM, each time the sum of the absolute value of the magnetisation of the 2 AFM layers is shown.

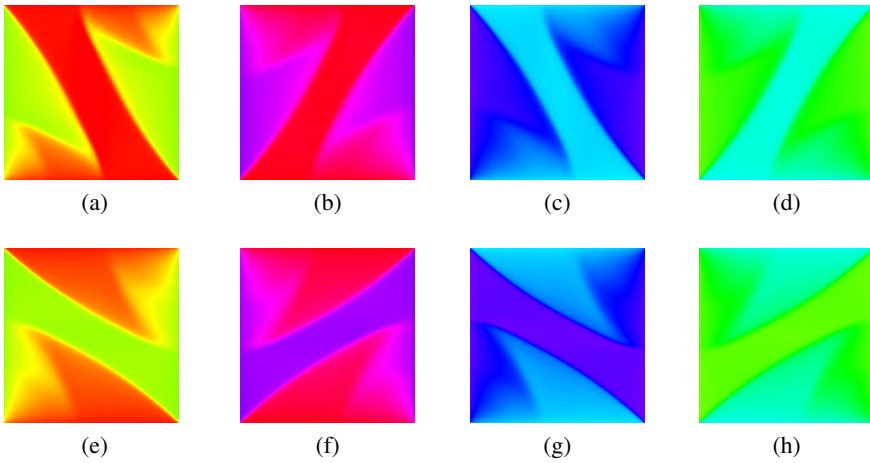


Figure 4.10: FM z-domains (top row) and corresponding symmetric FM domain states (bottom row) for $B_b = 7.5$ mT. Figures (a) and (e): B_b along $(1,1,0)$. Figures (b) and (f): B_b along $(1,-1,0)$. Figures (c) and (g): B_b along $(-1,-1,0)$. Figures (d) and (h): B_b along $(-1,1,0)$. In total, 8 equivalent FM states can be found. The corresponding AFM domains are not shown.

4.6 Example: Hoffmann training in a biaxial AFM

4.6.1 Introduction

As a second example, we will take a look at athermal training effects present at the interface of a compensated AFM, as was proposed by Hoffmann[101] and is nowadays generally accepted[102, 103]. While there can be no training or exchange bias in a perfectly compensated antiferromagnet with uniaxial anisotropy, Hoffmann argued that this is not the case when the AFM has a fourfold or higher magnetocrystalline anisotropy. After field cooling the sublattices of the AFM can be in a non collinear state and only relax towards an antiparallel configuration after the first reversal of the FM. This produces an athermal training effect and exchange bias in the first hysteresis loop ($n = 1$). Also the asymmetry between the descending branch in the first field loop and its reversal towards positive saturation is a prominent feature of athermal training, similar to what was found in the case of uncompensated AFM spins.

4.6.2 Micromagnetic model

As training in the model of Hoffmann results from a non collinear state of the 2 AFM sublattices, induced by field cooling, we can expect that the training effect will only happen within a certain parameter range. As an example, we will investigate this effect by considering a uniform biaxial compensated antiferromagnet whose easy axes make an angle of 45° with respect to the field cooling direction, here chosen to be the x direction (100) of our simulation box. To simulate field cooling, the AFM layers were initialized in a spin flop state, i.e. in the (1,1,0) and (1,-1,0) directions along their easy axes and are afterwards relaxed, while the FM was kept saturated in the field cooling direction.

A cell size of 2 nm was chosen for the in-plane direction and a cell thickness of 10 nm perpendicular to the interface, i.e. in this case $t_{\text{FM}} = t_{\text{AFM}} = 10$ nm. For the ferromagnet, typical parameters of Py were used: a saturation magnetisation $M_{\text{FM}} = 800$ kA/m and an exchange stiffness $A_{\text{FM}} = 13$ pJ/m. No FM magnetocrystalline anisotropy was considered. For the interaction strength between the 2 antiferromagnetic sublattices, as defined in equation 4.4, we used that $\delta = 8 \times 10^4$ J/m³.

The biaxial anisotropy constant $K_{c,AFM}$ of the antiferromagnet and the interfacial coupling parameter J_I between the FM and the AFM were varied and the coercivity and exchange bias field were determined for 2 consecutive hysteresis loops along the field cooling direction.¹³ The Zeeman energy was not taken into account for the AFM.

4.6.3 Results

The result of this parameter scan is shown in figure 4.11 where the difference in coercivity between the first and second hysteresis loop is displayed. Reduced dimensionless units were used, i.e.

$$j = \frac{J_I}{\delta t_{AFM}} \quad k = \frac{K_{c,AFM} t_{AFM}}{\delta t_{AFM}} \quad b_c = \frac{\mu_0 M_{FM} t_{FM} H_c}{\delta t_{AFM}}$$

for the interfacial coupling, sublattice anisotropy constant and coercivity respectively. The different reversal mechanisms, present in the phase diagram, are illustrated in figure 4.13 for a coupling constant $j = 1.75$.

One can clearly distinguish two regions with training in the phase diagram. The middle region is the real Hoffmann training (figure 4.13c) as explained in the previous subsection: the AFM layers change from a non collinear to an almost antiparallel arrangement after the first reversal ($n = 1$) of the ferromagnet towards negative saturation. After this irreversible transition, the AFM layers will induce spin flop coupling (see Appendix E) in the FM layer, but with an easy axis rotated over 45° with respect to the field cooling direction. According to the Stoner Wohlfarth model, they will also contribute to the coercivity in the second hysteresis loop, but its value will be reduced by a factor 2. The coercivity $b_{c,2}$ of the second hysteresis loop (after training) for $j = 1$ as a function of the reduced anisotropy constant k can be seen in figure 4.14. Hoffmann training is present from $k \approx 0.75$ to $k \approx 3.5$.

The rise in coercivity for $k < 0.75$ is due to the fact that both AFM layers are in an almost 90° canted position and switch together with the FM. For this configuration (figure 4.13a), an increasing anisotropy constant leads to an increasing coercivity, in contrast to the case of spin flop coupling.

¹³ H_{ext} is set at a small angle of 1° with the field cooling direction to introduce a slight asymmetry in our system.

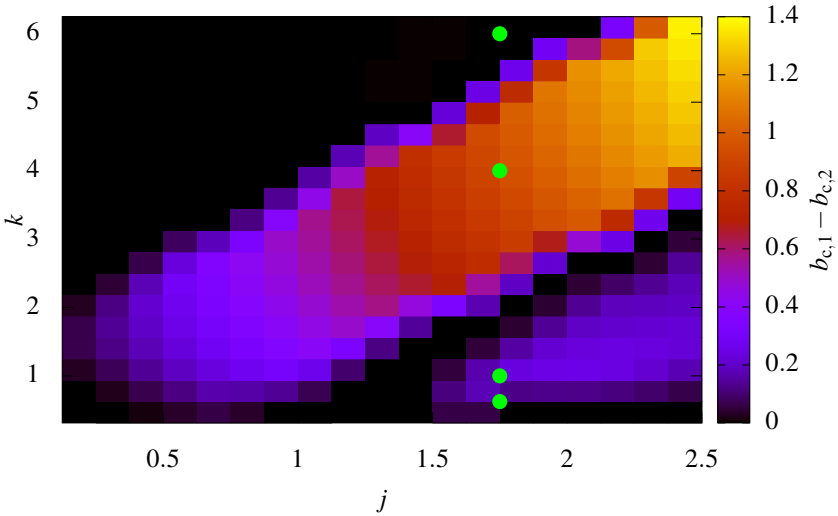


Figure 4.11: Phase diagram of Hoffmann training for a uniform biaxial antiferromagnet. Colour scale represents the difference in coercivity b_c (in reduced units) between the first and second hysteresis loop. The green dots indicate where the parameters of the sketches in figure 4.13 are situated.

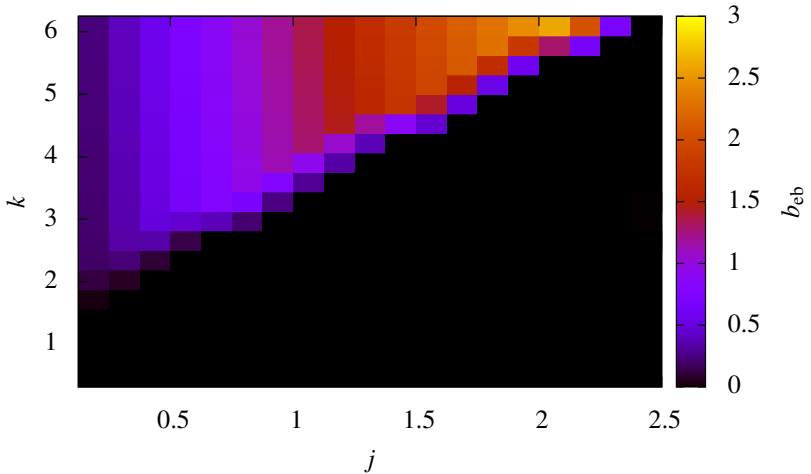


Figure 4.12: Regions in the phase diagram (for $n = 2$) which lead to permanent exchange bias due to pinned AFM spins.

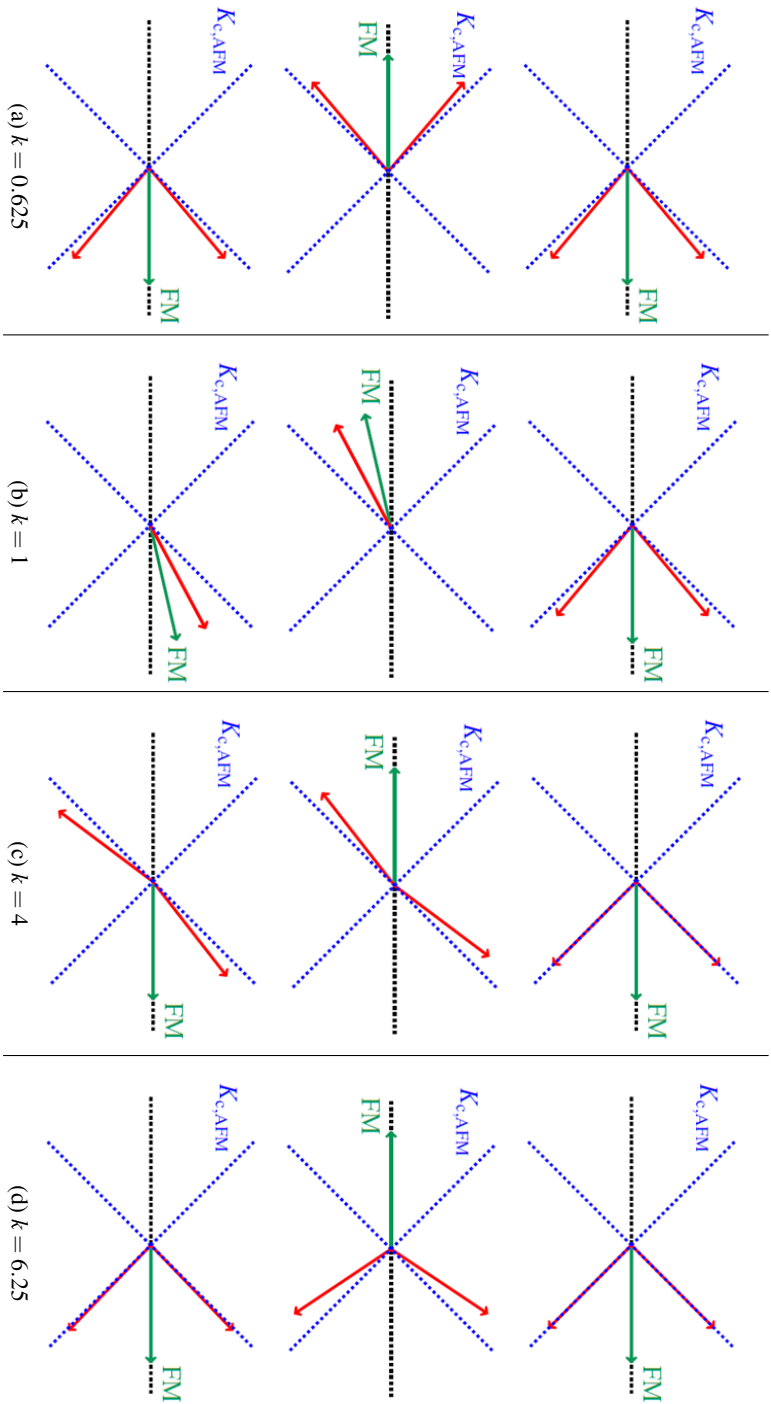


Figure 4.13: Each column represents a different region in the phase diagram (figure 4.11) for $j = 1.75$. Top row: relaxed field cooled state, middle row: at negative saturation, bottom row: at positive saturation again. Green arrow represents the FM, red arrows represent the 2 AFM layers. Figures (b) and (c) lead to an athermal training effect, while figure (d) leads to exchange bias.

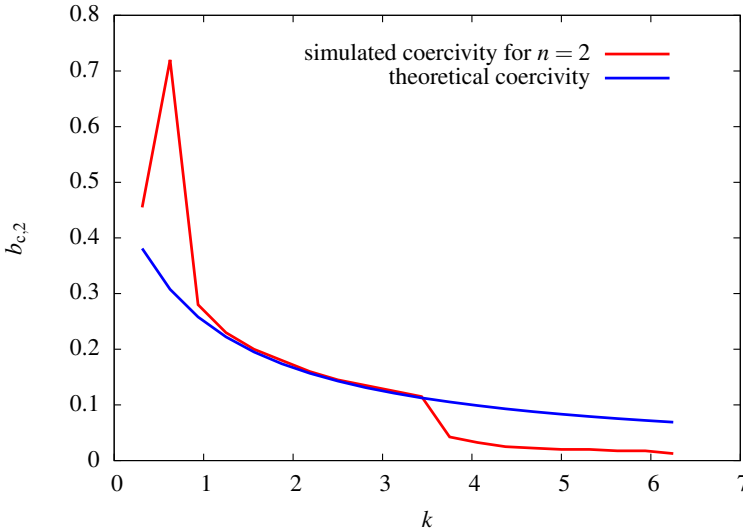


Figure 4.14: Comparison of the approximated theoretical coercivity b_c ($j = 1$) with the simulated coercivity, for $n = 2$. The theoretical curve (see Appendix E) matches with the simulated one, in case the 2 AFM layers stay in an antiparallel position for $n = 2$, thus from $k \approx 0.75$ to $k \approx 3.5$.

The training effect in the lower right part (region with high coupling and low anisotropy) of the phase diagram (figure 4.11) is the result of a spin flip transition. After reaching negative saturation in the first hysteresis loop, the two AFM layers stay parallel (see Appendix G) in further hysteresis loops. This mechanism is shown in figure 4.13b. A similar effect was already discussed when considering the breakdown of the canted spin flop state for an AFM with uniaxial anisotropy (section 4.4). In this case, the AFM layers switch irreversibly with the FM for $n > 1$, which leads to a higher coercivity. This is not the case in Hoffmann training. Both regions in the phase diagram however lead to an asymmetry in the first hysteresis loop which is typical for athermal training, as can be seen in figure 4.15.

Athermal training also leads to exchange bias in the first hysteresis loop after field cooling due to a change in coercivity. For high anisotropy constants k and low coupling constants j (upper left part of the phase diagram), one can in fact obtain exchange bias for $n \geq 1$ as the AFM spins are pinned in a canted state along the field cooling direction as is shown in figure 4.13d.

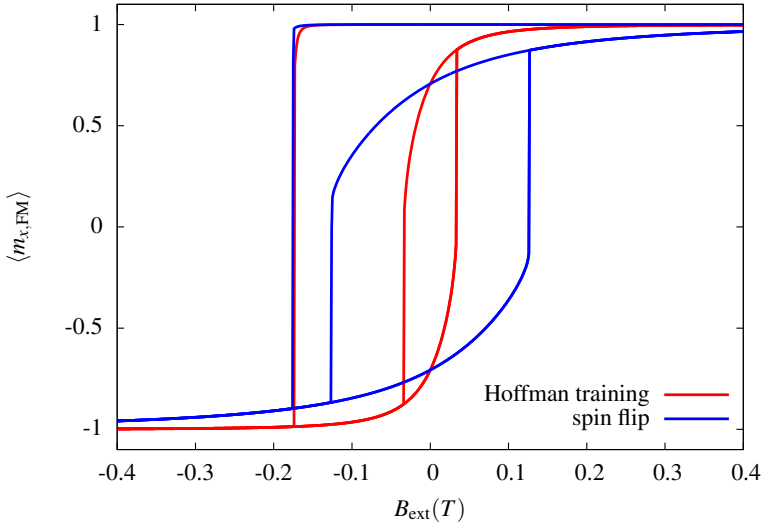


Figure 4.15: FM hysteresis loop, measured along the field cooling direction in the region of Hoffmann training ($j = 1.5$, $k = 2.5$) and in the region of a spin flip transition ($j = 2.25$, $k = 1.25$). In both cases the asymmetry and the training effect are clearly present.

The phase diagram for exchange bias in the case $n \geq 1$ is shown in figure 4.12. Using the small canting angle approximation in an AFM with biaxial anisotropy, one can calculate (see Appendix F) the bias field B_{eb} for high anisotropy constants. In figure 4.16, one can see that there is a good agreement between this model and the values obtained from our simulations. Also the bias field for 2 fixed uncompensated spins, which make an angle of 45° with the field cooling direction, is shown as comparison. We remark that in an experiment, one cannot distinguish between a frozen uncompensated AFM spin or 2 compensated biaxial AFM spins, frozen into a 90° canted state, as both have the same net effect on the FM layer.

If one assumes a negative coupling constant J_I and takes into account the Zeeman energy for the AFM during field cooling, one can also obtain positive bias fields, analogous to what was already discussed in section 3.7 for uncompensated AFM spins. For low cooling fields H_{cf} , the pinned compensated AFM spins will be oriented antiparallel to the cooling field direction. For stronger cooling fields however, the AFM spins can make

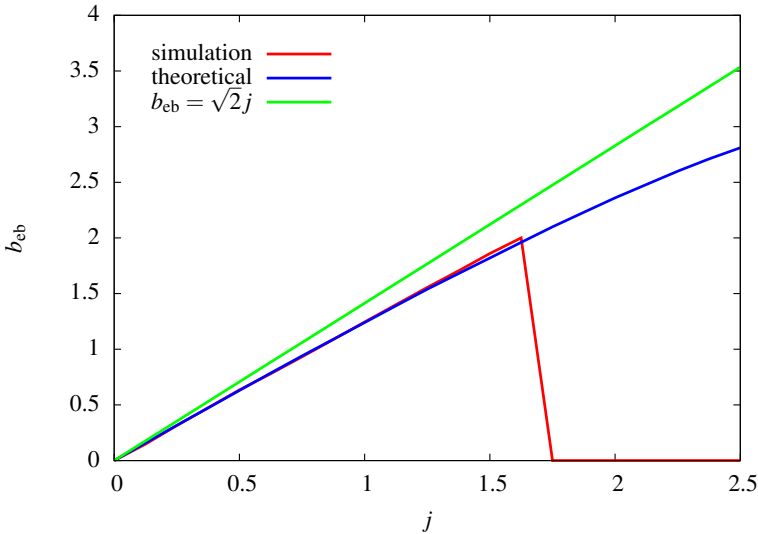


Figure 4.16: Comparison of the approximated theoretical bias field, as calculated in Appendix F, and the values obtained from our simulations ($n = 2$) for $k = 5$. The absolute value of the exchange bias field is shown.

an irreversible transition of 90° due to the Zeeman energy and produce a net magnetic moment parallel to H_{cf} . As field sweeps are often recorded for $H_{ext} \ll H_{fc}$, these spins stay pinned in the 90° canted state due to the strong magnetocrystalline anisotropy and low coupling to the FM, even during a reversal of the ferromagnet.

Additionally, a system with an in-plane polycrystalline biaxial AFM layer was simulated in the same parameter range as the uniform case. For each parameter set, the same grains with the same anisotropy axes were used. The AFM intergrain interaction was not taken into account. The difference in coercivity between the first and second hysteresis loop is shown in figure 4.17. Apart from small fluctuations, the global shape of the phase diagram is very similar to figure 4.11. The distinct separation between the region of Hoffmann training and the spin flip arrangement is less clear due to the random distribution of the anisotropy axes. The bias field in the second hysteresis loop ($n = 2$) is shown in figure 4.18 and is also similar to figure 4.12. In some regions, there is still a non vanishing bias field for $n \geq 2$.

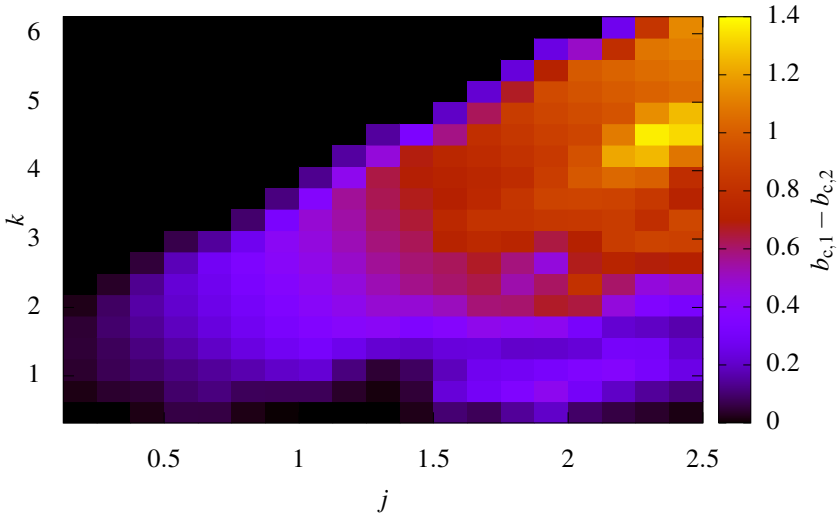


Figure 4.17: Phase diagram of Hoffman training for a polycrystalline biaxial antiferromagnet. Colour scale represents the difference in coercivity b_c (in reduced units) between the first and second hysteresis loop. The same parameters were used as in the uniform case, shown in figure 4.11.

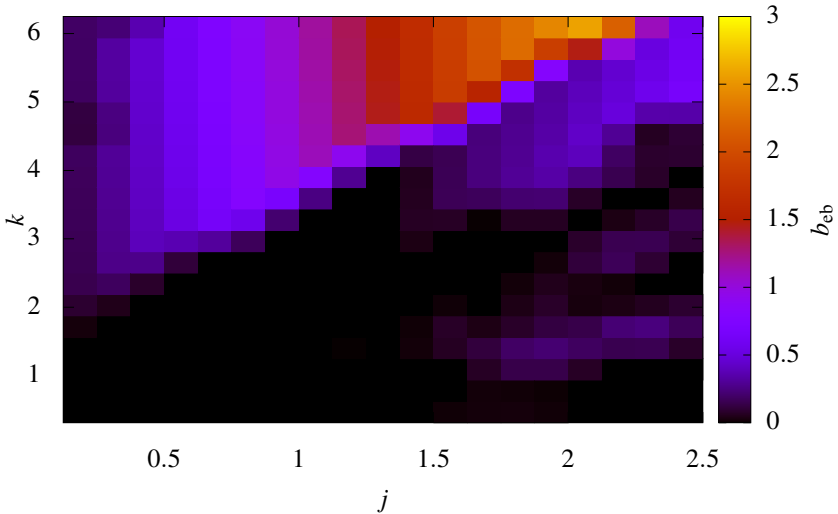


Figure 4.18: Exchange bias field ($n = 2$) in a polycrystalline AFM for grains with biaxial anisotropy. The same parameters were used as in the uniform case, shown in figure 4.12 .

The bias field in the region $j = 2, k = 4$ originates from the fact that some AFM sublattices, after being initialised at angle of 45° with respect to the field cooling direction, undergo a spin flip transition in the direction of the cooling field during the initial relaxation. Due to a high anisotropy, these AFM grains stay pinned during a reversal of the FM layer and thus induce exchange bias. The sum of the magnetisation vectors of the 2 AFM layers, defined as $\mathbf{m}_{\text{AFM}} = \mathbf{m}_{\text{AFM},1} + \mathbf{m}_{\text{AFM},2}$, is shown in figure 4.19 for the field cooled state, at negative saturation ($n = 1$) and at positive saturation ($n = 2$) of the ferromagnet. Although most AFM grains have undergone Hoffmann training after the first reversal of the FM (grey/blue coloured grains in figure 4.19b), some AFM grains have parallel sublattices, pointing in the field cooling direction (red coloured grains in figure 4.19b). A light blue and red colour can be seen in the grains with antiparallel sublattices at negative and positive saturation of the FM, respectively. The origin is a small canting of the AFM sublattices towards the ferromagnet, leading to a reversible net magnetic moment in the AFM in accordance to spin flop coupling.

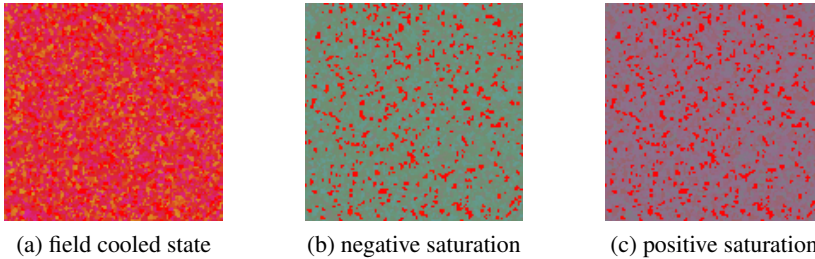


Figure 4.19: Sum of the magnetisation vectors of the 2 AFM sublattices. Figure 4.19a: field cooled case after initial relaxation. Figure 4.19b: at negative saturation of the FM. Some grains are in a spin flipped state (red) along the field cooling direction while other grains have undergone Hoffmann training (grey/blue). Figure 4.19c: at positive saturation of the FM.

This spin flipped state of some AFM grains is also reflected in the average magnetisation of the AFM layer. One finds in the polycrystalline case that $\langle m_{x,\text{AFM}} \rangle \approx 0.41$ at positive saturation, but also $\langle m_{x,\text{AFM}} \rangle \approx 0.03$ at negative saturation. However, in the uniform phase diagram we find that $\langle m_{x,\text{AFM}} \rangle$ is symmetric, i.e. $\langle m_{x,\text{AFM}} \rangle \approx 0.24$ and $\langle m_{x,\text{AFM}} \rangle \approx -0.24$ at positive and negative saturation of the FM layer, respectively.

Also a small asymmetry can be induced by the finite number of AFM grains in our simulation box and a finite distribution of biaxial anisotropy axes, which can lead to a net preferred direction. Thus to summarise, in this region one can find Hoffmann training as well as permanent exchange bias, as follows from the overlap of the phase diagrams 4.17 and 4.18.

In the region $j = 2$, $k = 1.6$ a spin flip transition of the 2 AFM layers occurs, analogous to the uniform case. The moments of the 2 AFM layers inside an AFM grain will be parallel after the first reversal ($n = 1$) towards negative saturation. This spin flip state, together with the limited size of our simulation box, produces also here a small exchange bias.

One can thus conclude that the average behaviour of a polycrystalline AFM is analogous to the case where the two biaxial anisotropy axes are set symmetrical along the field cooling direction.

4.7 Example: Training in an IrMn/CoFe bilayer

4.7.1 Introduction

As a last example of athermal training effects in a compensated AFM and as an illustration of the simultaneous implementation of exchange bias and spin flop coupling in MuMax³, we reproduced an experimental hysteresis loop of an exchange biased IrMn(15nm)/CoFe(10nm) bilayer, measured at 15 K, as was reported by Fulara et al[64].

In figure 4.20, one can see the experimental hysteresis loop ($n = 1$) when no external field was applied while cooling the sample (ZFC, black line) and when the sample was field cooled (FC, red line). The exchange bias in the ZFC loop can be explained by the positive remanent state of the CoFe layer before the cooling procedure[64, 25], as was already discussed in section 2.3.4. The inset shows the first ($n = 1$) and second ($n = 2$) hysteresis loop in the field cooled case.

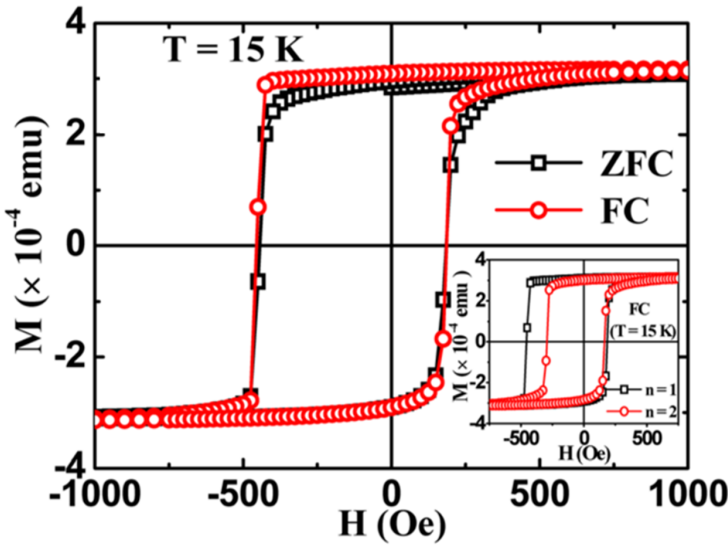


Figure 4.20: Experimental hysteresis loop of an IrMn(15nm)/CoFe(10nm) bilayer at a temperature of 15 K when no external field was applied while cooling the sample (ZFC, black line) and in the field cooled case (FC, red line). The inset shows the first ($n = 1$) and second ($n = 2$) hysteresis loop in the field cooled case.

Although IrMn has a uniaxial anisotropy at high temperatures, experimental evidence[104, 64] shows that, due to interlayer mixing[64] at the FM/AFM interface, the AFM undergoes a phase transition at 50K and develops a biaxial anisotropy during cooling. The observed training, after cooling in an external field $H_{fc} = 180$ mT, is attributed to Hoffmann training (inset figure 4.20) as the training does not follow the power law (equation 3.1) for thermal training, as is shown in figure 3.1. Due to the combination of this biaxial anisotropy and the interface interaction, the AFM sublattices are forced into a frustrated non collinear state, leading to athermal training as was discussed in section 4.6. Also note the asymmetric shape of the first hysteresis loop.

4.7.2 Micromagnetic model

The simulation box will be divided into $512 \times 512 \times (2 \text{ AFM} + 1 \text{ FM})$ cells of 3 nm in lateral size and 10 nm in thickness. For the FM, typical parameters [105, 106] were used: $M_{\text{FM}} = 1600$ kA/m and $A_{\text{FM}} = 2.5 \times 10^{-11}$ J/m. A small uniaxial anisotropy ($K_{\text{FM}} = 4$ kJ/m³) was applied in the field cooling direction to model the effect of an external field during deposition. The antiferromagnetic IrMn was divided into 20 nm grains and the anisotropy axes were randomly distributed. In the AFM, no intergrain interaction was taken into account. To simulate an infinite thin film, periodic boundary conditions (5,5,0) were applied along the in-plane directions.

The parameters¹⁴ of the AFM layer were tuned in order to match the experimental hysteresis loop: $A_{\text{AFM}} = -1.88 \times 10^{-11}$ J/m, $A_{\text{I}} = 1.7 \times 10^{-11}$ J/m and as biaxial anisotropy constant we used $K_{\text{c,AFM}} = 2.25 \times 10^5$ J/m³. Approximately 20 % of the AFM spins were initialized into a 45° canted position with respect to the field cooling direction and 76 % were randomly, but with antiparallel sublattices, distributed. To produce a small exchange bias field for $n \geq 2$, about 4 % pinned¹⁵ uncompensated spins were randomly added to the AFM layers, as discussed before (section 4.3). A quasistatic hysteresis loop was simulated along the field cooling direction.

¹⁴For a rescaling of the AFM parameters to achieve the correct energy, see Appendix C.

¹⁵Due to the presence of compensated as well as uncompensated AFM spins, the uncompensated spins are modelled by 2 parallel sublattices. Each sublattice applies an energy density $J_{\text{I}} = 1.7$ mJ/m² on the FM, and so in total a surface energy density of 3.4 mJ/m² is applied on the FM layer.

4.7.3 Results

The resulting hysteresis loop is shown in figure 4.21. One can clearly see the asymmetry and the reduction of the coercivity in the first hysteresis loop.

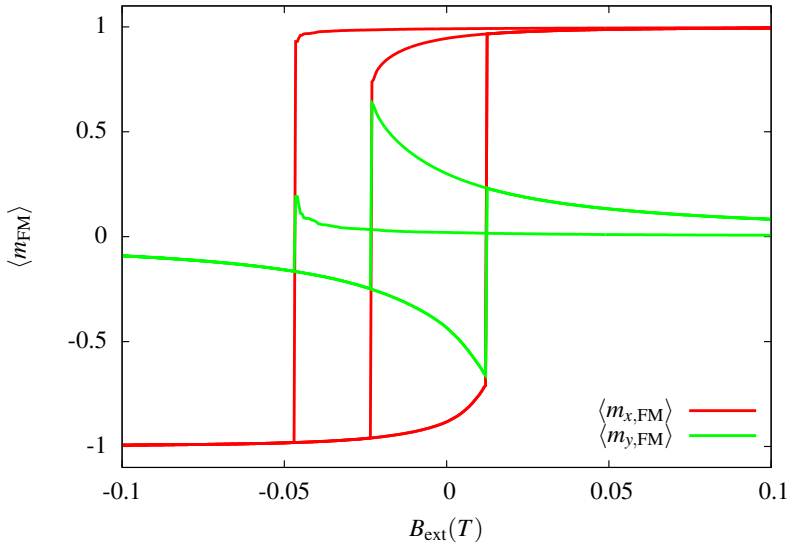


Figure 4.21: Simulated first and second hysteresis loop of an IrMn(15nm)/CoFe(10nm) bilayer. The average x and y components of the FM magnetisation are shown. The x direction corresponds to the field cooling direction.

Also the average orientation of an AFM grain, whose easy axes $K_{c,AFM}$ make an angle of 45° with respect to the field cooling direction fc, is shown in figure 4.22. Starting from the spin flop initialized states $AFM_{1,fc}$ and $AFM_{2,fc}$, the AFM sublattices relax towards position (a) when the FM reaches negative saturation. This relaxation from a non collinear to an antiparallel state produces athermal training as this is an irreversible transition. When the FM is saturated again in the field cooling direction, AFM_1 does not return to its initial position, but relaxes towards position (b) and thus stays in an almost antiparallel state with AFM_2 . In further hysteresis loops AFM_1 and AFM_2 only switch between positions (a) and (b). As this is a reversible transition, no training effect is obtained anymore for $n > 1$.

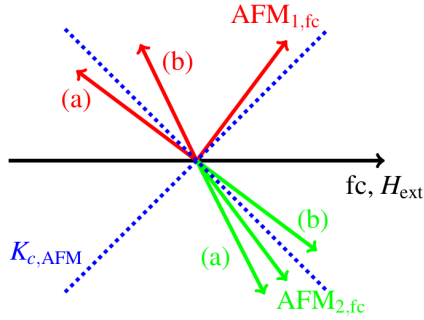


Figure 4.22: Average orientation of the sublattices inside an AFM grain, initialized in the spin flop state $AFM_{1,fc}$ and $AFM_{2,fc}$, whose easy axes $K_{c,AFM}$ make an angle of 45° with respect to the field cooling direction fc . The 2 sublattices (red and green) relax from a non collinear to the antiparallel state (a) after the FM has switched towards negative saturation in $n = 1$. Position (b) represents the configuration of the AFM layers at positive saturation again.

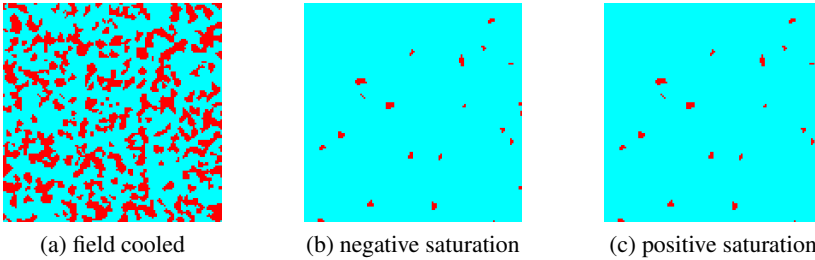


Figure 4.23: Training effect in an IrMn/CoFe bilayer. Red color: grains in which the 2 AFM layers are non collinear, blue color: grains in which the 2 AFM layers are antiparallel. Only the AFM layers in the pinned uncompensated grains stay parallel after reaching negative saturation in the first hysteresis loop. A quarter of the simulation box is shown.

In figure 4.23, one can see in which grains the 2 AFM layers are in a non collinear (red color) and antiparallel¹⁶ (blue color) state after field cooling and at negative saturation for $n = 1$. One can see that, after the first reversal of the FM towards negative saturation, the 2 AFM layers are antiparallel in all grains, except in those of the pinned uncompensated AFM grains. For comparison, the case of a polycrystalline IrMn layer with uniaxial anisotropy is shown in figure 4.24. As expected, no training effect is found.

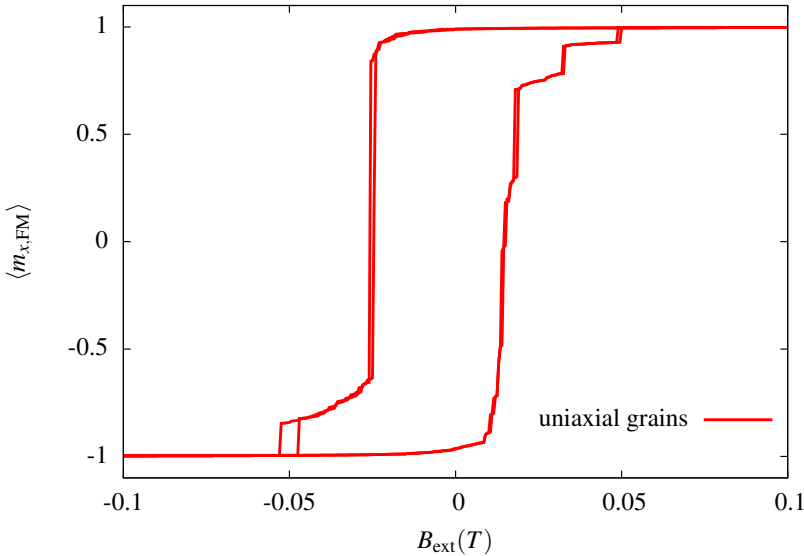


Figure 4.24: Hysteresis loop for a polycrystalline AFM with uniaxial anisotropy $K_{AFM} = \frac{K_{c,AFM}}{4}$, due to the definition of the biaxial anisotropy energy density.

¹⁶The 2 AFM layers inside a grain are considered antiparallel when the angle between both layers is larger than 140° as in our case the angle between the 2 magnetisation vectors will be always larger than 90° , see e.g. the field cooled state in figure 4.22.

4.8 Conclusions

We have studied how the MuMax³ framework can be used to implement compensated antiferromagnetic interfaces. Using the small canting angle approximation, we have shown that, for low coupling strengths, we can approximate the interfacial interaction by introducing a uniaxial anisotropy axis, perpendicular to the Néel vector of the antiferromagnet, acting on the ferromagnetic layer. In the case of strong coupling, we can take into account the exact energy terms, describing the interaction between a compensated antiferromagnet and a ferromagnet, by adding two extra layers to the simulation box. This approach allows us to study more complex magnetic systems, reproduce athermal training effects and model mixed AFM interfaces.

CONCLUSIONS AND OUTLOOK

The whole is greater than the sum of its parts.

Aristotle

5.1 Conclusions

We have studied how compensated and uncompensated antiferromagnetic interfaces can be implemented in MuMax³ and how it can be used to investigate e.g. training effects in a compensated AFM with biaxial anisotropy. As at an antiferromagnetic interface often compensated as well as uncompensated spins are present, the most general approach is by adding two extra layers to the simulation box. Using this method, we can obtain exchange bias and an enhanced coercivity due to frozen and rotatable uncompensated AFM spins, respectively. Also the formation of a planar domain wall in the antiferromagnet, was discussed in the model of Mauri, can easily be taken into account. We have confirmed that a trained hysteresis loop can be reinitialised to an apparent field cooled state.

We have also shown how the magnitude of the spin flop coupling in a compensated AFM interface is related to physical parameters and how it induces a uniaxial anisotropy in the ferromagnet, in case of small AFM canting angles. For strong coupling between the FM and the AFM layer or a high AFM anisotropy, the exact energy terms have to be taken into account as exchange bias or a spin flip transition can occur.

Using this implementation, we can produce athermal training effects in compensated as well as uncompensated antiferromagnetic interfaces and we can explain the typical asymmetry between the descending and the as-

ending branch of the first hysteresis loop. This allows us to reproduce experimental data, e.g. training in a Co/CoO bilayer[60]. As all these effects can be taken into account in one micromagnetic simulation, we can give a realistic description of FM/AFM interfaces.

5.2 Future outlook

5.2.1 More advanced models

Having demonstrated the implementation of antiferromagnetic interfaces in MuMax³ for the first time, we have opened a door for new micromagnetic studies of static effects of AFM interfaces on FM layers or on the stability of FM domain configurations. This implementation can easily be extended to antiferromagnets with a symmetry higher than biaxial anisotropy, to the case in which the 2 sublattices couple differently towards the ferromagnet or to the case in which an antiferromagnet exists of 3 sublattices. Also the origin and the conditions for the existence of positive exchange bias can be further investigated as well as the effects of compensated or uncompensated AFM interfaces on the domain wall motion in a ferromagnet. In 2015, Gilbert et al.[107] discovered that magnetic vortices in exchange biased Fe₂₀Ni₈₀/Ir₂₀Mn₈₀ nanodisks are viscously dragged due to uncompensated AFM spins at the interface. This leads to a distortion of the vortex at the FM/AFM interface and an asymmetry in the annihilation and nucleation fields. These systems can easily be studied by using the micromagnetic model we have proposed in this thesis.

5.2.2 Antiferromagnetic spintronics

Furthermore, a new and very promising field is emerging in magnetism: antiferromagnetic spintronics. Because antiferromagnets have no net magnetisation, do not produce stray fields and hardly couple to external fields, they are very stable against magnetic perturbations. This makes AFM themselves very suitable as a way to store data and not just to pin a FM layer, as is done in reading heads or MRAM devices. To use antiferromagnets in technological applications however, one needs to find a way to manipulate the Néel axis of the AFM. This can only be done by applying a staggered effective field, i.e. the sign of the field has to alternate between the 2 collinear AFM sublattices as otherwise no net torque is produced. This implicates e.g. that a uniform magnetic field cannot switch an antiferromagnet.

Very recently, in 2014, Železný et al.[108] made a groundbreaking discovery. They have shown that one can reorientate the AFM spin axis by applying an in-plane current in the AFM layer and by making use of Néel-order spin orbit torque (NSOT). This is a relativistic effect and doesn't require any prior spin polarisation of the current in contrast with spin transfer torque. NSOT can only be applied in AFM crystals with an appropriate symmetry[108, 109], e.g. the sublattices have to form inversion partners which is the case in antiferromagnets such as Mn_2Au and CuMnAs .

Labeling the 2 collinear sublattices of such an AFM as 1 and 2, the current applies, under specific circumstances, an effective field on each sublattice in an opposite direction, so $\mathbf{H}_1 = -\mathbf{H}_2$. The effective field is perpendicular to the current direction. The torque on each sublattice is given by $\tau_{1,2} = \frac{d\mathbf{M}_{1,2}}{dt} \propto \mathbf{M}_{1,2} \times \mathbf{H}_{1,2}$ and so a net torque exists, similar to the torque applied by an electric field on an electric dipole. This means that NSOT can rotate the AFM as a whole and thus can lead to electrical switching. This has experimentally been verified (2016) at room temperature in antiferromagnetic CuMnAs [109] by the electrical switching of the AFM between 2 perpendicular in-plane easy axes, as can be seen in figure 5.1. Applying a current in the $[100]$ direction leads to a switching of the AFM towards the $[010]$ direction and vice versa. The difference between these 2 orientations can be detected with AMR[109, 110]. As the AFM sublattices rotate as a whole and so no high frequency dynamics are involved, the influence of the switching of an AFM, coupled to a FM layer, can potentially also be investigated by using our micromagnetic model for an AFM interface.

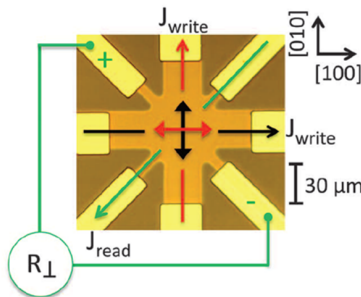


Figure 5.1: By applying a current pulse in the $[100]$ direction (black arrow), one can switch the antiferromagnet 90° (from red to black) due to NSOT.

Interestingly, Fukami[111] has shown in 2015 that an exchange biased Co/Ni multilayer can be switched by applying a current in the underlying AFM layer, in this case PtMn. The multilayer has an out-of-plane easy axis (see figure 5.2), perpendicular to the in-plane easy axis of the AFM. By inducing a spin orbit torque (SOT) on the FM layer due to an in-plane current in the AFM layer, together with the exchange coupling between the FM and the AFM, one can switch the perpendicular magnetisation of the FM. The big advantage of this method is that, in contrast to ordinary non-magnetic/FM stacks, no in-plane magnetic field needs to be applied in the current direction to allow for a deterministic switching of the ferromagnet. In this case, the external field is replaced by the bias field, induced by the exchange interaction between the ferromagnet and the antiferromagnet.

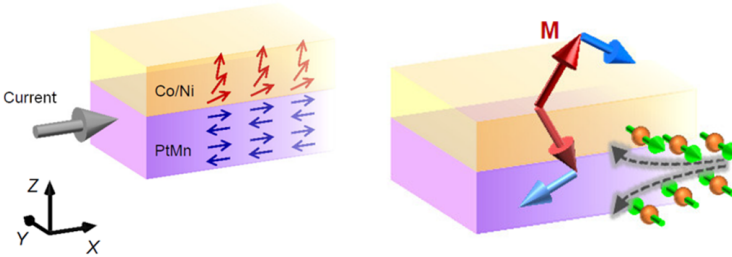


Figure 5.2: Left: direction of the applied current and the magnetisation vectors of the ferromagnetic Co/Ni multilayer and the antiferromagnetic PtMn layer. The out-of-plane magnetised ferromagnet is tilted at the FM/AFM interface due to exchange bias. Right: due to the SOT an effective field (blue arrows) is applied on the FM (red arrows). This torque can switch the FM parallel or antiparallel to the z -axis. Reproduced from [111].

One can thus conclude that, despite Louis Néel claimed that he *did not foresee any applications of antiferromagnets*, a renewed interest is gained in the last 10 years. Being able to model the interaction between a ferromagnet and an antiferromagnet in a realistic way is thus crucial to explore the implications of these recent advancements in search for new or better technologies.

The Bird of Paradise, renewed each century,
born in flame, ending in flame!
Thy picture, in a golden frame,
hangs in the halls of the rich,
but thou thyself often fliest around,
lonely and disregarded, a myth,
the Phoenix of Arabia.

In Paradise,
when thou wert born in the first rose,
beneath the Tree of Knowledge,
thou receivedst a kiss,
and thy right name was given thee
thy name, Poetry.

Hans Christian Andersen, *The Phoenix Bird*

PUBLICATIONS

- *Non-linear radial spinwave modes in thin magnetic disks*[112]
M. Helsen, A. Gangwar, **J. De Clercq**, A. Vansteenkiste, M. Weigand,
C. H. Back, and B. Van Waeyenberge
Appl. Phys. Lett. 106, 032405 (2015)
- *Modelling exchange bias with MuMax³*[1]
J. De Clercq, A. Vansteenkiste, M. Abes, K. Temst
and B. Van Waeyenberge
J. Phys. D: Appl. Phys. 49 435001 (2016)
- *Modelling compensated antiferromagnetic interfaces with MuMax³*[2]
J. De Clercq, J. Leliaert and B. Van Waeyenberge
Formally accepted by Journal of Physics D: Applied Physics (2017)
arXiv:1704.04030
- *Topical review: Fast micromagnetic simulations on GPU*
J. Leliaert, M. Dvornik, J. Mulkers, **J. De Clercq**
and B. Van Waeyenberge
Submitted to Journal of Physics D: Applied Physics (2017)
- *Adaptively time stepping the stochastic Landau-Lifshitz-Gilbert
equation at nonzero temperature: implementation and validation
in MuMax³*
J. Leliaert, M. Dvornik, J. Mulkers, **J. De Clercq**, A. Coene
and B. Van Waeyenberge
In preparation for AIP Advances (2017)
- Poster 1
Modelling exchange bias with MuMax³
Belgian Physical Society, Ghent, Belgium (2016)
- Poster 2
Modelling compensated antiferromagnetic interfaces with MuMax³
Intermag, Dublin, Ireland (2017)



Journal of Physics series

On the 50th anniversary of
Journal of Physics D: Applied Physics

This is to certify that the article:

Modelling exchange bias with MuMax³

**by Jonas De Clercq, Arne Vansteenkiste, Medjid Abes,
Kristiaan Temst and Bartel Van Waeyenberge**

has been selected by the Editorial Board of
Journal of Physics D: Applied Physics for inclusion in the exclusive
'Highlights of 2016' collection, and were chosen on the basis of
novelty, scientific impact and broadness of appeal

Tom Miller

Executive Editor

Journal of Physics D: Applied Physics

Appendices

STONER WOHLFARTH FOR GENERAL ANGLES γ

Defining $h_x = h \cos(\gamma)$ and $h_y = h \sin(\gamma)$ so that $h = \sqrt{h_x^2 + h_y^2}$, we can rewrite the stability equations 1.59 as

$$\frac{\partial \varepsilon}{\partial \beta} = \frac{1}{2} \sin(2\beta^*) + h_x \sin(\beta^*) - h_y \cos(\beta^*) = 0 \quad (\text{A.1})$$

$$\frac{\partial^2 \varepsilon}{\partial \beta^2} = \cos(2\beta^*) + h_x \cos(\beta^*) + h_y \sin(\beta^*) > 0 \quad (\text{A.2})$$

The last condition determines if, for a given value of (h_x, h_y) or equivalent a magnitude H_{ext} and an angle γ , two relative minima (one stable and one metastable) or only 1 absolute minimum is present¹. The critical curve between those 2 regions is determined by $\frac{\partial^2 \varepsilon}{\partial \beta^2} = 0$ together with $\frac{\partial \varepsilon}{\partial \beta} = 0$. This leads to parametric equations $h_x = h_x(\gamma)$ and $h_y = h_y(\gamma)$. Using that

$$\sin(\beta^*) \left[\frac{\partial \varepsilon}{\partial \beta} \right] + \cos(\beta^*) \left[\frac{\partial^2 \varepsilon}{\partial \beta^2} \right] = 0 \quad (\text{A.3})$$

one immediately obtains that $h_x = -\cos^3(\beta^*)$ and thus also $h_y = \sin^3(\beta^*)$ and thus one retrieves the famous Stoner Wohlfarth[10] asteroid equation

$$h_x^{\frac{2}{3}} + h_y^{\frac{2}{3}} = 1 \quad (\text{A.4})$$

The magnitude of the switching field can be written as

$$h = \left[\frac{1}{\cos^{\frac{2}{3}}(\gamma) + \sin^{\frac{2}{3}}(\gamma)} \right]^{\frac{3}{2}} \quad (\text{A.5})$$

¹This is similar to the case $\gamma = 0$ for $|h| < 1$ and $|h| > 1$ respectively.

EXCHANGE BIAS FOR AN UNCOMPENSATED AFM

In section 3.2, we have shown that the exchange bias field (equation 3.9), induced by a pinned ($J_I < K_{\text{AFM}}t_{\text{AFM}}$) uncompensated AFM macro spin, is given by

$$B_{\text{eb}} = -\frac{J_I}{M_{\text{FM}}t_{\text{FM}}}\sqrt{1 - \left(\frac{J_I}{2K_{\text{AFM}}t_{\text{AFM}}}\right)^2} \quad (\text{B.1})$$

by considering that a reversible hysteresis loop¹ has a vanishing coercivity and thus the bias field is defined by the condition $B_{\text{eb}} = B_{\text{ext}} (\beta^* = \frac{\pi}{2})$. We will now show that, due to the asymmetry of the hysteresis loop, the bias field cannot be defined by using the stability requirements which follow from the second order derivatives and the Hessian determinant.

To find the stability positions for the FM and AFM, given by β^* and ϕ^* respectively, one has to minimize the total energy as given in 3.2. The definitions of the angles are shown in figure B.1.

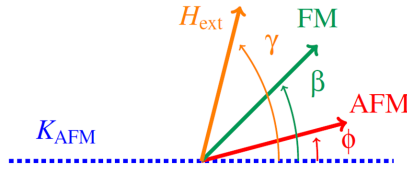


Figure B.1: The angles γ , β and ϕ are defined with respect to the uniaxial axis (blue line) of the uncompensated antiferromagnetic macrospin.

¹between the positions ($\beta^* = 0, \phi^* = 0$) and ($\beta^* = \pi, \phi^* = 0$)

For $\gamma = 0$ and $J_A = 0$, the angles β^* and ϕ^* are determined by

$$\frac{\partial \sigma}{\partial \beta} = \mu_0 H_{\text{ext}} M_{\text{FM}} t_{\text{FM}} \sin(\beta^*) + J_I \sin(\beta^* - \phi^*) = 0 \quad (\text{B.2})$$

$$\frac{\partial \sigma}{\partial \phi} = -J_I \sin(\beta^* - \phi^*) + t_{\text{AFM}} K_{\text{AFM}} \sin(2\phi^*) = 0 \quad (\text{B.3})$$

One can find 4 straight forward solutions, which are given by $(\beta^* = 0, \phi^* = 0)$, $(\beta^* = \pi, \phi^* = 0)$, $(\beta^* = \pi, \phi^* = \pi)$, $(\beta^* = 0, \phi^* = \pi)$ corresponding to the saturated states of the FM and AFM. These solutions minimize the total energy if

$$\frac{\partial^2 \sigma}{\partial \beta^2} = \mu_0 H_{\text{ext}} M_{\text{FM}} t_{\text{FM}} \cos(\beta^*) + J_I \cos(\beta^* - \phi^*) > 0$$

$$\frac{\partial^2 \sigma}{\partial \phi^2} = 2K_{\text{AFM}} t_{\text{AFM}} \cos(2\phi^*) + J_I \cos(\beta^* - \phi^*) > 0$$

$$\begin{aligned} \text{Hess}(\theta, \phi) &= 2K_{\text{AFM}} t_{\text{AFM}} J_I \cos(\beta^* - \phi^*) \cos(2\phi^*) \\ &\quad + \mu_0 H_{\text{ext}} M_{\text{FM}} t_{\text{FM}} 2K_{\text{AFM}} t_{\text{AFM}} \cos(\beta^*) \cos(2\phi^*) \\ &\quad + \mu_0 H_{\text{ext}} M_{\text{FM}} t_{\text{FM}} J_I \cos(\beta^*) \cos(\beta^* - \phi^*) > 0 \end{aligned}$$

We will only consider the case of pinned uncompensated spins, which satisfy the condition $J_I < K_{\text{AFM}} t_{\text{AFM}}$.

Case 1: $(\beta^* = 0, \phi^* = 0)$

Stability requirements show that this solution corresponds to an energy minimum if

$$\mu_0 H_{\text{ext}} > -\frac{J_I}{M_{\text{FM}} t_{\text{FM}}} \quad (\text{B.4})$$

$$J_I > -2K_{\text{AFM}} t_{\text{AFM}} \quad (\text{B.5})$$

$$\mu_0 H_{\text{ext},1} > -\frac{J_I}{M_{\text{FM}} t_{\text{FM}} \left(1 + \frac{J_I}{2K_{\text{AFM}} t_{\text{AFM}}}\right)} \quad (\text{B.6})$$

For $J_I > 0$, the second inequality does not provide any restriction, independent of J_I and $K_{\text{AFM}} t_{\text{AFM}}$, and is always satisfied. The third inequality, which is more strict than the first inequality, determines the start of the switching of the FM macrospin in the hysteresis loop for $H_{\text{ext}} < 0$ and the loss of stability of the solution $(\beta^* = 0, \phi^* = 0)$ if the Hessian determinant $H(\theta, \phi) = 0$.

Case 2: ($\beta^* = \pi, \phi^* = 0$)

This solution corresponds to the state in which the FM is completely reversed. Stability requirements show that

$$\mu_0 H_{\text{ext}} < -\frac{J_{\text{I}}}{M_{\text{FM}} t_{\text{FM}}} \quad (\text{B.7})$$

$$J_{\text{I}} < 2K_{\text{AFM}} t_{\text{AFM}} \quad (\text{B.8})$$

$$\mu_0 H_{\text{ext},2} < -\frac{J_{\text{I}}}{M_{\text{FM}} t_{\text{FM}} \left(1 - \frac{J_{\text{I}}}{2K_{\text{AFM}} t_{\text{AFM}}}\right)} \quad (\text{B.9})$$

taking into account that $J_{\text{I}} - 2K_{\text{AFM}} t_{\text{AFM}} < 0$. For $J_{\text{I}} > 0$, this solution is stable for pinned AFM spins as well as rotatable spins if the latter satisfy the condition $K_{\text{AFM}} t_{\text{AFM}} < J_{\text{I}} < 2K_{\text{AFM}} t_{\text{AFM}}$.

Shift of the hysteresis loop

If we define the shift of the hysteresis loop, using the stability requirements, we find

$$B_{\text{shift}} = \mu_0 \left(\frac{H_{\text{ext},2} + H_{\text{ext},1}}{2} \right) \quad (\text{B.10})$$

$$= -\frac{J_{\text{I}}}{2M_{\text{FM}} t_{\text{FM}}} \left(\frac{1}{1 - \frac{J_{\text{I}}}{2K_{\text{AFM}} t_{\text{AFM}}}} + \frac{1}{1 + \frac{J_{\text{I}}}{2K_{\text{AFM}} t_{\text{AFM}}}} \right) \quad (\text{B.11})$$

$$= -\frac{J_{\text{I}}}{M_{\text{FM}} t_{\text{FM}}} \left(\frac{1}{1 - \frac{J_{\text{I}}^2}{4K_{\text{AFM}}^2 t_{\text{AFM}}^2}} \right) \quad (\text{B.12})$$

which is different from the exact bias field as given in B.1 due to the asymmetry of the hysteresis loop. In the case of small coupling constants J_{I} , both bias fields reduce to the expression as found in the rigid Meiklejohn and Bean model (equation 2.9), i.e.

$$B_{\text{cb}} = B_{\text{shift}} \approx -\frac{J_{\text{I}}}{M_{\text{FM}} t_{\text{FM}}} \quad (\text{B.13})$$

IMPLEMENTATION OF A COMPENSATED INTERFACE

A compensated AFM with thickness t_{AFM} can be modelled in MuMax³[12] by adding 2 extra layers, labeled by AFM₁ and AFM₂, to the simulation box, as shown in figure C.1. In this way, the cell size perpendicular to the FM/AFM interface is set equal to the AFM layer thickness, i.e. $t_{\text{AFM}} = C_z$. If $C_z \neq t_{\text{AFM}}$, the energy terms in the AFM layers have to be rescaled as detailed in section C. To these two AFM layers, one can attribute effective parameters, e.g. an anisotropy constant K_{AFM} , to ensure all the energy contributions of the AFM are included. As only nearest neighbouring cells are taken into account for the evaluation of the exchange energy in MuMax³, one has to couple the bottom layer AFM₁ with the FM layer explicitly by adding a custom field and corresponding custom energy term.

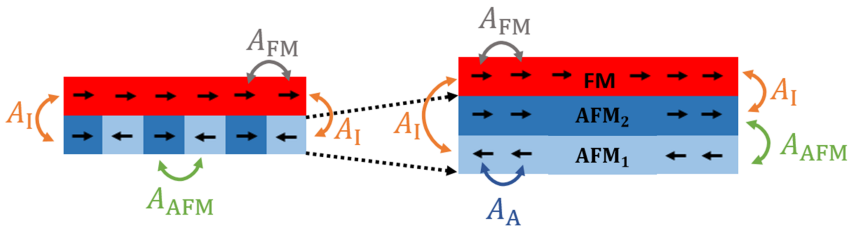


Figure C.1: Micromagnetic model of a compensated AFM/FM in MuMax³. AFM₂ can be coupled to the FM by rescaling the exchange energy. The FM and AFM₁ layer have to be coupled to each other using periodic boundary conditions or by defining a custom field / energy term.

AFM domain wall energy and physical interpretation of the interlayer and intralayer exchange stiffness

To demonstrate the validity of our micromagnetic model for the AFM, we investigate the energy of a 90° domain wall, shown in figure C.2. It also illustrates the physical meaning of the interlayer exchange stiffness $A_{\text{AFM}} < 0$ and the intralayer exchange stiffness $A_{\text{A}} > 0$. In our micromagnetic model (figure C.2, bottom), the atomic AFM sublattices are separated into 2 layers (AFM₁ and AFM₂) and the interlayer interaction A_{AFM} replaces the negative exchange stiffness A_1 associated with the nearest neighbour interaction between two antiparallel AFM spins, e.g. spin 1 and 2 in figure C.2 (top). The intralayer exchange stiffness A_{A} in our model is responsible for the lateral coupling between the AFM spins and ensures a domain wall can be formed in the AFM.

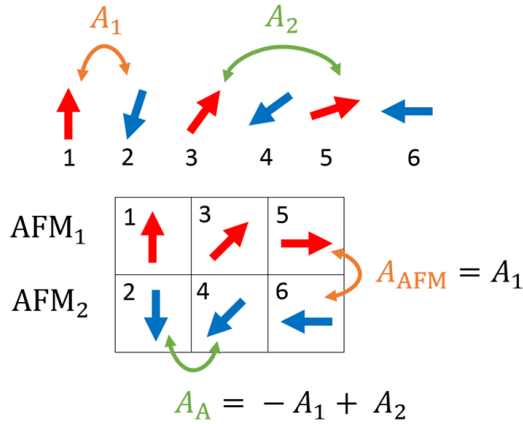


Figure C.2: Top: representation of an AFM domain wall. A_1 and A_2 represent the exchange stiffnesses which can be associated with the nearest and next nearest neighbour interaction. Bottom: micromagnetic model of an AFM domain wall. AFM₁ and AFM₂ are the 2 AFM layers. A_{AFM} and A_{A} are the interlayer and intralayer exchange stiffnesses respectively. In our micromagnetic model spin 2 and 3 are not coupled.

To determine the correct value of the exchange stiffness A_{A} , we compare the domain wall energy of the two models (figure C.2 (top) and figure C.2 (bottom)), given by ϵ_{at} and ϵ_{m} respectively.

Demanding that the total domain wall energy of $2N$ spins, spread over a distance $2N\Delta$, is the same in both cases, one obtains

$$\begin{cases} \epsilon_{\text{at}} = -(2N - 1) \frac{A_{\text{AFM}}}{\Delta^2} \cos(\theta) \\ \epsilon_{\text{m}} = -2(N - 1) \frac{A_{\text{A}}}{(2\Delta)^2} \cos(\theta_{\text{m}}) \end{cases} \quad (\text{C.1})$$

with θ the angle between neighbouring AFM spins, at a distance Δ and θ_{m} the angle between two next nearest neighbouring AFM spins at a distance 2Δ . Introducing the angle $\alpha = \pi - \theta$, which is small for large N , one can see that $\theta_{\text{m}} \approx 2\alpha$. Using the small angle approximation, we find

$$\begin{cases} \epsilon_{\text{at}} = (2N - 1) \frac{A_{\text{AFM}}}{\Delta^2} \cos(\alpha) \approx (2N - 1) \frac{A_{\text{AFM}}}{\Delta^2} \left(1 - \frac{\alpha^2}{2}\right) \\ \epsilon_{\text{m}} = -2(N - 1) \frac{A_{\text{A}}}{4\Delta^2} \cos(2\alpha) \approx -(N - 1) \frac{A_{\text{A}}}{2\Delta^2} (1 - 2\alpha^2) \end{cases} \quad (\text{C.2})$$

So for large N and neglecting constant energy offsets, we obtain that the total energy densities ϵ_{at} and ϵ_{m} are equal if $A_{\text{A}} \approx -A_{\text{AFM}}$.

If also the next nearest neighbour ferromagnetic exchange interaction A_2 is considered (e.g. between spins 3 and 5 in figure C.2 (top)), it needs to be added to the intralayer exchange stiffness A_{A} . So in our micromagnetic model, A_{A} will generally be larger than $|A_{\text{AFM}}|$.

Another approach would be by correctly averaging out the interaction of a macrospin in 1 AFM layer with the next nearest neighbours of the other AFM layer by adding extra custom field and energy terms to our micromagnetic model. In this 1 dimensional model, spin 4 would interact with spin 3 and a weighted interaction with spin 5 and spin 1, to restore the translational symmetry of the exchange energy.

Setting the exchange coupling between the FM and AFM layers

When a FM layer with exchange stiffness A_{FM} and saturation magnetisation M_{FM} and an AFM layer with an intralayer exchange stiffness A_{A} and saturation magnetisation M_{AFM} are neighbours, MuMax³ will average out the interlayer contribution to the exchange energy by calculating the harmonic mean α_{H} of the quantities $\frac{A_{\text{FM}}}{M_{\text{FM}}}$ and $\frac{A_{\text{A}}}{M_{\text{AFM}}}$ which is defined as

$$\alpha_{\text{H}} = \frac{2 \frac{A_{\text{FM}}}{M_{\text{FM}}} \frac{A_{\text{A}}}{M_{\text{AFM}}}}{\frac{A_{\text{FM}}}{M_{\text{FM}}} + \frac{A_{\text{A}}}{M_{\text{AFM}}}} \quad (\text{C.3})$$

This averaging follows from the fact that in MuMax³ the exchange stiffness is attributed to the volume of a cell, rather than being defined at the interface between 2 cells.

To obtain a total surface energy density J_{I} between the AFM₂ and the FM layer, one has to rescale the exchange energy density between the FM and the AFM₂ regions by making use of the scaling factor S , as introduced in equation 9 of the MuMax³ paper[12]. One can calculate that the scaling factor S has to be given by

$$S = \frac{J_{\text{I}} C_z}{\alpha_{\text{H}} (M_{\text{FM}} + M_{\text{AFM}})} \quad (\text{C.4})$$

This scaling factor has to be introduced in the function `ext_ScaleExchange` as defined in the MuMax³ API which can be found at <http://mumax.github.io/api.html>.

Saturation magnetisation of the AFM layers

To divide the interface energy density J_{I} equally between a FM and AFM cell, one has to set the saturation magnetisations (as micromagnetic input parameters in MuMax³) of the ferromagnet and antiferromagnet to equal values, i.e. $M_{\text{FM}} = M_{\text{AFM}}$. As no demagnetisation energy is taken into account for the AFM layers, changing M_{AFM} has no influence on the evolution to the minimal energy in the micromagnetic simulations. As the effective field terms acting on the AFM cell scale with $\frac{1}{M_{\text{AFM}}}$, the direction of the total effective field is not changed and thus still points in the direction of minimal energy. This rescaling only results in a rescaling of the time in the Landau-Lifshitz-Gilbert equation.

Coupling of the extra AFM layer to the FM layer by a custom energy term

To ensure that also the AFM₁ layer, which is not directly neighbouring the FM layer, is exchange coupled to the FM layer, a custom effective field and energy term¹ can be added in MuMax³. The contribution to the exchange energy density[12] in a FM cell due to the coupling with an AFM₁ cell can be expressed as

$$\epsilon_{\text{ex,FM}} = -\frac{1}{2}M_{\text{FM}}\mathbf{m}_{\text{FM}} \cdot \mathbf{B}_1 \quad (\text{C.5})$$

with \mathbf{m}_{FM} the normalised magnetisation vector of the FM cell and the effective field term \mathbf{B}_1 as

$$\mathbf{B}_1 = \frac{J_{\text{I}}}{C_z M_{\text{FM}}} (\mathbf{m}_{\text{AFM}} - \mathbf{m}_{\text{FM}}) \quad (\text{C.6})$$

with \mathbf{m}_{AFM} the normalised magnetisation vector of the underlying AFM₁ cell. The contribution to the energy density in an AFM₁ cell due to the coupling with a FM cell is

$$\epsilon_{\text{ex,AFM}} = -\frac{1}{2}M_{\text{FM}}\mathbf{m}_{\text{AFM}} \cdot \mathbf{B}_2 = \epsilon_{\text{ex,FM}} \quad (\text{C.7})$$

To ensure the interface energy density is equally divided between both layer, one has to set $M_{\text{FM}} = M_{\text{AFM}}$ as discussed in subsection C. For the effective field in the AFM₁ cell, we can write

$$\mathbf{B}_2 = \frac{J_{\text{I}}}{C_z M_{\text{FM}}} (\mathbf{m}_{\text{FM}} - \mathbf{m}_{\text{AFM}}) = -\mathbf{B}_1 \quad (\text{C.8})$$

Practically, the coupling of AFM₁ with the FM layer can easily be implemented in MuMax³ (from version 3.9.3) by adding following lines of code to the input script, assuming the FM is the top layer (n=2) and AFM₁ is the bottom layer (n=0).

```
f_I := (J_I) / (Cz*M_FM)
B_1 := Madd( M, shifted(M, 0, 0, 2), -f_I, f_I)
B_2 := Masked(Madd( M, shifted(M, 0, 0, -2), -f_I, f_I), layer(0))
B_ex := Add(Masked(B_1, layer(2)), B_2)
AddFieldTerm(B_ex)
AddEdensTerm(Mul(Mul(Const(-0.5), M_FM), Dot(M, B_ex)))
```

¹If the FM exists out of only 1 layer, one can also use periodic boundary conditions, in the direction perpendicular to the interface, i.e. `setPBC(0, 0, 1)`, and use the same scaling factor S as defined in section C.

Establishing the intersublattice exchange coupling between the two AFM layers

The interaction between the 2 layers AFM₁ and AFM₂ (see figure C.1), determined by the surface energy density δt_{AFM} , can be implemented by rescaling the exchange stiffness between the 2 AFM layers, analogous to what was discussed in section C. To obtain a total interface energy density δt_{AFM} , one can calculate that the scaling factor S has to be given by

$$S = -\frac{\delta t_{\text{AFM}} C_z}{2A_A} = \frac{A_{\text{AFM}}}{A_A} \quad (\text{C.9})$$

Note that the intralayer exchange stiffnesses A_A in the layers AFM₁ and AFM₂ are equal as each layer represents an AFM sublattice. In general, the exchange stiffness A_A can be different from the quantity $-A_{\text{AFM}}$, when taking into account the next nearest neighbour interaction (section C). In our simulations A_A is not a critical parameter as long as each layer inside an AFM grain is homogeneous within itself.

Rescaling energy terms

As MuMax³ uses a finite difference discretisation, the simulation box has to be divided into cells of equal sizes. If the total thickness of a simulation box is given by S_z and is divided into N_z cells in the z direction, then each cell has a thickness $C_z = \frac{S_z}{N_z}$. As in general, the thickness t_{FM} of the FM is different from the thickness t_{AFM} of the 2 AFM layers, a rescaling of the micromagnetic constants should be done in order to get the correct total energy in the AFM layers.

Choosing² a cell size C_z , perpendicular to the interface, the physical parameters A_A and $K_{\text{c,AFM}}$ should be rescaled as

$$A_A \rightarrow A_A \left(\frac{t_{\text{AFM}}}{C_z} \right)$$

$$K_{\text{c,AFM}} \rightarrow K_{\text{c,AFM}} \left(\frac{t_{\text{AFM}}}{C_z} \right)$$

where the values on the right hand side are the MuMax³ input parameters. For example, considering an AFM layer with thickness t_{AFM} and physi-

²If we discretize the FM in only 1 layer, we will set $C_z = t_{\text{FM}}$.

cal sublattice anisotropy constant $K_{c,AFM}$, we find that the total anisotropy energy³ in an AFM cell with cell sizes C_x , C_y and C_z is then given by

$$E_K = \frac{K_{c,AFM}}{4} \left(\frac{t_{AFM}}{C_z} \right) C_x C_y C_z = \frac{K_{c,AFM}}{4} C_x C_y t_{AFM} \quad (C.10)$$

which amounts to the correct physical anisotropy energy in an AFM cell with thickness t_{AFM} and lateral sizes C_x and C_y .

Also the Zeeman energy of the AFM layers can be taken into account by appropriately rescaling its value

$$B_{AFM} \rightarrow B_{AFM} \left(\frac{t_{AFM}}{C_z} \right)$$

Note that in MuMax³, the saturation magnetisation M_{AFM} of the antiferromagnet should be set equal to that of the ferromagnet, as discussed in section C. One can take into account the correct Zeeman energy of the AFM layers by rescaling the magnitude of the external field with a factor $\frac{M_{AFM,ph}}{M_{FM}}$ where $M_{AFM,ph}$ represents the physical sublattice saturation magnetisation of an antiferromagnet.

Example code

As an example of the implementation of a compensated AFM interface in MuMax³, we will simulate the hysteresis loop of a thin, infinite Py layer ($t_{FM} = 3$ nm), coupled to an AFM with thickness of $t_{AFM} = 3$ nm, uniaxial sublattice anisotropy constant $K_{AFM} = 7 \times 10^5$ J/m³, interface coupling $J_I = 0.7$ mJ/m² and mutual interaction $\delta = 1 \times 10^6$ J/m³ between the 2 AFM layers. In this case, the magnetostatic field is also switched off in the FM in order to be able to compare our results with the macrospin approach.

As the FM is discretized in only 1 layer and thus $t_{FM} = t_{AFM} = C_z$, it is sufficient to couple AFM₁ with the FM by making use of periodic boundary conditions in the z direction and thus exchange couple the bottom layer ($n=0$) with the top layer ($n=2$). When the FM is discretized into multiple layers, one has to leave out the statements `ext_ScaleExchange(0, 2, J_I*Cz/(2*M_FM*alpha_H))` and `setPBC(0,0,1)` in the code and add

³In case the magnetisation vector of the AFM cell is aligned at an angle of 45° with respect to the biaxial anisotropy axes.

the custom code to the input script, as discussed in section C. The FM was initialized in the spin flop state and the external field applied perpendicular to the anisotropy axis of the AFM. A small angle was introduced to break the symmetry in the system.

```
Nx := 64
Ny := 64
Nz := 3
Cx := 3.0e-9
Cy := 3.0e-9
Cz := 3.0e-9
setgridsize(Nx, Ny, Nz)
setcellsize(Cx, Cy, Cz)
setgeom(universe())
// FM is discretized in only 1 layer
setPBC(0,0,1)

DefRegion(0, Layer(0)) // AFM1 layer
DefRegion(1, Layer(1)) // AFM2 layer
DefRegion(2, Layer(2)) // FM layer

A_FM := 1.3e-11
M_FM:= 800e3
Aex.setRegion(2, A_FM)
Msat.setRegion(2, M_FM)
// only to compare with the macrospin approach
NoDemagSpins.SetRegion(2, 1)
m.setRegion(2, uniform(1, 0, 0))

t_AFM := Cz
// no rescaling is necessary as t_AFM = Cz
// divide the energy density equally between a FM and AFM cell
M_AFM := M_FM
K_AFM := 7.0e5
J_I := 0.7e-3
delta := 1.0e6
A_AFM := - delta*t_AFM*Cz/2
A_A := A_AFM
```

```

for i:=0; i<2; i++ {
// no demagnetisation energy for AFM layers
  NoDemagSpins.SetRegion(i, 1)
  Aex.setRegion(i, A_A)
  Msat.setRegion(i, M_AFM)
// sublattices are initialized antiparallel
  m.setRegion(i, uniform(0.1, pow(-1,i), 0))
  Kul.setregion(i,K_AFM)
  anisU.setregion(i,vector(0,1,0))
}

// harmonic mean for M_FM = M_AFM
alpha_H := (2/M_FM)*(1/(1/A_FM + 1/A_A))
// rescaling coupling between AFM2 and FM
ext_ScaleExchange(1, 2, J_I*Cz/(2*M_FM*alpha_H))
// rescaling coupling between AFM1 and FM
ext_ScaleExchange(0, 2, J_I*Cz/(2*M_FM*alpha_H))
// rescaling coupling between AFM1 and AFM2
ext_ScaleExchange(0, 1, A_AFM/A_A)

relax()
save(m)

B_app := 0.0
// save external field applied on FM layer
TableAddVar(B_app, "B_app", "T")
// save average magnetisation of FM layer
TableAdd(m.Region(2))
for i := 80; i > -81; i-- {
  B_app = i * 1e-3
  B_ext.setregion(2, vector(B_app*cos(1.0*pi/180),
                           B_app*sin(1.0*pi/180), 0))

  tablesave()
  relax()
}

```

```

for i := -79; i < 81; i++ {
  B_app = i * 1e-3
  B_ext.setregion(2, vector(B_app*cos(1.0*pi/180),
                           B_app*sin(1.0*pi/180), 0))

  tablesave()
  relax()
}

```

Using the coercive fields of the hysteresis loop (see figure C.3), we find that $B_c \approx 40$ mT which is in correspondence to equation 4.12 for $K_{\text{FM}} = 0$.

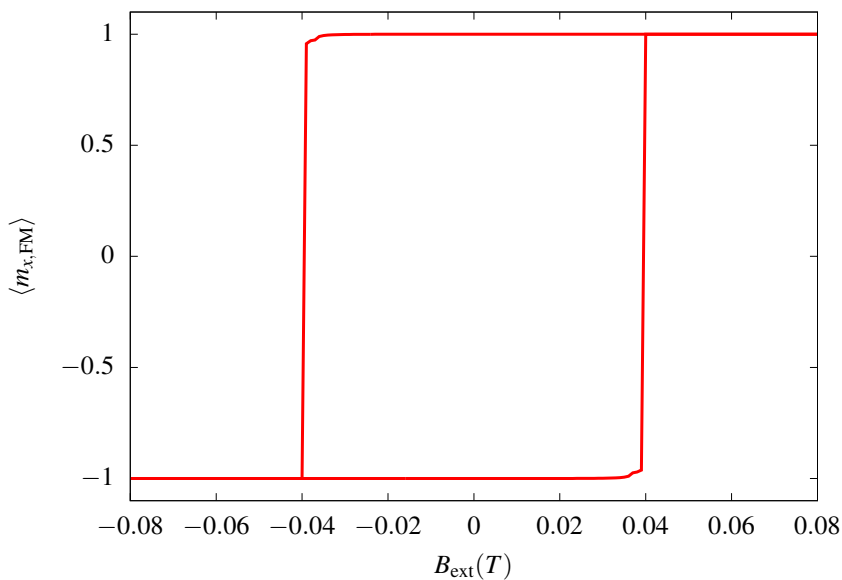


Figure C.3: Hysteresis loop, produced by using this example code.

IMPLEMENTATION OF BIAXIAL ANISOTROPY

Although biaxial anisotropy is not natively implemented in MuMax³, it can be included by adding a custom field and corresponding custom energy term. The biaxial anisotropy energy density is given by

$$\epsilon_K = K_c (\mathbf{c}_1 \cdot \mathbf{m})^2 (\mathbf{c}_2 \cdot \mathbf{m})^2 \quad (\text{D.1})$$

$$= K_c \cos^2(\beta) \sin^2(\beta) \quad (\text{D.2})$$

where K_c is the biaxial anisotropy constant, \mathbf{c}_1 and \mathbf{c}_2 are the *normalised* biaxial anisotropy axes and β is the angle that the normalised magnetisation vector \mathbf{m} makes with respect to \mathbf{c}_1 .

If we take e.g. \mathbf{c}_1 and \mathbf{c}_2 along the x and y direction of the simulation box respectively, then one can add following code to the MuMax³ input script

```

c1 := Constvector(1,0,0)
c2 := Constvector(0,1,0)
f := Const (-2 * Kc / (M_FM))
B_c := Mul(f, Madd(Mul( Mul(Mul( Dot(c2, m)
, Dot(c2, m)), Dot(c1, m)), c1)
, Mul( Mul(Mul( Dot(c1, m)
, Dot(c1, m)), Dot(c2, m)), c2), 1,1))
AddFieldTerm(B_c)
AddEdensTerm(Mul( Mul( Const(-0.25), Const(M_FM) ), Dot(M, B_c) ))

```

to implement this biaxial anisotropy. Note that in this case the maximal energy density is obtained for $\epsilon_K = \frac{K_c}{4}$ at the angle $\beta = \frac{\pi}{4}$.

SPIN FLOP COUPLING FOR A BIAxIAL AFM

In this section, we will show that the expression for the spin flop coupling in an antiferromagnet with biaxial anisotropy, is the same for uniaxial antiferromagnets (after Hoffmann training). Assuming that the 2 antiferromagnetic macrospins are in an almost antiparallel position, one can define the surface energy density σ_{AFM} as

$$\begin{aligned} \sigma_{\text{AFM}} = & -J_{\text{I}} \cos\left(\frac{3\pi}{4} - \theta - \beta\right) - J_{\text{I}} \cos\left(\frac{\pi}{4} - \phi + \beta\right) - \delta t_{\text{AFM}} \cos(\theta + \phi) \\ & - \frac{K_{\text{c,AFM}} t_{\text{AFM}}}{4} \sin^2\left(2\theta + \frac{3\pi}{2}\right) - \frac{K_{\text{c,AFM}} t_{\text{AFM}}}{4} \sin^2\left(2\phi + \frac{\pi}{2}\right) \end{aligned}$$

The definitions of the angles θ , ϕ , γ and β are shown in figure E.1.

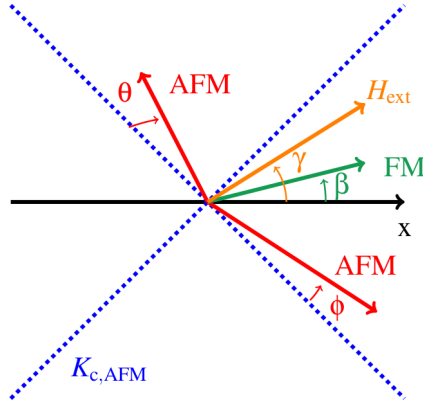


Figure E.1: Definition of the AFM canting angles θ and ϕ , the FM angle β and the angle γ of the external field H_{ext} .

Using the small canting angle approximation, one finds that

$$\begin{aligned}\sigma_{\text{AFM}} = & -J_{\text{I}} \left[1 - \frac{\theta^2}{2} \right] \cos \left(\frac{3\pi}{4} - \beta \right) - J_{\text{I}} \theta \sin \left(\frac{3\pi}{4} - \beta \right) \\ & - J_{\text{I}} \left[1 - \frac{\phi^2}{2} \right] \cos \left(\frac{\pi}{4} + \beta \right) - J_{\text{I}} \phi \sin \left(\frac{\pi}{4} + \beta \right) \\ & + \frac{\delta t_{\text{AFM}}}{2} (\theta + \phi)^2 + K_{\text{c,AFM}} t_{\text{AFM}} (\theta^2 + \phi^2)\end{aligned}$$

while dropping constant energy terms. By minimizing the energy density σ_{AFM} towards the AFM angles θ and ϕ , and eliminating θ^* from the ϕ^* equation and vice versa, one obtains

$$\begin{aligned}\theta^*(\beta) &= \frac{J_{\text{I}} \sin \left(\frac{\pi}{4} + \beta \right) [2K_{\text{c,AFM}} t_{\text{AFM}} + J_{\text{I}} \cos \left(\frac{\pi}{4} + \beta \right)]}{4K_{\text{c,AFM}}^2 t_{\text{AFM}}^2 + 4t_{\text{AFM}}^2 K_{\text{c,A}} \delta - J_{\text{I}}^2 \cos^2 \left(\frac{\pi}{4} + \beta \right)} \\ \phi^*(\beta) &= \frac{J_{\text{I}} \sin \left(\frac{\pi}{4} + \beta \right) [2K_{\text{c,AFM}} t_{\text{AFM}} - J_{\text{I}} \cos \left(\frac{\pi}{4} + \beta \right)]}{4K_{\text{c,AFM}}^2 t_{\text{AFM}}^2 + 4t_{\text{AFM}}^2 K_{\text{c,AFM}} \delta - J_{\text{I}}^2 \cos^2 \left(\frac{\pi}{4} + \beta \right)}\end{aligned}$$

Resubstituting these expressions in the energy density and retaining the lowest order approximation, one finally obtains that

$$\sigma_{\text{AFM}}(\beta) = \left[\frac{J_{\text{I}}^2}{2t_{\text{AFM}} (K_{\text{c,AFM}} + \delta)} \right] \cos^2 \left(\frac{\pi}{4} + \beta \right)$$

This equation formally looks the same as the one for an antiferromagnet with uniaxial anisotropy, but with the easy axis rotated over 45° . The energy is minimal for $\beta^* = \frac{\pi}{4}$ or $\frac{5\pi}{4}$ and the hysteresis loops of the FM layer are analogous to the ones as defined in the Stoner Wohlfarth model, but with an anisotropy axis rotated over 45° with respect to the direction of the external field. Thus the switching field B_{c} is reduced by a factor 2 for $\gamma = 0$, i.e.

$$B_{\text{c}} = \left[\frac{J_{\text{I}}^2}{2M_{\text{FM}} t_{\text{FM}} t_{\text{AFM}} (K_{\text{c,AFM}} + \delta)} \right] \quad (\text{E.1})$$

neglecting the anisotropy of the ferromagnet.

EXCHANGE BIAS FOR A BIAXIAL COMPENSATED ANTIFERROMAGNET

Analogous to the calculation of the coercivity induced by spin flop coupling in an antiferromagnet with uniaxial anisotropy, one can calculate the exchange bias field for an antiferromagnet with a strong biaxial anisotropy and low coupling constant. In this case, the function $\sigma_{\text{AFM}}(\beta, \theta, \phi)$ is given by

$$\begin{aligned} \sigma_{\text{AFM}} = & -J_1 \cos\left(\frac{\pi}{4} + \theta - \beta\right) - J_1 \cos\left(\frac{\pi}{4} + \phi + \beta\right) \\ & - \delta t_{\text{AFM}} \cos\left(\theta + \phi - \frac{\pi}{2}\right) - \frac{K_{\text{c,AFM}} t_{\text{AFM}}}{4} \sin^2\left(2\theta + \frac{\pi}{2}\right) \\ & - \frac{K_{\text{c,AFM}} t_{\text{AFM}}}{4} \sin^2\left(2\phi + \frac{\pi}{2}\right) \end{aligned}$$

where we have defined the in-plane biaxial anisotropy as in section D, but rotated over 45° with respect to the x axis. The definition of the angles θ , ϕ , γ and β is shown in figure F.1.

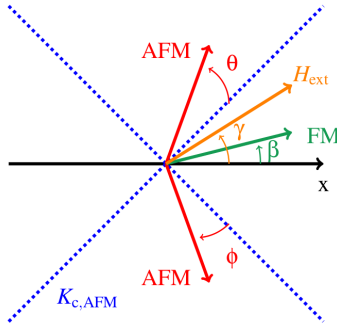


Figure F.1: Definition of the AFM canting angles θ and ϕ , the FM angle β and the angle γ of the external field H_{ext} .

Using the small canting angle approximation again, one finds that

$$\begin{aligned}\sigma_{\text{AFM}} = & -J_{\text{I}} \left[\cos \left(\frac{\pi}{4} - \beta \right) \left(1 - \frac{\theta^2}{2} \right) - \theta \sin \left(\frac{\pi}{4} - \beta \right) \right] \\ & - J_{\text{I}} \left[\cos \left(\frac{\pi}{4} + \beta \right) \left(1 - \frac{\phi^2}{2} \right) - \phi \sin \left(\frac{\pi}{4} + \beta \right) \right] \\ & - \delta t_{\text{AFM}} (\theta + \phi) - \frac{K_{\text{c,AFM}} t_{\text{AFM}}}{4} (1 - 4\theta^2) \\ & - \frac{K_{\text{c,AFM}} t_{\text{AFM}}}{4} (1 - 4\phi^2)\end{aligned}$$

Calculating the first derivative of σ_{AFM} towards θ and ϕ to minimize σ_{AFM} , one obtains

$$\phi^* = -\frac{J_{\text{I}} \sin \left(\frac{\pi}{4} + \beta \right) - \delta t_{\text{AFM}}}{2K_{\text{c,AFM}} t_{\text{AFM}} + J_{\text{I}} \cos \left(\frac{\pi}{4} + \beta \right)} \quad (\text{F.1})$$

$$\theta^* = -\frac{J_{\text{I}} \sin \left(\frac{\pi}{4} - \beta \right) - \delta t_{\text{AFM}}}{2K_{\text{c,AFM}} t_{\text{AFM}} + J_{\text{I}} \cos \left(\frac{\pi}{4} - \beta \right)} \quad (\text{F.2})$$

and by resubstituting these 2 equation into σ_{AFM}

$$\sigma_{\text{AFM}}(\beta) = -\sqrt{2} J_{\text{I}} \cos(\beta) - \frac{1}{2} \left[\frac{(J_{\text{I}} \sin \left(\frac{\pi}{4} - \beta \right) - \delta t_{\text{AFM}})^2}{2K_{\text{c,AFM}} t_{\text{AFM}} + J_{\text{I}} \cos \left(\frac{\pi}{4} - \beta \right)} \right] \quad (\text{F.3})$$

$$- \frac{1}{2} \left[\frac{(J_{\text{I}} \sin \left(\frac{\pi}{4} + \beta \right) - \delta t_{\text{AFM}})^2}{2K_{\text{c,AFM}} t_{\text{AFM}} + J_{\text{I}} \cos \left(\frac{\pi}{4} + \beta \right)} \right] \quad (\text{F.4})$$

dropping constant terms. Neglecting the anisotropy in the FM, one can thus write the total effective surface energy density as

$$\sigma_{\text{eff}}(\beta) = -\mu_0 M_{\text{FM}} t_{\text{FM}} H_{\text{ext}} \cos(\gamma - \beta) - \sqrt{2} J_{\text{I}} \cos(\beta) \quad (\text{F.5})$$

$$- \frac{1}{2} \left[\frac{(J_{\text{I}} \sin \left(\frac{\pi}{4} - \beta \right) - \delta t_{\text{AFM}})^2}{2K_{\text{c,AFM}} t_{\text{AFM}} + J_{\text{I}} \cos \left(\frac{\pi}{4} - \beta \right)} \right] \quad (\text{F.6})$$

$$- \frac{1}{2} \left[\frac{(J_{\text{I}} \sin \left(\frac{\pi}{4} + \beta \right) - \delta t_{\text{AFM}})^2}{2K_{\text{c,AFM}} t_{\text{AFM}} + J_{\text{I}} \cos \left(\frac{\pi}{4} + \beta \right)} \right] \quad (\text{F.7})$$

For $\gamma = 0$, one finds after minimizing the effective surface energy density σ that $\beta^* = 0$ and $\beta^* = \pi$ are 2 extrema, representing the saturated states of the FM. Numerical analysis shows that there are no other extrema in our

parameter range.¹ This implicates that one cannot not define the bias field as $B_{\text{eb}} = B_{\text{ext}} (\langle m_{\text{FM},x} \rangle = 0)$. One finds that the solution $\beta^* = 0$ is stable for the magnetic field

$$\begin{aligned}
 B_1 \geq & -\frac{\sqrt{2}J_1}{M_{\text{FM}}t_{\text{FM}}} \\
 & + \frac{1}{M_{\text{FM}}t_{\text{FM}}} \left[\frac{J_1^2}{2K_{\text{c,AFM}}t_{\text{AFM}} + \frac{\sqrt{2}}{2}J_1} + 2 \frac{\left(\frac{\sqrt{2}}{2}J_1 - \delta t_{\text{AFM}}\right) J_1^2}{\left(2K_{\text{c,AFM}}t_{\text{AFM}} + \frac{\sqrt{2}}{2}J_1\right)^2} \right] \\
 & - \frac{1}{M_{\text{FM}}t_{\text{FM}}} \left[\frac{\left(\frac{\sqrt{2}}{2}J_1 - \delta t_{\text{AFM}}\right) J_1 \sqrt{2}}{2K_{\text{c,AFM}}t_{\text{AFM}} + \frac{\sqrt{2}}{2}J_1} - \frac{\left(\frac{\sqrt{2}}{2}J_1 - \delta t_{\text{AFM}}\right)^2 J_1^2}{\left(2K_{\text{c,AFM}}t_{\text{AFM}} + \frac{\sqrt{2}}{2}J_1\right)^3} \right] \\
 & + \frac{1}{2M_{\text{FM}}t_{\text{FM}}} \frac{\left(\frac{\sqrt{2}}{2}J_1 - \delta t_{\text{AFM}}\right)^2 J_1 \sqrt{2}}{\left(2K_{\text{c,AFM}}t_{\text{AFM}} + \frac{\sqrt{2}}{2}J_1\right)^2}
 \end{aligned}$$

and $\beta^* = \pi$ is stable for

$$\begin{aligned}
 B_2 \leq & -\frac{\sqrt{2}J_1}{M_{\text{FM}}t_{\text{FM}}} \\
 & + \frac{1}{M_{\text{FM}}t_{\text{FM}}} \left[-\frac{J_1^2}{2K_{\text{c,AFM}}t_{\text{AFM}} - \frac{\sqrt{2}}{2}J_1} + 2 \frac{\left(\frac{\sqrt{2}}{2}J_1 + \delta t_{\text{AFM}}\right) J_1^2}{\left(2K_{\text{c,AFM}}t_{\text{AFM}} - \frac{\sqrt{2}}{2}J_1\right)^2} \right] \\
 & + \frac{1}{M_{\text{FM}}t_{\text{FM}}} \left[\frac{\left(\frac{\sqrt{2}}{2}J_1 + \delta t_{\text{AFM}}\right) J_1 \sqrt{2}}{2K_{\text{c,AFM}}t_{\text{AFM}} - \frac{\sqrt{2}}{2}J_1} - \frac{\left(\frac{\sqrt{2}}{2}J_1 + \delta t_{\text{AFM}}\right)^2 J_1^2}{\left(2K_{\text{c,AFM}}t_{\text{AFM}} - \frac{\sqrt{2}}{2}J_1\right)^3} \right] \\
 & + \frac{1}{2M_{\text{FM}}t_{\text{FM}}} \frac{\left(\frac{\sqrt{2}}{2}J_1 + \delta t_{\text{AFM}}\right)^2 J_1 \sqrt{2}}{\left(2K_{\text{c,AFM}}t_{\text{AFM}} - \frac{\sqrt{2}}{2}J_1\right)^2}
 \end{aligned}$$

Using the symmetry of the hysteresis loop, one can define the exchange bias field B_{eb} as the shift of the hysteresis loop, determined by $B_{\text{eb}} = \frac{B_1+B_2}{2}$. Keeping the parameters $K_{\text{c,AFM}}$ and δ fixed, one can plot the bias field B_{eb}

¹In the case of higher coupling constants J_1 , there is a breakdown of our small canting angle approximation as can be seen in figure 4.12.

as a function of the coupling parameter J_I . An example is shown in figure 4.16 for $k = 5$. For a very high anisotropy $K_{c,AFM}$, the bias field is reduced to that of 2 uncompensated spins, making an angle of 45° with the field cooling direction.

Numerical analysis of the effective surface energy density $\sigma(\beta)$ shows that there is a region in which both the solutions $\beta = 0$ and $\beta = \pi$ are stable (see figure F.2), which results in a small coercivity B_c , given by

$$B_c = \frac{B_1 - B_2}{2} = \frac{256 t_{AFM} J_I^6 \left(K_{c,AFM} + \frac{\delta}{4} - \frac{4 K_{c,AFM}^3 t_{AFM}^2}{J_I^2} \right) \left(\frac{4 K_{c,AFM} \delta t_{AFM}^2}{J_I^2} + 1 \right)}{M_{FM} t_{FM} \left(\sqrt{2} J_I - 4 K_{c,AFM} t_{AFM} \right)^3 \left(\sqrt{2} J_I + 4 K_{c,AFM} t_{AFM} \right)^3}$$

as there are no other energy minima in our parameter range.

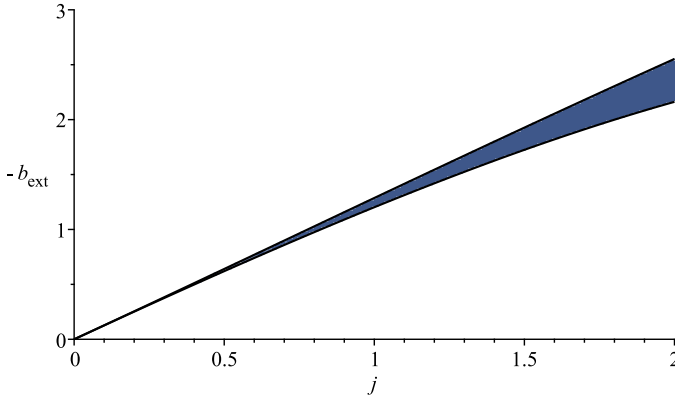


Figure F.2: The 2 critical stability curves (black lines) determined by $\left(\frac{\partial^2 \sigma}{\partial \beta^2} \right) = 0$ for $\beta^* = 0$ and $\beta^* = \pi$ with $k = 5$ (reduced units). Blue area shows the stability overlap. Remark that a breakdown of the low canting angle approximation happens around $j = 1.5$ as shown in figure 4.16.

An example of the surface energy density for $j = 1$, $k = 5$ and external field $b_{ext} = -1.25$ is shown in figure F.3. One can clearly see that, for these parameters, both the solutions $\beta^* = 0$ and $\beta^* = \pi$ are stable. For low coupling constants J_I , one finds that $B_c \ll B_{cb}$, as expected. At breakdown of the low canting angle approximation ($j \approx 1.5$) we obtain that $B_c \approx 5\%$ of B_{cb} for $k = 5$. The coercivity b_c as a function of the coupling constant j is shown in figure F.4.

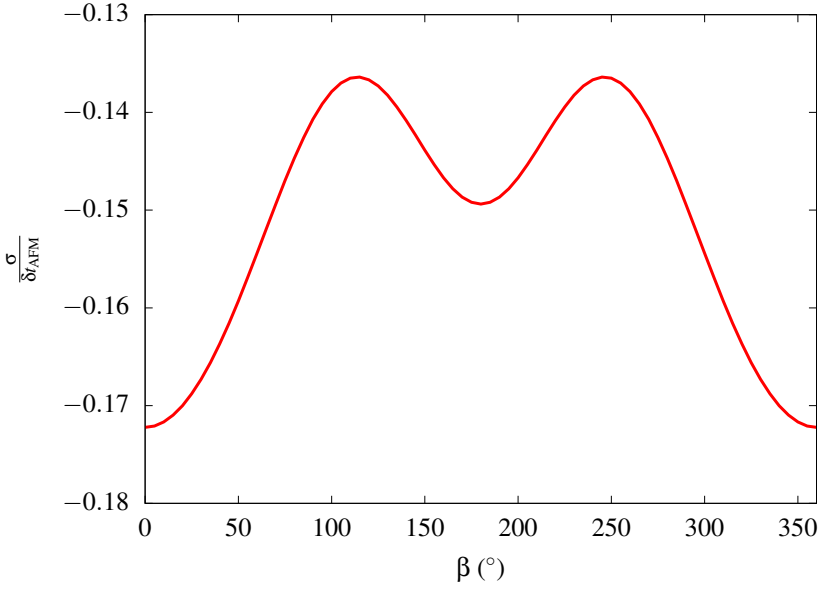


Figure F.3: Reduced surface energy density $\frac{\sigma}{\delta_{AFM}}$ as a function of the FM angle β for the parameters $j = 1$, $k = 5$ and external field $b_{\text{ext}} = -1.25$. Two minima are present $\beta^* = 0$ and $\beta^* = \pi$ in the region of stability overlap. This leads to a finite coercivity, in correspondence to figure F.2.

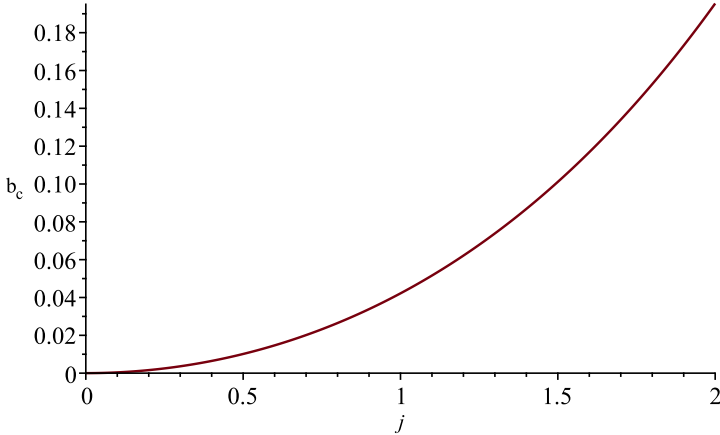


Figure F.4: Coercivity b_c as function of the coupling constant j for $k = 5$ (reduced units).

SPIN FLIP IN A UNIAXIAL COMPENSATED AFM

We will show that, if the 2 AFM sublattices point in the same anisotropy *direction* and if the canting angles are small, they have to coincide, i.e. $\theta = \phi$. The definitions of the angles are shown in figure G.1.

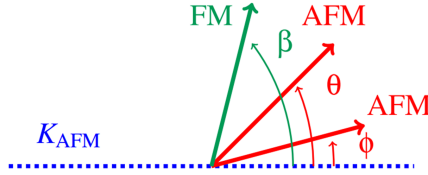


Figure G.1: Definitions of the AFM angles θ and ϕ and the FM angle β .

The surface energy density σ_{AFM} , attributed to the antiferromagnet and the interface interaction, is now given by

$$\begin{aligned} \sigma_{\text{AFM}}(\phi, \theta, \beta) &= -J_{\text{I}} \cos(\beta - \theta) - J_{\text{I}} \cos(\beta - \phi) + \delta t_{\text{AFM}} \cos(\theta - \phi) \\ &\quad - K_{\text{AFM}} t_{\text{AFM}} (\cos^2(\theta) + \cos^2(\phi)) \\ &\approx -J_{\text{I}} \left(1 - \frac{\theta^2}{2}\right) \cos(\beta) - J_{\text{I}} \left(1 - \frac{\phi^2}{2}\right) \cos(\beta) \\ &\quad - J_{\text{I}} (\theta + \phi) \sin(\beta) + K_{\text{AFM}} t_{\text{AFM}} (\theta^2 + \phi^2) \\ &\quad - \delta t_{\text{AFM}} \frac{(\theta - \phi)^2}{2} \end{aligned}$$

Calculating the first derivatives towards θ and ϕ to minimize the energy density, we find that

$$\begin{aligned} \frac{\partial \sigma_{\text{AFM}}}{\partial \theta} &= J_{\text{I}} \theta^* \cos(\beta) - J_{\text{I}} \sin(\beta) + 2K_{\text{AFM}} t_{\text{AFM}} \theta^* - \delta t_{\text{AFM}} (\theta^* - \phi^*) = 0 \\ \frac{\partial \sigma_{\text{AFM}}}{\partial \phi} &= J_{\text{I}} \phi^* \cos(\beta) - J_{\text{I}} \sin(\beta) + 2K_{\text{AFM}} t_{\text{AFM}} \phi^* + \delta t_{\text{AFM}} (\theta^* - \phi^*) = 0 \end{aligned}$$

and so we find that

$$\theta^* = \phi^* = \frac{J_I \sin(\beta)}{J_I \cos(\beta) + 2K_{\text{AFM}} t_{\text{AFM}}} \quad (\text{G.1})$$

This shows that the 2 AFM sublattices have to coincide in the case of a large magnetocrystalline anisotropy and that the canting angles are independent of the interlayer interaction parameter δ .

EXCHANGE BIAS INDUCED BY UNEQUAL COUPLING STRENGTHS IN A COMPENSATED AFM

We will show that exchange bias is produced as a first order effect if the 2 AFM sublattices couple with different coupling strengths towards the ferromagnetic layer. The surface energy density σ_{AFM} is given by

$$\begin{aligned} \sigma_{\text{AFM}}(\beta, \phi, \theta) = & -J_{\text{I},\theta} \cos(\beta - \theta) + J_{\text{I},\phi} \cos(\beta + \phi) \\ & - K_{\text{AFM}} t_{\text{AFM}} [\cos^2(\theta) + \cos^2(\phi)] \\ & - \delta t_{\text{AFM}} \cos(\theta + \phi) \end{aligned} \quad (\text{H.1})$$

The definition of the FM angle β and the AFM canting angles θ and ϕ is shown in figure H.1.

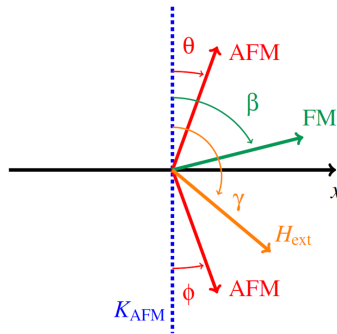


Figure H.1: Definition of the AFM canting angles θ and ϕ , the FM angle β and the angle γ of the external field H_{ext} with respect to the AFM uniaxial anisotropy axis K_{AFM} .

Using the small canting approximation, minimizing the surface energy density σ_{AFM} (analogous to section 4.2) and eliminating θ^* from the ϕ^* equation and vice versa, we find

$$\theta^* = \frac{\sin(\beta) [-J_{1,\theta}J_{1,\phi} \cos(\beta) + (J_{1,\theta} - J_{1,\phi}) \delta t_{\text{AFM}} + 2J_{1,\theta}K_{\text{AFM}}t_{\text{AFM}}]}{-J_{1,\theta}J_{1,\phi} \cos^2(\beta) + (2K_{\text{AFM}} + \delta) (J_{1,\theta} - J_{1,\phi}) t_{\text{AFM}} \cos(\beta) + \tau}$$

$$\phi^* = \frac{\sin(\beta) [J_{1,\theta}J_{1,\phi} \cos(\beta) - (J_{1,\theta} - J_{1,\phi}) \delta t_{\text{AFM}} + 2J_{1,\phi}K_{\text{AFM}}t_{\text{AFM}}]}{-J_{1,\theta}J_{1,\phi} \cos^2(\beta) + (2K_{\text{AFM}} + \delta) (J_{1,\theta} - J_{1,\phi}) t_{\text{AFM}} \cos(\beta) + \tau}$$

where we have defined $\tau = t_{\text{AFM}}^2 (2K_{\text{AFM}} + \delta)^2 - \delta^2 t_{\text{AFM}}^2$. One can easily see that these equations reduce to expressions 4.6 in case $J_{1,\theta} = J_{1,\phi} = J_1$. After lengthy calculations, one can show that the effective AFM surface energy density is given by

$$\sigma_{\text{AFM}}(\beta) = - (J_{1,\theta} - J_{1,\phi}) \cos(\beta) + \Lambda \quad (\text{H.2})$$

It is clear that the first energy term induces exchange bias in the FM layer as a result of the unequal coupling strengths of the sublattices towards the ferromagnet. The higher order terms Λ are given by

$$\begin{aligned} \Lambda = & - (J_{1,\theta} - J_{1,\phi}) \cos(\beta) [J_{1,\theta}J_{1,\phi} \cos(\beta) - (J_{1,\theta} - J_{1,\phi}) (2K_{\text{AFM}} + \delta) t_{\text{AFM}}]^2 \lambda \\ & + 4K_{\text{AFM}}t_{\text{AFM}} [J_{1,\theta}^2J_{1,\phi}^2 \cos^2(\beta) + (J_{1,\theta} - J_{1,\phi})^2 (2K_{\text{AFM}} + \delta)^2 t_{\text{AFM}}^2] \lambda \\ & + 8K_{\text{AFM}}^2 t_{\text{AFM}}^3 (J_{1,\theta} - J_{1,\phi})^2 (K_{\text{AFM}} + \delta) \lambda \\ & - 16K_{\text{AFM}}^2 t_{\text{AFM}}^3 J_{1,\theta}J_{1,\phi} (K_{\text{AFM}} + \delta) \lambda \\ & - J_{1,\theta}J_{1,\phi} \cos(\beta) (J_{1,\theta} - J_{1,\phi}) K_{\text{AFM}}t_{\text{AFM}} \lambda \\ & + 2 (J_{1,\theta} - J_{1,\phi})^2 (2K_{\text{AFM}} + \delta)^2 t_{\text{AFM}}^2 \lambda \end{aligned}$$

with

$$\lambda = \frac{\sin^2(\beta)}{2 [-J_{1,\theta}J_{1,\phi} \cos^2(\beta) + (2K_{\text{AFM}} + \delta) (J_{1,\theta} - J_{1,\phi}) t_{\text{AFM}} \cos(\beta) + \tau]^2}$$

One can easily check that equation H.2 reduces to equation 4.8 in the case that $J_{1,\theta} = J_{1,\phi} = J_1$.

Bibliography

- [1] Jonas De Clercq, Arne Vansteenkiste, Medjid Abes, Kristiaan Temst, and Bartel Van Waeyenberge. Modelling exchange bias with mumax3. *Journal of Physics D: Applied Physics*, 49(43):435001, 2016.
- [2] Jonas De Clercq, Jonathan Leliaert, and Bartel Van Waeyenberge. Modelling compensated antiferromagnetic interfaces with mumax3. *Journal of Physics D: Applied Physics*, arXiv 0712.0157, 2017.
- [3] John MD Coey. *Magnetism and magnetic materials*. Cambridge University Press, 2010.
- [4] Warren E. Henry. Spin paramagnetism of cr^{+++} , fe^{+++} , and gd^{+++} at liquid helium temperatures and in strong magnetic fields. *Phys. Rev.*, 88:559–562, Nov 1952.
- [5] Peter Mohn. *Magnetism in the solid state: an introduction*, volume 134. Springer Science & Business Media, 2006.
- [6] LALE Landau and Es Lifshitz. On the theory of the dispersion of magnetic permeability in ferromagnetic bodies. *Phys. Z. Sowjetunion*, 8(153):101–114, 1935.
- [7] Bernard Dieny, Ronald B Goldfarb, and Kyung-Jin Lee. *Introduction to magnetic random-access memory*. John Wiley & Sons, 2016.
- [8] John David Jackson. *Classical electrodynamics*. Wiley, New York, NY, 3rd ed. edition, 1999.
- [9] William Fuller Brown. Theory of the approach to magnetic saturation. *Phys. Rev.*, 58:736–743, Oct 1940.
- [10] E. C. Stoner and E. P. Wohlfarth. A mechanism of magnetic hysteresis in heterogeneous alloys. *Philosophical Transactions of the Royal Society of London A: Mathematical, Physical and Engineering Sciences*, 240(826):599–642, 1948.

- [11] Amikam Aharoni. *Introduction to the Theory of Ferromagnetism*, volume 109. Clarendon Press, 2000.
- [12] Arne Vansteenkiste, Jonathan Leliaert, Mykola Dvornik, Mathias Helsen, Felipe Garcia-Sanchez, and Bartel Van Waeyenberge. The design and verification of mumax3. *AIP Advances*, 4(10):107133, 2014.
- [13] A. Vansteenkiste and B. Van de Wiele. Mumax: A new high-performance micromagnetic simulation tool. *Journal of Magnetism and Magnetic Materials*, 323(21):2585 – 2591, 2011.
- [14] W. H. Meiklejohn and C. P. Bean. New magnetic anisotropy. *Phys. Rev.*, 102:1413–1414, Jun 1956.
- [15] D. L. Mills. Surface spin-flop state in a simple antiferromagnet. *Phys. Rev. Lett.*, 20:18–21, Jan 1968.
- [16] Fritz Herlach and Noboru Miura. *High Magnetic Fields: Science and Technology Volume 3: Theory and Experiments II*, p. 138. World Scientific, 2006.
- [17] Rong-Gen Cai and Run-Qiu Yang. Holographic model for the paramagnetism/antiferromagnetism phase transition. *Phys. Rev. D*, 91:086001, Apr 2015.
- [18] Igor A. Zaliznyak. *Spin Structures and Spin Wave Excitations*. John Wiley and Sons, Ltd, 2007.
- [19] W. H. Meiklejohn and C. P. Bean. New magnetic anisotropy. *Phys. Rev.*, 105:904–913, Feb 1957.
- [20] Florin Radu and Hartmut Zabel. *Exchange Bias Effect of Ferro-/Antiferromagnetic Heterostructures*, pages 97–184. Springer Berlin Heidelberg, Berlin, Heidelberg, 2008.
- [21] D. Mauri, H. C. Siegmann, P. S. Bagus, and E. Kay. Simple model for thin ferromagnetic films exchange coupled to an antiferromagnetic substrate. *Journal of Applied Physics*, 62(7):3047–3049, 1987.
- [22] A Scholl, M Liberati, E Arenholz, H Ohldag, and J Stöhr. Creation of an antiferromagnetic exchange spring. *Physical review letters*, 92(24):247201, 2004.

- [23] A. P. Malozemoff. Random-field model of exchange anisotropy at rough ferromagnetic-antiferromagnetic interfaces. *Phys. Rev. B*, 35:3679–3682, Mar 1987.
- [24] R Coehoorn, J.T Kohlhepp, R.M Jungblut, A Reinders, and M.J Dekker. Mesoscopic magnetism and the phenomenon of exchange anisotropy: Mbe grown cu(110)/ni80fe20/fe50mn50 bilayers with corrugated interfaces. *Physica B: Condensed Matter*, 319(1):141 – 167, 2002.
- [25] P. Miltényi, M. Gierlings, M. Bamming, U. May, G. Güntherodt, J. Nogués, M. Gruyters, C. Leighton, and Ivan K. Schuller. Tuning exchange bias. *Applied Physics Letters*, 75(15):2304–2306, 1999.
- [26] Tôru Moriya. Anisotropic superexchange interaction and weak ferromagnetism. *Phys. Rev.*, 120:91–98, Oct 1960.
- [27] Shuai Dong, Qinfang Zhang, Seiji Yunoki, J.-M. Liu, and Elbio Dagotto. Ab initio. *Phys. Rev. B*, 84:224437, Dec 2011.
- [28] R. Yanes, J. Jackson, L. Udvardi, L. Szunyogh, and U. Nowak. Exchange bias driven by dzyaloshinskii-moriya interactions. *Phys. Rev. Lett.*, 111:217202, Nov 2013.
- [29] Shuai Dong, Kunihiko Yamauchi, Seiji Yunoki, Rong Yu, Shuhua Liang, Adriana Moreo, J.-M. Liu, Silvia Picozzi, and Elbio Dagotto. Exchange bias driven by the dzyaloshinskii-moriya interaction and ferroelectric polarization at *g*-type antiferromagnetic perovskite interfaces. *Phys. Rev. Lett.*, 103:127201, Sep 2009.
- [30] S. J. Zhu, J. Yuan, B. Y. Zhu, F. C. Zhang, B. Xu, L. X. Cao, X. G. Qiu, B. R. Zhao, and P. X. Zhang. Exchange bias effect and enhanced magnetoresistance in la_{0.67}sr_{0.33}mno₃-srtio₃ superlattices. *Applied Physics Letters*, 90(11):112502, 2007.
- [31] W. Thomson. On the electro-dynamic qualities of metals:—effects of magnetization on the electric conductivity of nickel and of iron. *Proceedings of the Royal Society of London*, 8:546–550, 1856.
- [32] M. N. Baibich, J. M. Broto, A. Fert, F. Nguyen Van Dau, F. Petroff, P. Etienne, G. Creuzet, A. Friederich, and J. Chazelas. Giant magnetoresistance of (001)fe/(001)cr magnetic superlattices. *Phys. Rev. Lett.*, 61:2472–2475, Nov 1988.

- [33] G. Binasch, P. Grünberg, F. Saurenbach, and W. Zinn. Enhanced magnetoresistance in layered magnetic structures with antiferromagnetic interlayer exchange. *Phys. Rev. B*, 39:4828–4830, Mar 1989.
- [34] Mathias Getzlaff. *Fundamentals of magnetism*. Springer Science & Business Media, 2007.
- [35] N. F. Mott. Electrons in transition metals. *Advances in Physics*, 13:325–422, July 1964.
- [36] Pablo Merodio Camara. *Spin dependent transport in antiferro and ferrimagnetic nanostructures*. Theses, Université Grenoble Alpes, December 2014.
- [37] M. Julliere. Tunneling between ferromagnetic films. *Physics Letters A*, 54:225–226, September 1975.
- [38] H.J.M. Swagten. Chapter one spin-dependent tunneling in magnetic junctions. volume 17 of *Handbook of Magnetic Materials*, pages 1 – 121. Elsevier, 2007.
- [39] Y. M. Lee, J. Hayakawa, S. Ikeda, F. Matsukura, and H. Ohno. Effect of electrode composition on the tunnel magnetoresistance of pseudo-spin-valve magnetic tunnel junction with a mgo tunnel barrier. *Applied Physics Letters*, 90(21):212507, 2007.
- [40] Evgeny Y Tsymbal and Igor Zutic. *Handbook of Spin Transport and Magnetism*. CRC Press, 2011.
- [41] Elby Titus, Rahul Krishna, José Grácio, Manoj Singh, Antonio Luis Ferreira, and Ricardo G Dias. Carbon nanotube based magnetic tunnel junctions (mtjs) for spintronics application. In Jose Mauricio Marulanda, editor, *Electronic Properties of Carbon Nanotubes*, chapter 23. InTech, Rijeka, 2011.
- [42] L. Berger. Emission of spin waves by a magnetic multilayer traversed by a current. *Phys. Rev. B*, 54:9353–9358, Oct 1996.
- [43] J.C. Slonczewski. Current-driven excitation of magnetic multilayers. *Journal of Magnetism and Magnetic Materials*, 159(1):L1 – L7, 1996.

- [44] J. J. Nowak, R. P. Robertazzi, J. Z. Sun, G. Hu, J. H. Park, J. Lee, A. J. Annunziata, G. P. Lauer, R. Kothandaraman, E. J. O'Sullivan, P. L. Trouilloud, Y. Kim, and D. C. Worledge. Dependence of voltage and size on write error rates in spin-transfer torque magnetic random-access memory. *IEEE Magnetics Letters*, 7:1–4, 2016.
- [45] E Albisetti, D Petti, M Pancaldi, M Madami, S Tacchi, J Curtis, WP King, A Papp, G Csaba, W Porod, et al. Nanopatterning reconfigurable magnetic landscapes via thermally assisted scanning probe lithography. *Nature nanotechnology*, 2016.
- [46] Zhongqing Wei, Debin Wang, Suenne Kim, Soo-Young Kim, Yike Hu, Michael K Yakes, Arnaldo R Laracuente, Zhenting Dai, Seth R Marder, Claire Berger, et al. Nanoscale tunable reduction of graphene oxide for graphene electronics. *Science*, 328(5984):1373–1376, 2010.
- [47] Vassil Skumryev, Stoyan Stoyanov, Yong Zhang, George Hadji-panayis, et al. Beating the superparamagnetic limit with exchange bias. *nature*, 423(6942):850, 2003.
- [48] J Sort, F Garcia, S Auffret, B Rodmacq, B Dieny, V Langlais, S Suriñach, JS Muñoz, MD Baró, and J Nogués. Using exchange bias to extend the temperature range of square loop behavior in [pt/co] multilayers with perpendicular anisotropy. *Applied Physics Letters*, 87(24):242504, 2005.
- [49] Yayoi Takamura, Erik Folven, Jonathan B. R. Shu, Karl R. Lukes, Binzhi Li, Andreas Scholl, Anthony T. Young, Scott T. Retterer, Thomas Tybell, and Jostein K. Grepstad. Spin-flop coupling and exchange bias in embedded complex oxide micromagnets. *Phys. Rev. Lett.*, 111:107201, Sep 2013.
- [50] E. Folven, J. Linder, O. V. Gomonay, A. Scholl, A. Doran, A. T. Young, S. T. Retterer, V. K. Malik, T. Tybell, Y. Takamura, and J. K. Grepstad. Controlling the switching field in nanomagnets by means of domain-engineered antiferromagnets. *Phys. Rev. B*, 92:094421, Sep 2015.
- [51] Richard FL Evans, Weijia J Fan, Phanwadee Chureemart, Thomas A Ostler, Matthew OA Ellis, and Roy W Chantrell. Atomistic spin

- model simulations of magnetic nanomaterials. *Journal of Physics: Condensed Matter*, 26(10):103202, 2014.
- [52] M. J. Donahue and D. G. Porter. OOMMF-computer code, <http://math.nist.gov/oommf>.
- [53] T. Fischbacher, M. Franchin, G. Bordignon, and H. Fangohr. A systematic approach to multiphysics extensions of finite-element-based micromagnetic simulations: Nmag. *IEEE Transactions on Magnetics*, 43(6):2896–2898, June 2007.
- [54] Jonathan Leliaert, Ben Van de Wiele, Arne Vansteenkiste, Lasse Laurson, Gianfranco Durin, Luc Dupré, and Bartel Van Waeyenberge. Current-driven domain wall mobility in polycrystalline permalloy nanowires: A numerical study. *Journal of Applied Physics*, 115(23):233903, 2014.
- [55] Miguel Kiwi. Exchange bias theory. *Journal of Magnetism and Magnetic Materials*, 234(3):584–595, 2001.
- [56] H. Ohldag, A. Scholl, F. Nolting, E. Arenholz, S. Maat, A. T. Young, M. Carey, and J. Stöhr. Correlation between exchange bias and pinned interfacial spins. *Phys. Rev. Lett.*, 91:017203, Jul 2003.
- [57] Lamberto Duò, Marco Finazzi, and Franco Ciccacci. *Magnetic Properties of Antiferromagnetic Oxide Materials: Surfaces, Interfaces, and Thin Films*. John Wiley & Sons, 2010.
- [58] T. C. Schulthess and W. H. Butler. Consequences of spin-flop coupling in exchange biased films. *Phys. Rev. Lett.*, 81:4516–4519, Nov 1998.
- [59] Julian Dean, Andras Kovacs, Amit Kohn, A. Goncharov, M. A. Bashir, G. Hrkac, D. A. Allwood, and Thomas Schrefl. Exchange bias interactions in polycrystalline/amorphous bilayers. *Applied Physics Letters*, 96(7):072504, 2010.
- [60] Thiago Dias, E Menéndez, Haoliang Liu, Christian Van Haesendonck, André Vantomme, Kristiaan Temst, Joao Edgar Schmidt, Raquel Giulian, and J Geshev. Rotatable anisotropy driven training effects in exchange biased co/coo films. *Journal of Applied Physics*, 115(24):243903, 2014.

- [61] Himanshu Fulara, Sujeet Chaudhary, and Subhash C. Kashyap. Influence of strong anisotropy of coFe layer on the reversal asymmetry and training effect in Ir₂₂Mn₇₈/Co₆₀Fe₄₀ bilayers. *Journal of Applied Physics*, 113(4):043914, 2013.
- [62] Himanshu Fulara, Sujeet Chaudhary, and Subhash C. Kashyap. Interdependence of reversal asymmetry and training effect in Ir₂₂Mn₇₈/Ni₈₁Fe₁₉ bilayers probed with magnetoresistance. *Applied Physics Letters*, 101(14):142408, 2012.
- [63] Christian Binck. Training of the exchange-bias effect: A simple analytic approach. *Phys. Rev. B*, 70:014421, Jul 2004.
- [64] Himanshu Fulara, Sujeet Chaudhary, and Subhash C. Kashyap. Influence of strong anisotropy of coFe layer on the reversal asymmetry and training effect in Ir₂₂Mn₇₈/Co₆₀Fe₄₀ bilayers. *Journal of Applied Physics*, 113(4), 2013.
- [65] J. Geshev. Analytical solutions for exchange bias and coercivity in ferromagnetic/antiferromagnetic bilayers. *Phys. Rev. B*, 62:5627–5633, Sep 2000.
- [66] R. Jungblut, R. Coehoorn, M. T. Johnson, J. van de Stegge, and A. Reinders. Orientational dependence of the exchange biasing in molecular-beam-epitaxy-grown Ni₈₀Fe₂₀/Fe₅₀Mn₅₀ bilayers (invited). *Journal of Applied Physics*, 75(10):6659–6664, 1994.
- [67] Cheng-Hsun-Tony Chang, Shin-Chen Chang, Jyh-Shen Tsay, and Yeong-Der Yao. Variation of blocking temperatures for exchange biased CoO/Co/Ge(100) films. *AIP Advances*, 6(5):056101, 2016.
- [68] L. Wee, R.L. Stamps, and R.E. Camley. Temperature dependence of domain-wall bias and coercivity. *Journal of Applied Physics*, 89(11):6913–6915, 2001.
- [69] Mannan Ali, Christopher H Marrows, M Al-Jawad, Bryan J Hickey, Arkajyoti Misra, Ulrich Nowak, and Klaus-Dieter Usadel. Antiferromagnetic layer thickness dependence of the IrMn/Co exchange-bias system. *Physical review B*, 68(21):214420, 2003.
- [70] J. Stohr and H.C. Siegmann. From fundamentals to nanoscale dynamics. *Springer Ser. Solid State Sci.* 152:820, 2006, Aug 2007.

- [71] V Baltz, A Manchon, M Tsoi, T Moriyama, T Ono, and Y Tserkovnyak. Antiferromagnetism: the next flagship magnetic order for spintronics? *arXiv preprint arXiv:1606.04284*, 2016.
- [72] F. Radu, M. Etzkorn, R. Siebrecht, T. Schmitte, K. Westerholt, and H. Zabel. Interfacial domain formation during magnetization reversal in exchange-biased coo/co bilayers. *Phys. Rev. B*, 67:134409, Apr 2003.
- [73] A Harres and J Geshev. A polycrystalline model for magnetic exchange bias. *Journal of Physics: Condensed Matter*, 24(32):326004, 2012.
- [74] J Wu, JS Park, W Kim, E Arenholz, M Liberati, A Scholl, YZ Wu, Chanyong Hwang, and ZQ Qiu. Direct measurement of rotatable and frozen coo spins in exchange bias system of coo/fe/ag (001). *Physical review letters*, 104(21):217204, 2010.
- [75] H Laidler, L Holloway, and K O’Grady. Crystallographic defects in coo thin film media: effect on interactions and magnetic viscosity. *Journal of Physics D: Applied Physics*, 35(6):512, 2002.
- [76] P. Dova, H. Laidler, K. O’Grady, M. F. Toney, and M. F. Doerner. Effects of stacking faults on magnetic viscosity in thin film magnetic recording media. *Journal of Applied Physics*, 85(5):2775–2781, 1999.
- [77] D. Le Roy, R. Morel, A. Brenac, S. Pouget, and L. Notin. Perpendicular magnetization in coo (111) layers induced by exchange interaction with ferromagnetic co and ni60cu40 nanoclusters. *Journal of Applied Physics*, 111(8):083901, 2012.
- [78] T Kosub, C Schubert, H Schletter, M Daniel, M Hietschold, V Neu, M Maret, D Makarov, and M Albrecht. Coercivity enhancement in exchange biased coo/co 3 pt bilayers. *Journal of Physics D: Applied Physics*, 44(1):015002, 2011.
- [79] M. Ali, C. H. Marrows, and B. J. Hickey. Onset of exchange bias in ultrathin antiferromagnetic layers. *Phys. Rev. B*, 67:172405, May 2003.

- [80] H. Ohldag, A. Scholl, F. Nolting, E. Arenholz, S. Maat, A. T. Young, M. Carey, and J. Stöhr. Correlation between exchange bias and pinned interfacial spins. *Phys. Rev. Lett.*, 91:017203, Jul 2003.
- [81] J Nogués and Ivan K Schuller. Exchange bias. *Journal of Magnetism and Magnetic Materials*, 192(2):203 – 232, 1999.
- [82] Steven Brems, Kristiaan Temst, and Chris Van Haesendonck. Origin of the training effect and asymmetry of the magnetization in polycrystalline exchange bias systems. *Phys. Rev. Lett.*, 99:067201, Aug 2007.
- [83] Steven Brems, Dieter Buntinx, Kristiaan Temst, Chris Van Haesendonck, Florin Radu, and Hartmut Zabel. Reversing the training effect in exchange biased CoO/Co bilayers. *Phys. Rev. Lett.*, 95:157202, Oct 2005.
- [84] Steven Brems, Alexander Volodin, Chris Van Haesendonck, and Kristiaan Temst. Magnetic force microscopy study of the training effect in polycrystalline co/coo bilayers. *Journal of Applied Physics*, 103(11):113912, 2008.
- [85] M. Kiwi, José Mejiá-López, R.D. Portugal, and R. Ramirez. Positive exchange bias model: Fe/fef₂ and fe/mnf₂ bilayers. *Solid State Communications*, 116(6):315 – 319, 2000.
- [86] Nguyen Nguyen Phuoc, Nguyen Phu Thuy, Nguyen Anh Tuan, Le Thanh Hung, Nguyen Trung Thanh, and Nguyen Thanh Nam. Coexistence of positive and negative exchange bias in crmn/co bilayers. *Journal of magnetism and magnetic materials*, 298(1):43–47, 2006.
- [87] Oleg Petravic, Zhi-Pan Li, Igor V Roshchin, M Viret, R Morales, X Batlle, and Ivan K Schuller. Bidomain state in exchange biased fe f₂/ni. *Applied Physics Letters*, 87(22):222509, 2005.
- [88] Hendrik Ohldag, Hongtao Shi, Elke Arenholz, Joachim Stöhr, and David Lederman. Parallel versus antiparallel interfacial coupling in exchange biased Co/fe_f₂. *Phys. Rev. Lett.*, 96:027203, Jan 2006.

- [89] C Leighton, J Nogués, BJ Jönsson-Åkerman, and Ivan K Schuller. Coercivity enhancement in exchange biased systems driven by interfacial magnetic frustration. *Physical review letters*, 84(15):3466, 2000.
- [90] Nguyen Nguyen Phuoc, Nguyen Phu Thuy, Nguyen Anh Tuan, Le Thanh Hung, Nguyen Trung Thanh, and Nguyen Thanh Nam. Coexistence of positive and negative exchange bias in crmn/co bilayers. *Journal of magnetism and magnetic materials*, 298(1):43–47, 2006.
- [91] Xianglin Ke, Mark S Rzechowski, Land J Belenky, and Chang-Beom Eom. Positive exchange bias in ferromagnetic la 0.67 sr 0.33 mno 3/ srruo 3 bilayers. *Applied physics letters*, 84(26):5458–5460, 2004.
- [92] N. C. Koon. Calculations of exchange bias in thin films with ferromagnetic/antiferromagnetic interfaces. *Phys. Rev. Lett.*, 78:4865–4868, Jun 1997.
- [93] RL Stamps. Mechanisms for exchange bias. *Journal of Physics D: Applied Physics*, 33(23):R247, 2000.
- [94] Erik Folven, Andreas Scholl, Anthony Young, Scott T. Retterer, Jos E. Boschker, Thomas Tybell, Yayoi Takamura, and Jostein K. Grepstad. Crossover from spin-flop coupling to collinear spin alignment in antiferromagnetic/ferromagnetic nanostructures. *Nano Letters*, 12(5):2386–2390, 2012. PMID: 22468652.
- [95] T. J. Moran, J. Nogués, D. Lederman, and Ivan K. Schuller. Perpendicular coupling at fe–fef₂ interfaces. *Applied Physics Letters*, 72(5):617–619, 1998.
- [96] M. D. Stiles and R. D. McMichael. Model for exchange bias in polycrystalline ferromagnet-antiferromagnet bilayers. *Phys. Rev. B*, 59:3722–3733, Feb 1999.
- [97] Dieter Suess, Markus Kirschner, Thomas Schrefl, Josef Fidler, RL Stamps, and J-V Kim. Exchange bias of polycrystalline antiferromagnets with perfectly compensated interfaces. *Physical Review B*, 67(5):054419, 2003.

- [98] Yayoi Takamura, Erik Folven, Jonathan B. R. Shu, Karl R. Lukes, Binzhi Li, Andreas Scholl, Anthony T. Young, Scott T. Retterer, Thomas Tybell, and Jostein K. Grepstad. Spin-flop coupling and exchange bias in embedded complex oxide micromagnets. *Phys. Rev. Lett.*, 111:107201, Sep 2013.
- [99] E. Folven, A. Scholl, A. Young, S. T. Retterer, J. E. Boschker, T. Tybell, Y. Takamura, and J. K. Grepstad. Effects of nanostructuring and substrate symmetry on antiferromagnetic domain structure in lafeo₃ thin films. *Phys. Rev. B*, 84:220410, Dec 2011.
- [100] J Wu, D Carlton, JS Park, Y Meng, E Arenholz, A Doran, AT Young, A Scholl, C Hwang, HW Zhao, et al. Direct observation of imprinted antiferromagnetic vortex states in co/fe/ag (001) discs. *Nature Physics*, 7(4):303–306, 2011.
- [101] A. Hoffmann. Symmetry driven irreversibilities at ferromagnetic-antiferromagnetic interfaces. *Phys. Rev. Lett.*, 93:097203, Aug 2004.
- [102] B. Kaeswurm and K. O’Grady. The origin of athermal training in polycrystalline metallic exchange bias thin films. *Applied Physics Letters*, 99(22):222508, 2011.
- [103] M. K. Chan, J. S. Parker, P. A. Crowell, and C. Leighton. Identification and separation of two distinct contributions to the training effect in polycrystalline co/femn bilayers. *Phys. Rev. B*, 77:014420, Jan 2008.
- [104] Himanshu Fulara, Sujeet Chaudhary, and Subhash C. Kashyap. Biaxial anisotropy driven asymmetric kinked magnetization reversal in exchange-biased irmn/nife bilayers. *Applied Physics Letters*, 103(5), 2013.
- [105] Ben Van de Wiele, Jonathan Leliaert, Kevin J. A. Franke, and Sebastiaan van Dijken. Electric-field-driven dynamics of magnetic domain walls in magnetic nanowires patterned on ferroelectric domains. *New Journal of Physics*, 18, MAR 16 2016.
- [106] S.O. Parreiras and M.D. Martins. Effect of planar anisotropy in vortex configuration of micro-scale disks. *Physics Procedia*, 75:1142 – 1149, 2015.

- [107] Dustin A. Gilbert, Li Ye, Aida Varea, Sebastia Agramunt-Puig, Nuria del Valle, Carles Navau, Jose Francisco Lopez-Barbera, Kristen S. Buchanan, Axel Hoffmann, Alvar Sanchez, Jordi Sort, Kai Liu, and Josep Nogues. A new reversal mode in exchange coupled antiferromagnetic/ferromagnetic disks: distorted viscous vortex. *Nanoscale*, 7:9878–9885, 2015.
- [108] J. Železný, H. Gao, K. Výborný, J. Zemen, J. Mašek, Aurélien Manchon, J. Wunderlich, Jairo Sinova, and T. Jungwirth. Relativistic néel-order fields induced by electrical current in antiferromagnets. *Phys. Rev. Lett.*, 113:157201, Oct 2014.
- [109] P. Wadley, B. Howells, J. Železný, C. Andrews, V. Hills, R. P. Campion, V. Novák, K. Olejník, F. Maccherozzi, S. S. Dhesi, S. Y. Martin, T. Wagner, J. Wunderlich, F. Freimuth, Y. Mokrousov, J. Kuneš, J. S. Chauhan, M. J. Grzybowski, A. W. Rushforth, K. W. Edmonds, B. L. Gallagher, and T. Jungwirth. Electrical switching of an antiferromagnet. *Science*, 351(6273):587–590, 2016.
- [110] MJ Grzybowski, P Wadley, KW Edmonds, R Beardsley, V Hills, RP Campion, BL Gallagher, Jasbinder S Chauhan, V Novak, T Jungwirth, et al. Imaging current-induced switching of antiferromagnetic domains in cumnas. *Physical Review Letters*, 118(5):057701, 2017.
- [111] Shunsuke Fukami, Chaoliang Zhang, Samik DuttaGupta, Aleksandr Kurenkov, and Hideo Ohno. Magnetization switching by spin-orbit torque in an antiferromagnet-ferromagnet bilayer system. *Nature materials*, 2016.
- [112] M. Helsen, A. Gangwar, J. De Clercq, A. Vansteenkiste, M. Weigand, C. H. Back, and B. Van Waeyenberge. Non-linear radial spinwave modes in thin magnetic disks. *Applied Physics Letters*, 106(3):032405, 2015.

*Pulchra tota, sine nota
cujuscumque maculae
fac nos mundos et jucundos
te laudare sedit.*